Rapid pulsation growth at quasi-parallel collisionless shocks

Shruti Gopal

A Thesis submitted for the degree of Master of Philosophy

Astronomy Unit
School of Physics and Astronomy
Queen Mary, University of London.

August 2014

Declaration

The work presented in this thesis is the result of original research carried out by myself under the supervision of Prof. David Burgess, and has not been submitted for any other degree or award in any other university or educational establishment.

Signed: Shruti Gopal

Date: August 2014

For my beloved Sai Baba, my friend and Master.

Acknowledgements

I would like to thank my supervisor Prof. David Burgess, to whom I am immensely grateful for his academic guidance, invaluable support and suggestions over the course of my research and writing of this thesis. I also sincerely appreciate his prompt and critical review of my writing and his continual willingness to answer any questions or doubts that I have had throughout the PhD process.

This work would not have been possible without the STFC studentship. I also wish to thank my colleagues at School of Physics and Astronomy for providing a pleasant working environment, and providing welcome distractions and for helping make life in Queen Mary enjoyable and sociable.

I must express my gratitude to my friends and family for their enduring love, support and patience, and for continually believing in me and teaching me to never give up. Without them this thesis would not have been able to be completed.

Abstract

The bow shock is a shock wave that forms ahead of the Earth's magnetosphere in the collisionless supersonic flow of the solar wind. The quasi-parallel shock forms when the interplanetary magnetic field makes an angle of less than 45 degrees with the shock normal. Observations show the presence of magnetic pulsations, energetic diffuse ions and cooler, denser specularly reflected ions at the shock. Shock reformation involving the growth of magnetic pulsations is a key component of the structure of Earths quasi-parallel bow shock. This thesis aims to explore the rapid growth mechanism of these pulsations and hence increase our understanding of the structure of the quasi-parallel shock, which is generally less well understood than quasi-perpendicular shock. Using a hybrid simulation model of the interaction between shock reflected ions and upstream waves we study the effect of varying the parameters which control the growth of waves into large amplitude pulsations. A number of features are observed providing an insight into the growth mechanisms. Reflected ion beams can cause strong coupling with the pulse due to nonlinear cyclotron effects, and cause a narrow feature to develop. On the other hand, the diffuse ions show a relatively weaker interaction with the pulse and no narrow feature is generated. A strong interaction with the diffuse ions requires an unrealistically high density. However, in both cases, it is clear that the ULF wave does not simply just grow, as the pulse does not remain with the ions that cause the interaction. Instead the pulse splits and launches a new beamward (i.e., in the beam direction) wave in the simulation frame. This

result may explain the spacecraft observation that pulsations appear to slow down in the spacecraft frame. The newly launched propagating wave seems to have some of the same properties as solitons. Comparisons are made with observations from the Cluster spacecraft. Hence, the results give us a greater insight into the wave-particle dynamics in the reformation process and implications for particle acceleration at the quasi-parallel shock.

Contents

List of Figures

List of Tables

Chapter 1

Introduction

1.1 Collisionless shocks and context of study

We start with a description of collisionless shocks (Basic Space Plasma Physics by Baumjohann and Treumann, 1996; Astrophysical Plasmas book by Schwartz, Owen and Burgess, revised 2004). A shock is formed when a disturbance travels through a plasma at a speed that is faster than a characteristic wave speed of the plasma. For most solar system shocks this is the fast mode wave speed, and the resulting shock is called a fast mode shock. At the shock, there is a sharp change in density, pressure and speed of the plasma. In collisional shocks, collisions provide the coupling and allow transfer of energy and momentum between the particles. However, in a collisionless shock, such as Earth's bow shock, the characteristic shock length is much smaller than the collisional mean free path of the plasma particles. The mean free path between collisions in the solar wind is about 1 AU and the size of the system, that is, the thickness of Earths bow shock is 100-1000km. In a collisionless plasma, the fields and particles both act together to carry out the role of the collisions. In an ordinary

gas, it is collisions which cause the sound waves and transfer energy. However, at collisionless shocks, it is the collective behaviour of the particles and the magnetic fields that provide the dissipation required to heat the plasma at the shock.

There are a number of questions regarding collisionless shocks that still remain unanswered. These include the dissipation process, which is extremely difficult to define at this type of shock. In collisional shocks, the collisions evolve fast enough that the particle distribution is Maxwellian, with only a small percentage of particles at high velocities. However, particle distribution functions in collisionless plasma are often non-Maxwellian since some of the particles are accelerated to very high velocities. Therefore at collisionless shocks, the definition of temperature can be modified to describe the spread of the particle velocity distribution.

There are a number of ways to describe the dissipation process at collisionless shocks (Burgess within book by Russell and Kivelson, 1995). One way to describe the process is by instabilities. If there is some distortion in the particle distribution, this can lead to an instability. These instabilities then generate waves, which result in changes to the particle velocities. However, there is a problem with this model of the dissipation process. An instability most affects the particles that have caused that instability. For example, one possibility is that in the shock magnetic field gradient the current driven ion acoustic instability would be expected to heat the electrons more than the ions. But observations at solar system shocks show that ions are heated up more. This means other dissipation models may be needed to describe the dissipation process at collisionless shocks.

Another way to look at the dissipation process is to see how the particles are affected by the macroscopic fields in the plasma. This works because the plasma is collisionless and so the particle trajectories are effectively scatter-free. The fields themselves may be affected by the particles and hence this method can only apply if the particles are

not disturbed too much by the fields. If the fields change the spread of the particle velocity distribution, then the temperature of the plasma will be changed. Instabilities will then provide additional scattering and heating as a secondary process, driven by non-Maxwellian features of the velocity space distribution created by the macroscopic fields.

An important feature of collisionless shocks is whether they are time-steady or not. This is strongly influenced by the upstream magnetic field direction. So-called quasi-perpendicular shocks (see later for definition) have a largely time steady field profile, whereas quasi-parallel shocks are dominated by turbulent fluctuations. But in both cases distortion of the particle distributions by large scale field structures is important.

Collisonless shocks appear in different forms in the universe such as shocks produced by Coronal Mass Ejections, new stars, jets from Active Galactic Nuclei and supernova remnants. In this study, we look at Earth's collisionless bow shock. We particularly focus on the interactions between particles and waves which lead to fast wave growth, which seem to be important ingredients for the unsteady and turbulent character of Earth's quasi-parallel bow shock. A better understanding of these interactions should provide us with a clearer understanding of the processes involved at the bow shock and give us a better insight into the plasma processes near more distant shocks.

1.2 Earth's Magnetosphere

Here we describe the Earth's magnetosphere (Basic Space Plasma Physics by Baumjohann and Treumann, 1996). The magnetosphere forms as a result of the solar wind being frozen-in to the Interplanetary Magnetic Field (IMF) due to the high conductivity of the solar wind plasma. This means that solar wind plasma linked by a set of IMF lines, will remain linked to that set of field lines whatever the individual motion

of the two parcels of plasma. This frozen-in principle implies no mixing of fields and plasmas of different origin, in particular magnetic field from the sun remains separate from the field and plasma associated with Earth's magnetic field. Thus a magnetosphere, which is like a bubble, is formed around the Earth, and the solar wind flows around this region. There is a current generated at the boundary between the two different type of plasma and fields, which at the Earth is called the magnetopause.

In this magnetosphere, the Earth's magnetic field dominates and the solar wind is deflected around this field. A schematic of the magnetosphere can be seen in figure 1.1. The dayside is compressed to 6-10 R_E and the nightside is extended to 100-200 R_E. The bow shock is a shock wave that is formed since the solar wind, with typical speed of 450 km/s, is both supersonic and super-Alfvenic. This shock is very thin and has a curved shape, approximately symmetric about the sun-planet line. The exact position of the bow shock relative to the Earth depends on the solar wind ram pressure and strength of terrestrial field.

The region downstream of the bow shock is known as the magnetosheath and confines the shocked solar wind plasma. At the bow shock, the solar wind kinetic energy gets converted to thermal and magnetic energy, so the solar wind is slowed down to sub-sonic speeds and the plasma is denser and hotter than the solar wind plasma. The magnetopause is a boundary layer that separates the magnetosphere and the magnetosheath, and it is here that a current sheet exists. Its exact location can be found by balancing the solar wind ram pressure with the Earth's magnetic pressure just inside the magnetopause. Typically, it is located at 10 R_E, but variations in the solar wind ram pressure can mean that the position moves by several R_E. Since the magnetopause changes with solar wind conditions, the bow shock position is continually changing. This is observed when it moves over a spacecraft. The curved bow shock surface means that the magnetic field angle changes over the surface and the shock differs accordingly.

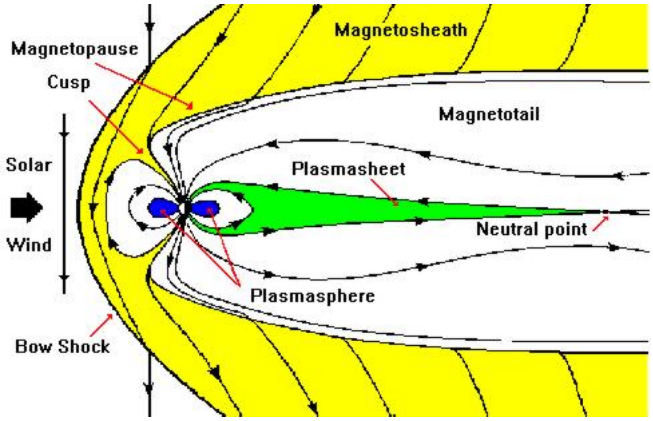

Figure 1.1: Schematic of Earth's magnetosphere showing the different regions [figure from website http://helios.gsfc.nasa.gov/magneto.html]

1.3 Earth's Bow Shock

The bow shock was first discovered by Ness et al., 1964 and it lies at a distance of 3-4 R_E in front of the magnetopause boundary. Greenstadt et al., 1970a, 1977, established a number of features of the bow shock: (1) it has a thick (2-2.5 R_E) pulsation region, (2) plasma distributions were characteristic of neither the magnetosheath nor the solar wind, (3) typical period of fluctuations was 10 seconds. Spacecraft observations (Kaufmann, 1967) showed that the shock is comprised of two types: sometimes it is an abrupt and sharp transition and at other times it is more turbulent with large amplitude pulsations (Fairfield, 1969; Greenstadt et al., 1970a, b).

The reason for the two types of shock is due to the Interplanetary Magnetic Field (IMF) being at an angle to the Sun-Earth line, so that it intersects the curved surface of the bow shock at different angles. This means that the bow shock has different properties at different points along its surface, depending on what angle the IMF makes with the shock normal (Greenstadt et al., 1970c). When the angle is less than 45 degrees, the shock is described as being quasi parallel, and when it is greater than 45 degrees, it is known as quasi perpendicular. The quasi-perpendicular shock is a

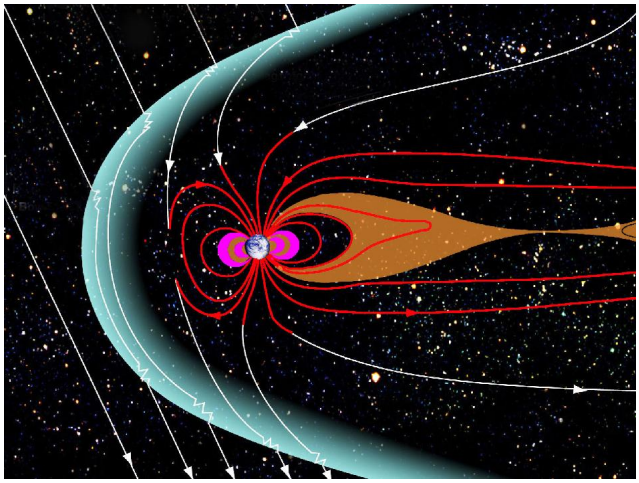

Figure 1.2: Schematic of Earth's magnetosphere showing the angles that the IMF (shown with white lines) makes with the bow shock [figure from website http://www.nasa.gov/topics/solarsystem/sunearthsystem/magnetosphere2-unlabeled.html]

sharp transition from upstream to downstream, relatively time steady and characterized by a steep rise in magnetic field strength known as the 'ramp', while the quasi parallel shock shows much more turbulence and is less stable.

About 25 per cent of the solar wind incident ions are specularly reflected at the quasi-perpendicular shock, depending on the upstream conditions (Paschmann and Sckopke, 1983; Wilkinson and Schwartz, 1990). Specular reflection means that the velocity component that is normal to the shock is reversed. The ions gyrate and pass downstream as a result of the orientation of the IMF lines. In the downstream region, these reflected gyrating ions dominate the heating required at the shock. Specularly reflected ions have also been observed at the quasi-parallel shock (Gosling et al., 1982, 1989; Onsager et al., 1990; Thomsen etal., 1990a; Fuselier et al., 1990). In this case though, the orientation of the IMF lines is such that the ions pass upstream (Gosling et al., 1982; Schwartz et al., 1983).

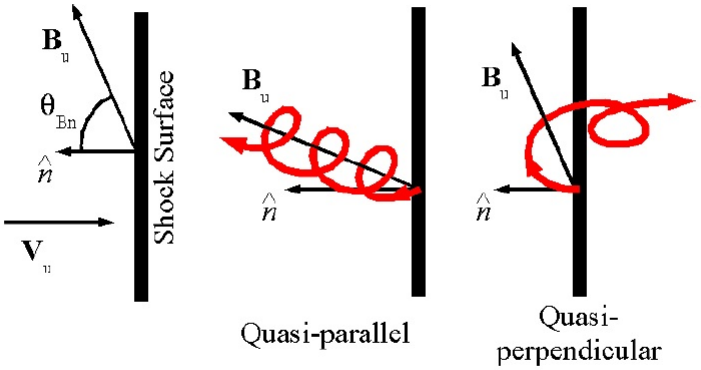

Figure 1.3: Schematic of particle trajectories at quasi-perpendicular shock and quasi-parallel shock, where reflected ion motion is shown in red [Astrophysical Plasmas on-line book by Schwartz. S. J, Owen. C, Burgess. D, revised 2004]

The small scale structure of both the quasi-parallel and quasi-perpendicular bow shock can be qualitatively understood by considering the trajectories of individual particles in the different magnetic field geometries. The characteristics of the two types of shock are determined largely by the trajectories of the ions specularly reflected at the shock, shown in figure 1.3. An ion reflected at the quasi-perpendicular shock has gyro-motion, which takes it back upstream. Within half a gyro-radius, the ion reverses its motion and returns back to the shock. As the field lines are almost tangential to the shock surface and are convecting towards the shock at the solar wind velocity, the reflected ion re-encounters the shock before carrying out more than a gyro-orbit. At the quasi-parallel shock, the ion reflected at the shock travels upstream with a large field-aligned velocity component. This picture assumes that the ion is unaffected by the motion of the solar wind and IMF and will escape upstream. An extended region forms when backstreaming ions return upstream, known as the foreshock and this will be discussed in detail in the next section.

1.4 SLAMS pulsations at the quasi-parallel shock

Observations of the quasi-parallel shock included studies by Greenstadt, 1974 and Greenstadt et al., 1977, in which data from Pioneer 9, HEOS 1 and OGO 5 was used to show that the shock is made of pulsations that are 1-2 R_E in size. Greenstadt et al., 1977, discussed that the plasma distributions that were associated with these pulsations were neither characteristic of the solar wind nor the magnetosheath. Thomsen et al.,1990, used ISEE-1 and ISEE-2 observations to find out whether these pulsations are amplified upstream waves convecting past the spacecraft or rapid contractions and expansions of the shock surface over the spacecraft. They found that the pulsations exist as both convected and nested signatures. Convected signatures are those where the magnetic signatures convect past the spacecraft with the solar wind, while the nested signatures describe the in and out motion of the bow shock. The quasi-perpendicular shock is invariably observed as a result of its in-out motion. Hence, transmissions which are convective were unexpected.

Later, Schwartz and Burgess, 1991, proposed a model of patchwork of the 3-D magnetic structures. They analysed magnetic field data during a shock crossing and introduced the idea of a broad shock transition region made up of 3-D pulsations named Short Large Amplitude Magnetic Structures (SLAMS). Figure 1.4 shows this model, where SLAMS are represented by shaded ovals. The magnetic field is shown by dashed lines and the bulk flow by the double arrows. As SLAMS are convected with the flow, they steepen and grow in amplitude (get darker in the diagram), slow down and merge with the other magnetic structures. They suggested that SLAMS have convected signatures rather than nested signatures.

The properties of SLAMS are documented by AMPTE-IRM and AMPTE-UKS observations (Schwartz et al., 1992) as: (1) being of short duration lasting only 5-20 seconds, (2) having large amplitude $(dB/B) \geq 2$, and (3) being well defined signa-

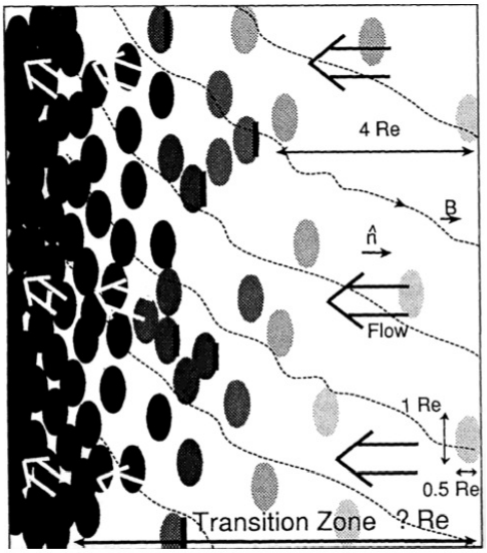

Figure 1.4: Schematic of the SLAMS, shown by shaded ellipses, magnetic field, shown by dashed lines, and bulk flow, shown by double arrows. [figure 1 in Schwartz and Burgess, 1991]

tures in magnetic field. It is generally accepted that the interaction between solar wind and backstreaming ions generate Ultra Low Frequency (ULF) waves, which then steepen into the SLAMS (Schwartz and Burgess, 1991). The properties of SLAMS are consistent with growing out of a ULF wave field (Thomsen et al., 1990). The ULF waves grow to 2-4 times their initial amplitude, into SLAMS, in as little as 5-20 seconds (Schwartz et al., 1992). The SLAMS then make up the quasi-parallel shock.

Schwartz, 1991 highlighted two types of SLAMS, the 'isolated' ones and 'embedded' ones. The 'embedded' SLAMS are often observed as being embedded within Long pulsations, which are periods of turbulent magnetic field lasting for about 2 minutes. The magnetic field signatures before and after an isolated event are typical of a ULF wave field and the ion distributions show a peak at the energies, temperature and direction of the solar wind. The rest frame speed of isolated SLAMS can be calculated from the difference in the timing of the SLAMS at two spacecraft. This was carried out in the study by Schwartz et al., 1992 and it was found that for larger amplitude structures there is faster propagation but no clear distinction between ULF waves and SLAMS. The speed of embedded SLAMS is more difficult to calculate, but it was observed that the larger structures showed longer delays.

More recent observations have been carried out using the multi-spacecraft of the Cluster mission. Lucek et al., 2008 used Cluster observations to show that any differences in SLAMS observations at different spacecraft are due to both spatial and temporal variations. At small spacecraft separations, the spatial variation is more dominant. Minimum spacecraft separation at which spatial variations are significant is 100-150 km (Lucek et al., 2004; Lucek, 2006). At spacecraft separations larger than 100-150 km, the spatial and temporal effects become important. These Cluster observations indicate that the Schwartz and Burgess model is over-simple. The SLAMS cannot just be uniform "blobs". There is spatial variation on small scales.

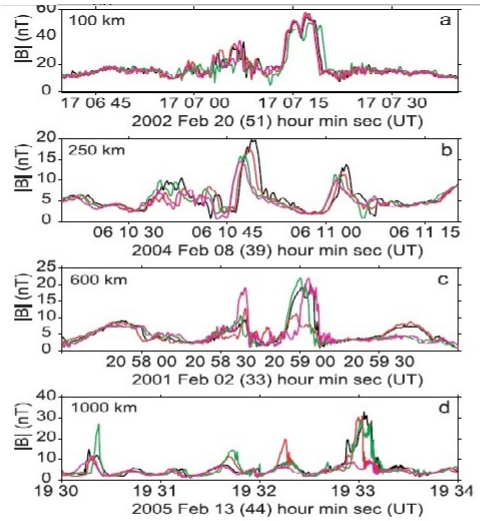

Figure 1.5: SLAMS signatures for different spacecraft Cluster separation distances: 100, 250, 600, 1000 km from top to bottom respectively. Cluster 1 is shown in black, Cluster 2 in red, Cluster 3 in green and Cluster 4 in magenta. [figure 1 in Lucek et al., 2008]

Typical 'isolated' SLAMS signatures are shown in figure 1.5. The plots show the magnetic field signatures from all four Cluster spacecraft with different separation distances of the spacecraft. Where the separation distance is small, any difference between the signatures from the four spacecraft are probably due to spatial differences. Where the separation distance is large, it is difficult to distinguish whether the differences are due to spatial or temporal differences. These Cluster observations suggest that the overall size of SLAMS is few thousand km.

Lucek et al., 2008 used observations from Cluster spacecraft to calculate the SLAMS growth rate. They plotted the fractional magnetic field magnitude difference of SLAMS against the time delay between pairs of spacecraft. The plot had a positive gradient, showing that temporal evolution was dominant. The growth rate of

SLAMS, obtained from the gradient of the line of best fit, was 0.07 +/- 0.01 s^{-1} for data from spacecraft with 250 km separation and 0.043 +/-0.004 s^{-1} for data from spacecraft with 1000 km separation. These results are consistent with simulations which show that growth occurs on a timescale of inverse gyrofrequency (Scholer et al., 2003; Tsubouchi and Lembege, 2004).

There have been a number of calculations of the size of the transition zone in which the SLAMS growth occurs. This is the region from first appearance of SLAMS to the merged state that forms at the magnetosheath. It was found to have an upper limit of 2700 km from Cluster observations (Lucek et al., 2008). This was calculated from measurements of magnetic field, plasma number density and plasma velocity at each of the four spacecraft. The result shows that it is a narrow transition layer and only one or at the most a few SLAMS will fit into this layer at a time. This is an area where more observations, especially multi-spacecraft, will be important.

Hybrid simulations on the quasi parallel shock have revealed that it is cyclically reforming (Burgess, 1989) with periods where the transition is more abrupt and sharp and periods where it is more gradual and extended. This can be seen in figure 1.6. Since the time that reformation of the quasi parallel shock was discovered, there have been a range of mechanisms put forward to explain the reformation process (Winske et al., 1990; Lyu and Kan 1990; Pantellini et al., 1992; Onsager et al., 1990; Scholer and Burgess, 1992; Scholer 1993; Giacalone et al., 1993; Dubouloz and Scholer, 1993, 1995). The reformation process may occur as a result of any of the mechanisms described in these works or it may be a combination of mechanisms.

The mechanisms put forward include the interface instability mechanism of Winske et al., 1990, the whistler wave scattering mechanism of Lyu and Kan, 1990, and Pantellini et al., 1992, the reflected ion deflection mechanism (Onsager et al., 1991a,b; Scholer and Burgess, 1992) and the diffuse ion mechanism (Scholer, 1993; Dubouloz

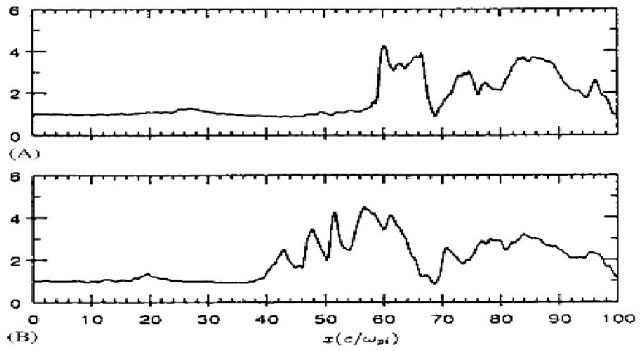

Figure 1.6: Plots of magnetic field magnitude, normalised to its upstream value, along the simulation box for simulation of high Mach number shock, where the top panel (A) shows an abrupt and sharp transition and the bottom panel (B) shows a more gradual transition of the quasi parallel shock. [figure 2 in Burgess, 1989]

and Scholer, 1993, 1995). However Scholer, 1993, suggested that the former two mechanisms may not play a role in reformation since the wave steepening process occurs more than 20 ion inertial lengths upstream of the shock ramp. The latter two mechanisms that seem to be established as causing the growth of SLAMS and thus leading to shock reformation are described in detail in Chapter 2. There is not yet agreement on the pulsation growth mechanism and whether or not different mechanisms operate simultaneously.

In this study, we focus on the region in the shock transition where both specularly reflected ions and diffuse ions are present. We present results of hybrid simulations of the interaction of ions with a convecting pulse (Chapter 4) along with Cluster observations (Chapter 5) to identify signatures of the two mechanisms: the reflected ion deflection mechanism and the diffuse ion mechanism.

1.5 Foreshock

At the Earth's bow shock, particles which gain sufficient energy at the shock can escape upstream without being swept back into the shock, thus forming a foreshock region. However, waves in the foreshock can scatter ions back to the shock, leading to acceleration to higher energies. The foreshock is made up of inflowing solar wind particles that are reflected from the shock, as well as any magnetosheath particles that have leaked back across the shock. Different parts of the shock are effective for accelerating different particle populations, for example, electrons are accelerated at the quasi-perpendicular shock. Since electrons travel faster than ions the foreshock is made up of two regions. These are the electron foreshock, which has a boundary where the IMF becomes tangential to the bow shock and the ion foreshock, which is further downstream.

There are a number of particle distributions observed in the ion foreshock. There are specularly reflected ions with energies 1-5 keV, that are observed locally close to the quasi parallel shock. Three other ion distributions have been observed: field aligned beams (Asbridge et al., 1968), diffuse ions (Gosling et al., 1978) and intermediate ions (Paschmann et al., 1979).

High energy (tens of keV) field aligned beams are found at the upstream edge of the ion foreshock (Lin et al., 1974). These beams are produced by shock drift acceleration of solar wind ions (Armstrong et al., 1985). Lower energy (1 keV) field aligned beams are observed deeper in the foreshock (Sonnerup, 1969), produced by shock drift acceleration of solar wind ions and from leakage of ions from the magnetosheath (Schwartz and Burgess, 1984; Fuselier and Thomsen, 1992).

Diffuse ions have energies up to 200 keV (Scholer et al., 1979; Thomsen, 1985) and are found deep in the foreshock close to the quasi-parallel shock. These ions have

broad, nearly isotropic angular distributions (Gosling et al., 1978). It was originally thought that diffuse ions originated from field aligned beams (Gosling et al., 1978; Bame et al., 1980; Thomsen, 1985). However it was later observed that the alpha particle to proton ratio in the field aligned beams was much smaller than in the diffuse ion distribution (Ipavich et al., 1988; Fuselier and Thomsen, 1992). Therefore it is unlikely that diffuse ions evolved from the field aligned beams. Simulation studies suggest that diffuse ions have evolved from solar wind ions that are trapped at the shock and gain energy in the solar wind motional electric field (Scholer et al., 1998).

There are also gyrophase-bunched ions, which result from lower energy field aligned beams being trapped in low frequency monochromatic waves (Hoshino and Terasawa, 1985; Thomsen et al., 1985; Fuselier et al., 1986a, b). When these waves grow, they scatter the gyrophase-bunched ions to form intermediate ions, which have a larger pitch angle spread and higher energies than field aligned beams.

Figure 1.7 shows schematic view of bow shock and some of its particle distributions. We can observe field aligned beams on field lines for $\theta_{Bn} = 40 - 70$ degrees. Diffuse ions can be seen deeper in the quasi-parallel shock. In the schematic the 2D velocity space relief plots show these ions. The sharp peak in the plots is the solar wind. There is coupling of different parts of the bow shock as a result of the foreshock, since the particles can travel along the IMF lines.

The foreshock is also characterized by extensive wave activity, which results from the interaction of the backstreaming ions with the inflowing solar wind. The non-Maxwellian distributions of the backstreaming ions give rise to instabilities, which in turn excite ultra-low-frequency (ULF) magnetohydrodynamic waves, ion acoustic waves, and electron plasma oscillations. ULF waves are the most prominent type of waves at the ion foreshock. They are emitted by ion-beam instabilities triggered by the back-scattered particles and inflowing solar wind ions (Le and Russell, 1992).

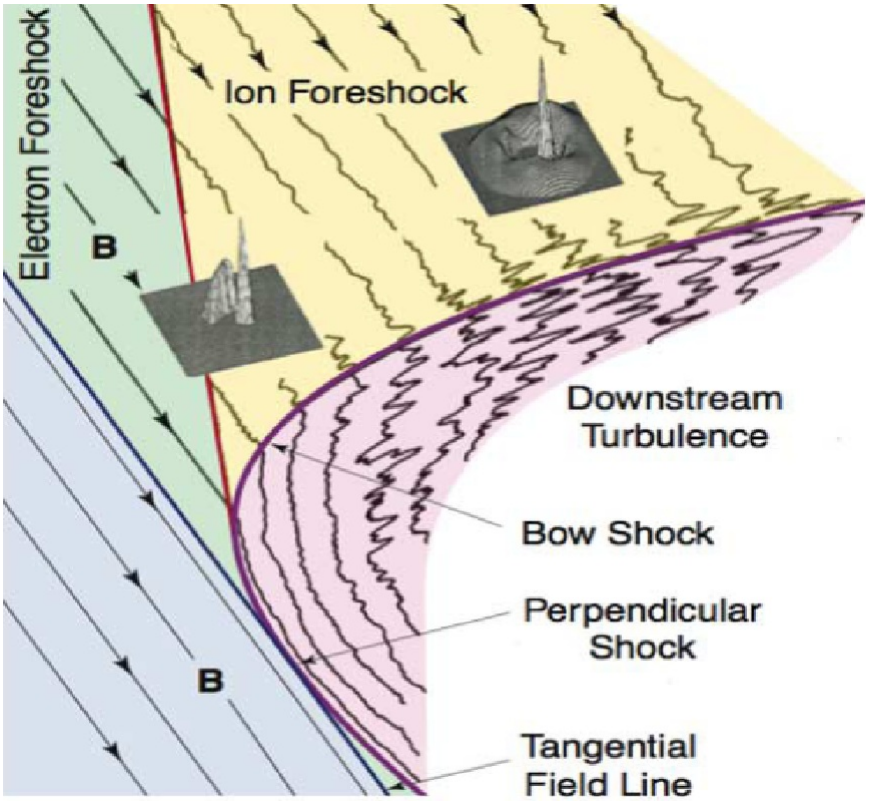

Figure 1.7: Schematic view of the bow shock where the foreshock is shown upstream of the quasi parallel shock and downstream of the tangential field line. The foreshock is split into the electron and ion foreshocks. The field aligned and diffuse ions are shown using 2D velocity space relief plots where the field aligned beams are just behind the ion foreshock boundary and diffuse ions are observed deeper in the quasi-parallel shock. The sharp peak in these plots represents the solar wind. [figure 7 in Treumann and Scholer, 2001, Desai and Burgess, 2008, and Eastwood et al., 2005]

These ULF waves, with amplitude of $1B_0$ and periods of about 30 seconds, propagate sunward, but are convected earthward by the solar wind (Hoppe and Russell, 1983). These waves can be seen in figure 1.8.

Close to the foreshock boundary, the ULF waves are nearly sinusoidal and exhibit left-handed polarisation in the spacecraft frame (Hoppe et al., 1981; Le and Russell, 1992). Deeper in the foreshock, their amplitude increases and they become less sinusoidal, strongly compressed, exhibiting both left-handed and right-handed polarisation in the spacecraft frame (Blanco-Cano and Schwartz, 1995). The left-handed compressional waves can be explained by the ion-ion resonant instability. The right-handed compressional waves are thought to be generated by either the non-resonant firehose instability or by the left-handed Alfven-ion resonant instability.

The electron foreshock exists further upstream from the ion foreshock due to the high velocity of accelerated electrons which means that they more closely follow the magnetic field lines despite the solar wind convection (see figure 1.7). The high energy (16 keV) electron beam forms along the tangent field lines, while 5 keV electrons are observed behind the electron foreshock boundary and 1 keV electrons are observed deeper in the foreshock. The energy flux of the high energy electrons falls off rapidly downstream of the tangent IMF field lines. The electrons in the foreshock form unstable distributions and generate Langmuir waves at frequencies near the electron plasma frequency (Filbert and Kellogg, 1979; Anderson et al., 1979; Bale et al., 1997; Cairns, 1987a, b).

1.6 Overview of thesis

In this thesis, we focus on the quasi parallel bow shock and in particular the region of the foreshock where both diffuse ions and specularly reflected ions are present. We

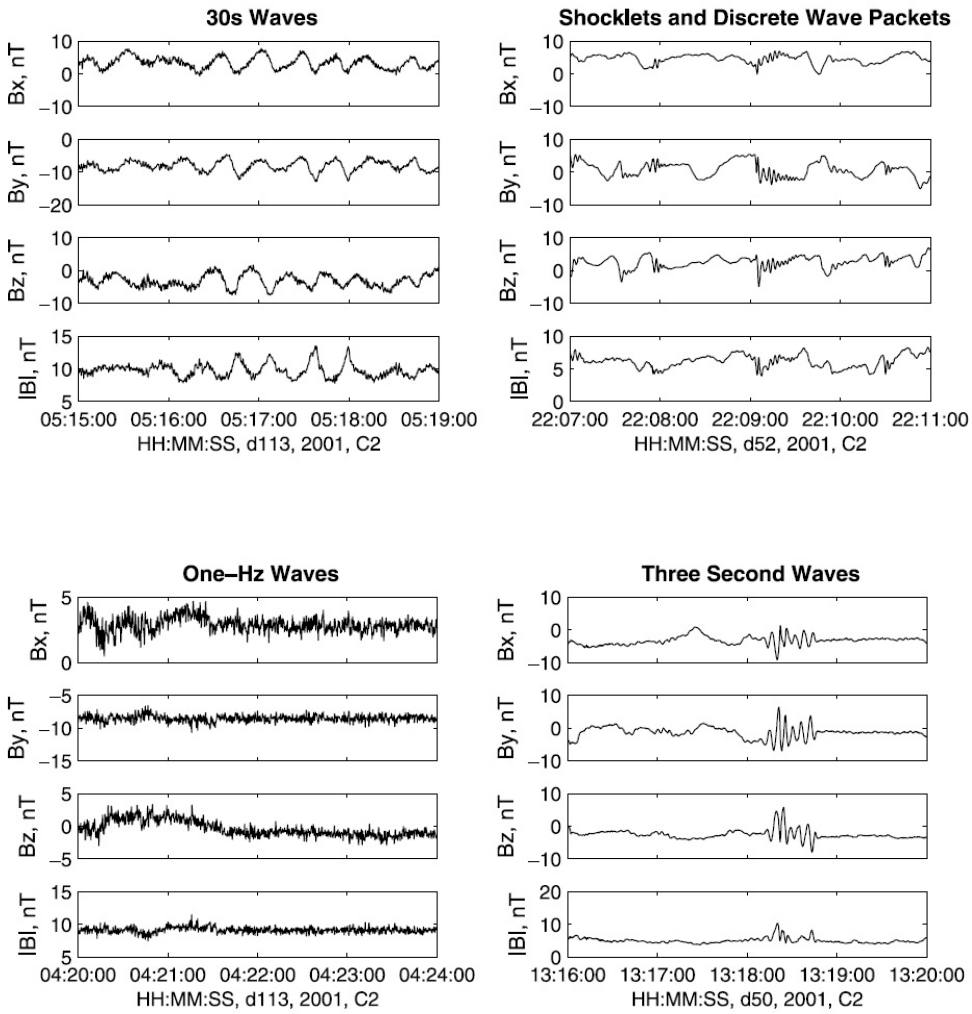

Figure 1.8: Different types of ULF waves observed at the foreshock by Cluster FGM [figure 1 from Eastwood et al., 2005]

investigate the reformation mechanism of the shock using hybrid simulations of the interaction of the ions with a convecting pulse. Unlike in shock simulation studies, our model allows us to vary different parameters such as density of the ions, angle the reflected ions make with the shock normal, velocity of the ions and the initial amplitude of the pulse. Hence, we are able to present some of the signatures of the reformation mechanisms. The signatures may allow an observational identification of which mechanism is dominant at pulsations seen at the bow shock.

In addition to the simulation work, we use Cluster spacecraft data to study the pulsation events to gain a better insight into the reformation mechanism. The Cluster instruments such as the Fluxgate Magnetometer (FGM) and the Cluster Ion Spectrometry (CIS) allow us to observe the magnetic field and ion distributions with high resolution (The Cluster Active Archive by Laakso, Taylor and Escoubet, 2010). By combining the magnetic field data with the ion distribution data, we can understand the signatures of the reformation mechanism at events where diffuse ions or reflected ions are involved. We are also able to compare the Cluster observations with the simulation results of the ion distributions.

Chapter 2 is a more detailed description of the reformation process at the quasi-parallel shock and discusses the different controversies that exist about which mechanism is involved. The controversies include a difference in opinion as to whether ULF waves are involved in the process, whether instabilities are involved and whether the reflected ions or the diffuse ions play a more dominant role. A description of the two mechanisms investigated in this study, namely the diffuse ion mechanism and the reflected ion deflection mechanism, is given in this chapter.

The next chapter, chapter 3, is a brief introduction to the simulation method. We also discuss the work where we used the Kuramitsu and Hada, 2008 model to look at the interaction between a static pulse and a specularly reflected ion. Kuramitsu and Hada,

2008 study the interaction between a static pulse and an ion where the interaction is in the coordinate frame moving with the wave packet. They then plot the reflection probability of the ion for different pulse amplitude b, and winding number n, which is the number of rotations the transverse magnetic field makes within the wave packet. Since this work is the starting point for our self-consistent simulations, we present an extension of this work in parameter range.

Chapter 4 looks at the interaction between a propagating pulse with specularly reflected ions and diffuse ions using a hybrid simulation, which accounts for the difference in time and length scales between electrons and ions by treating the ions as particles and electrons as a fluid. Our simulation has the same initial conditions for the pulse as the Kuramitsu and Hada, 2008 model, but the use of the hybrid simulation allows for the self-consistent evolution of particles and fields. This is important for observing the effect of the ions on the pulse because the ions can have a significant impact on the pulse. We first focus on interaction between the pulse and reflected ions, both the gyrating and field aligned beam cases and then we look at the interaction between the pulse and diffuse ions.

Chapter 5 discusses in-situ observations of a number of SLAMS events and shows comparisons with our simulation work. The data used is from Cluster spacecraft, particularly from the Fluxgate Magnetometer (FGM) and the Cluster Spectrometry (CIS) instruments. We determine the times when Cluster spacecraft are in the appropriate region of the magnetosphere and look at magnetic field data to identify a number of SLAMS events. For those events, we study the velocity space plots showing the velocity distribution of the different types of ions including the diffuse ions, the gyrating ions and field aligned ions. In this chapter we also compare the ion distribution plots with similar plots from simulation work.

The last chapter, chapter 6 is a discussion of all the results from the previous chapters

and an overall view. It includes a comparison of the simulation work with the in-situ observations work.

Chapter 2

Mechanisms of reformation at the quasi-parallel shock

2.1 Overview

The idea of cyclic reformation process at the quasi-parallel shock was first suggested by Burgess 1989 using hybrid simulations and since then there have been many authors that have confirmed this. The reformation process can explain a number of observations such as the variety of magnetic field signatures and cold ion beams in the shock transition. Through simulations of high Mach number shocks we see that the shock structure has periods of a sharp transition and periods of a more gradual transition and then the process repeats itself. It is the foreshock waves that propagate toward the shock along with the ions being reflected at the shock that seem to be linked to this reformation mechanism. The ions upstream of the shock, which have been reflected at the shock, are at high densities and so form a pressure pulse that relaunches the shock position.

Since the time that studies revealed that the quasi-parallel shock is cyclically reforming (Burgess, 1989), there have been a range of models put forward to explain the reformation process. It has been established that SLAMS make up the quasi parallel shock (Schwartz and Burgess, 1991). However, the exact mechanism for the growth of SLAMS and thus the reformation process is still controversial.

There is a controversy about the role of ultra-low frequency (ULF) waves in the process. While some authors feel that the presence of ULF waves may be crucial for reformation (Burgess, 1989; Scholer and Terasawa, 1990; Scholer and Burgess, 1992; Schwartz et al., 1992), others have found that reformation can occur even without ULF waves (Winske et al., 1990; Thomsen et al., 1990; Onsager et al, 1991a). There is also a difference in opinion about the reformation process with regards to whether it is triggered by instability (Onsager et al., 1991a; Scholer, 1993; Winske et al., 1990) or related to the reflected ion deflection model (Onsager et al., 1990b, Scholer and Burgess, 1992). There are some works that highlight the importance of specularly reflected ions in the reformation process (Burgess, 1989, Onsager et al., 1991a, Scholer and Burgess, 1992) and others which suggest that diffuse ions play a more distinctive role (Scholer, 1993, Dubouloz and Scholer, 1993, 1995). Then there is model by Lyu and Kan, 1990 and Pantellini et al., 1992, who suggest that the interactions between the incident ions and the whistler wave trains cause the reformation process.

These controversies will all be explored in this chapter and some of these works (Winske et al., 1990; Lyu and Kan 1990; Pantellini et al., 1992; Onsager et al., 1991a, 1991b; Scholer and Burgess, 1992; Scholer 1993; Giacalone et al., 1993; Dubouloz and Scholer, 1993, 1995) will be further discussed. It can be said that the reformation process may occur as a result of any of the mechanisms described in these works or it may be a combination of mechanisms. For example, at small angles of magnetic field to shock normal a certain model may apply, while at larger angles, a different model may apply.

2.2 Instability approach versus the reflected ion deflection model

There is a controversy regarding whether the reformation process is caused by an instability or by a physical effect that can be represented by the reflected ion deflection model. The reflected ion deflection model describes the process in which beam ions are decelerated and deflected by a wave crest in the magnetic wave field. This leads to a local enhancement in the ion density and since the flow is frozen in with the flux, an increase in the magnetic field. Hence it leads to a positive feedback loop, since the background ions are then decelerated and deflected by the enhancement in the magnetic field. The role of instabilities will be described first and then the reflected ion deflection model will be discussed in this section.

A plasma instability in a region occurs when a change in the plasma characteristics (magnetic field , temperature, density) causes turbulence because the particle distribution function becomes unstable. For a linear instability, waves in some mode will grow exponentially, until they saturate by some non-linear process. There are many types of plasma instabilities and some authors (Onsager et al., 1991a; Scholer, 1993; Winske et al., 1990) suggest that instabilities trigger the reformation process at the shock. Winske et al., 1990 say that the interface instability causes the process. This instability takes place because the coupling between the incoming ions and the downstream ions is very unstable. An upstream wavefield is not required for the interface instability. However, Scholer, 1993 suggests that the ion-ion beam instability is more important. This instability takes place when the incoming solar wind ions interact with the diffuse ions and causes the growth of the waves in the magnetic wavefield. Onsager et al., 1991a particularly highlight the importance of both the resonant and nonresonant modes of the ion-ion instabilities in the process. They discuss the ion-ion beam instability that results from the interaction between the incoming ions and the

specularly reflected ions.

Winske et al., 1990 carry out 1D hybrid simulations and show that the backstreaming upstream ions are needed for the reformation provided that they are within a distance of 10 c/ω_{pi} from the shock, where ω_{pi} is the ion plasma frequency. They also used numerical experiments, where they were more able to control the conditions than in a real shock simulation. It was shown that waves were excited before ions could propagate far enough upstream to excite the resonant modes. Therefore they suggested that the waves result from a resonant interaction at the interface, and so are independent of the upstream waves.

Scholer, 1993 used 1-D hybrid simulations to also show that an instability leads to shock reformation. However, he highlighted the role of the ion-ion beam instability in causing wave steepening and amplification as opposed to the interface instability described by Winske et al., 1990. The ion-ion beam instability results from the interaction of two counterstreaming beams, in this case the solar wind beam and the diffuse ions. The simulation used a pre-existing wavefield, and the magnetic field was at an angle of 30 degrees to the shock normal. The study looks at the effects on the wave field by the diffuse ions. Scholer, 1993 suggests that the upstream waves grew as a result of this instability. It was found that ULF waves grow into SLAMS and result in reformation providing that the gradient in the ion beam density is of the same order as the wavelength of the ULF wave.

Figure 2.1 shows the ion phase space, number of backstreaming ions, and tangential components of the magnetic field against the distance across the shock, in the shock normal direction, at $\Omega_{ci}t = 71$ where Ω_{ci} is the ion gyrofrequency. It is defined as $\Omega_{ci} = eB_0/mc$, where c is the speed of light, e is the magnitude of the electronic charge, m is the ion mass and B_0 is the upstream magnetic field strength. In this figure, the shock ramp can be seen as being located at about $x = 422$ and the steepened edge of

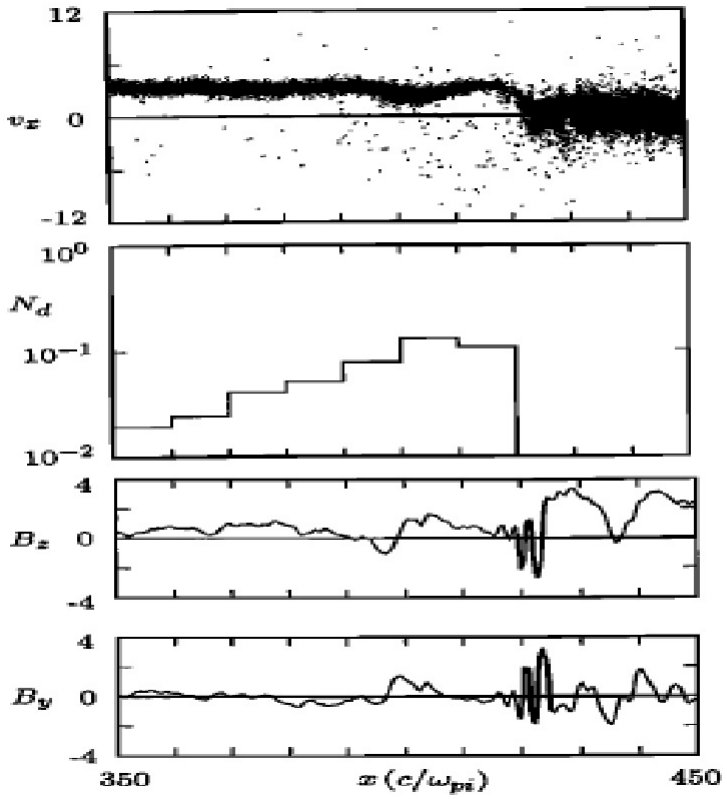

Figure 2.1: Ion phase space (top panel), number of backstreaming ions, and tangential components of the magnetic field against the distance across the shock, in the shock normal direction, at $\Omega_{ci}t = 71$. The shock ramp can be seen as being located at about $x = 422$ and the steepened edge of the wave is at about $x = 397$, [figure 2 in Scholer, 1993]

the wave is at about $x = 397$. It can be seen from this plot that the intensity of the diffuse ions increase almost exponentially toward the shock. This suggests that the growth of the steepened wave, often described as a shocklet, is due to the increase in diffuse ion density close to the shock. Dubouloz and Scholer, 1995 agree with these findings. According to Scholer, 1993, when there is a hot and tenuous beam, the wave growth is driven by the ion-ion beam instabilities. He argues that the reformations take place 20 c/ω_{pi} upstream from the shock and so dismisses the role of the interface instability of Winske et al, 1990 in the reformation process.

Observations from the AMPTE-UKS spacecraft by Giacalone et al., 1993 showing an increase of energetic particle pressure near the pulsation agree with the results of Scholer, 1993 and his model of the ion-ion beam instability to explain reformation. However, they found some differences in the energetic particle pressure around SLAMS. They found that at different energies the ion pressure increases just before the SLAMS signature and then decreases after SLAMS has convected past the spacecraft, indicating coupling between the SLAMS and energetic particles.

Onsager et al, 1991a carried out 1-D hybrid simulations and they also found that ion-ion beam instabilities play an important part in shock reformation. A cold, high density beam was used in the study and they looked at the interaction between the specularly reflected ions and the solar wind incident ions as opposed to diffuse ions. The magnetic field was parallel to the beam and to the solar wind direction and there was no initial wavefield used. The solar wind plasma flowed in the +x direction with speed 5 V_A and the reflected beam was directed in -x direction with a speed 5 V_A. The beam densities used ranged from 11 per cent to 82 per cent of the background ion density. The simulations were effectively done in the shock frame. Figure 2.2 shows the total density normalised to the initial density for the beam, the magnetic field normalised to the initial value, the phase of the transverse magnetic field and the total ion temperature normalised to the initial ion temperature as a function of distance at $\Omega_{ci}t = 20$. The density and magnetic field enhancements can be seen in the plot.

A finite beam was used for the reflected ions and the results of the interaction were compared with linear theory for an infinite beam. Generally, the resonant mode is unstable at low ion densities and the non-resonant mode is unstable at higher densities. For the high densities used in this study, the linear instability theory for an infinite beam predicts that the non-resonant mode is more unstable over a wide range of densities. This can be seen in figure 2.3, which shows the growth rate of the

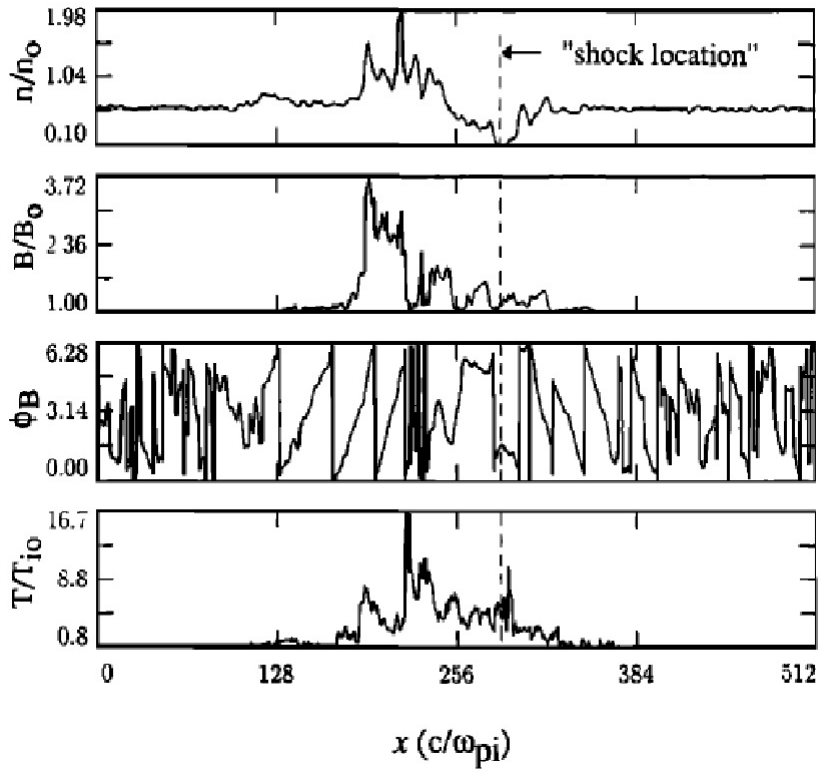

Figure 2.2: Total density normalised to the initial density for the beam, the magnetic field normalised to the initial value, the phase of the transverse magnetic field and the total ion temperature normalised to the initial ion temperature as a function of distance at $\Omega_{ci}t = 20$ [figure 5 in Onsager et al., 1991a]

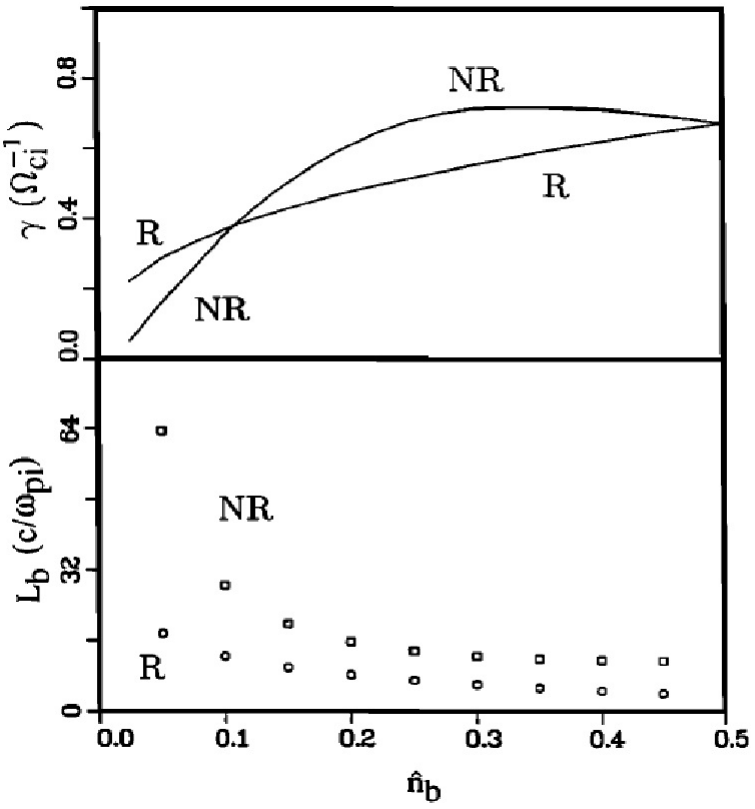

Figure 2.3: Growth rate of the resonant and non-resonant modes as a function of beam density, from linear theory(upper panel), length of beam required for resonant and nonresonant modes to be in contact with beam for one linear growth time (lower panel) [figure 7 in Onsager et al., 1991a]

resonant and non-resonant modes as a function of beam density, from linear theory. The wave helicities were used to work out the regions dominated by different modes, since both modes are RH polarized but propagate in opposite directions and so have opposite helicity. The finite beam study suggested that both the resonant and non-resonant modes are unstable in the interaction between the counterstreaming ions, contrary to the linear theory.

Two main reasons were suggested for this discrepancy. The first reason is that the resonant mode has a lower group velocity than the non-resonant mode and so this

wave is in contact with the beam for longer than the non-resonant mode wave. This has the effect of making the resonant mode wave grow to larger amplitudes even though it has a lower growth rate than the non-resonant wave. The second reason is a result of there being thermal spread in the velocities of the beam particles. This means that a cold low density region forms ahead of the beam. The resonant waves grow in this region and as they grow they become more pronounced than the non-resonant waves.

Scholer and Burgess, 1992 used 1-D hybrid simulations and show that the reflected ion deflection model can describe the reformation process. They looked at the interaction between ULF waves and specularly reflected ions and find that the waves grow in amplitude and steepen. They say this wave growth is caused by the deceleration and deflection of ions by the wave crest. In this model the upstream wave must have a large local value of angle between the magnetic field and direction of beam propagation. The deflection means that there is a local density increase and due to the compressibility of the plasma, there is also an increase in the magnetic field. A positive feedback loop is set up as described above. This process can be seen in figure 2.4, which shows the $x - V_x$ phase space plot (left) and the transverse magnetic field (right). When the beam ions encountered a large value of B_z and B_y in the wave crest, they were decelerated. The ions were deflected in the V_z and V_y direction and velocity V_x went to zero so that the beam ions were flowing tangential to the shock front. There was a local increase in both the density and the field components B_z and B_y. This caused a slowing of incoming background ions, which led to further increase in magnetic field. It can be seen from phase angle plots in figure 2.5 that the wave helicity is almost unchanged. This suggests that the ion-ion beam instabilities are not important in the enhancement of the magnetic field and thus shock reformation.

This model is consistent with Onsager et al., 1991b, who also used 1-D hybrid simulations to look at the interaction between the reflected ions and solar wind ions. Their

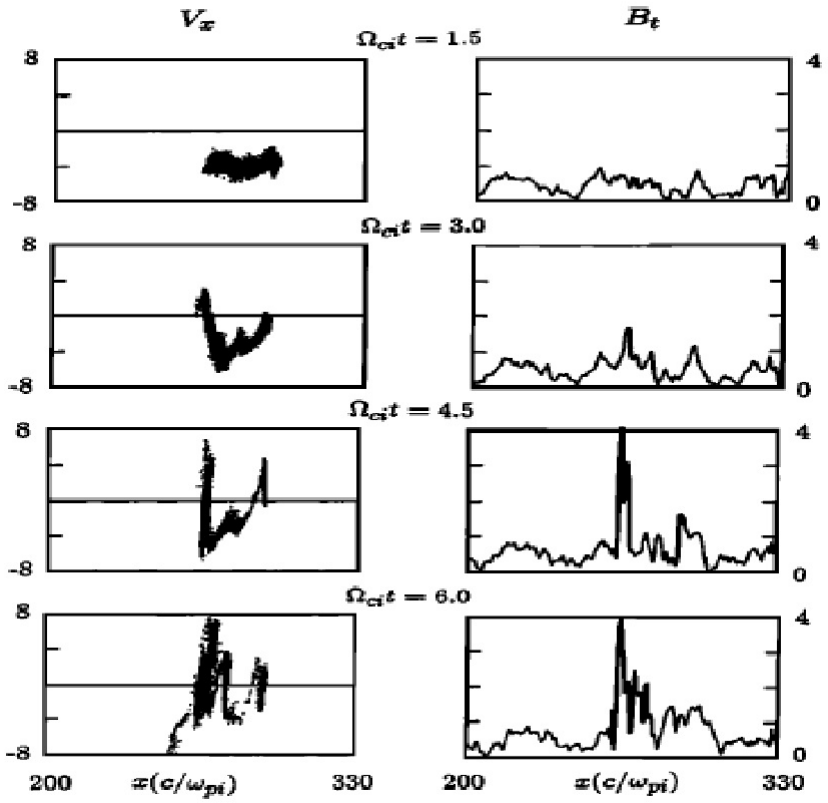

Figure 2.4: $x - V_x$ phase space plots (left) and the transverse magnetic field plots(right) for different times when beam density was 40 per cent of incident ions [figure 4 in Scholer and Burgess, 1992]

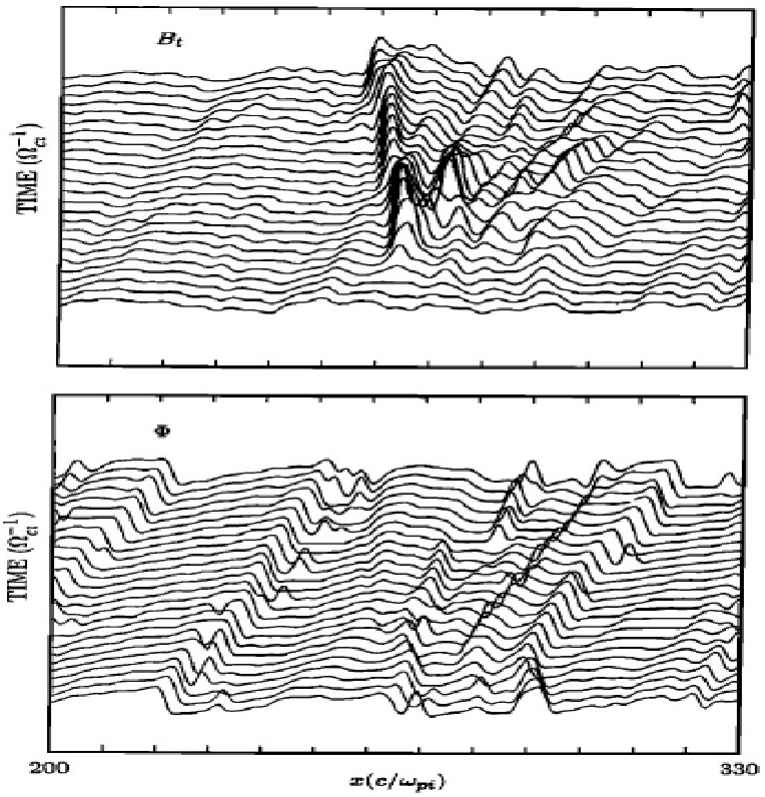

Figure 2.5: Stack plots of tangential magnetic field (top) and the magnetic field phase (bottom) for the simulation with density of 40 per cent of incident ions [figure 5 in Scholer and Burgess, 1992]

simulations are similar to those in Onsager et al., 1991a, except that in Onsager et al., 1991b, they have used a wave field and the magnetic field is at an angle to the shock normal direction. They suggest that the shock forms at a position upstream, where the ions have zero velocity in the direction normal to the shock. Onsager et al, 1991b found that coupling of reflected ions to background plasma ions varies with the angle of magnetic field to shock normal, θ_{BN}, the beam density and the beam temperature. They suggest that coupling occurs at time and location where the injected ions are deflected and become moving transverse to the shock normal direction. As time progresses in the simulation, beam ions and background ions are slowed down to $V_x = 0$ at some location. Also there is an increase in beam density and magnetic field indicating shock formation. The reformation distance and time was plotted as variation with θ_{BN}, beam density and beam temperature. The results were compared with results from test particle equations from Gosling and Thomsen, 1985. Simulations showed similar trends to expectations from the equations, that is, larger reformation lengths and times for smaller θ_{BN} values. However, lengths were shorter and times were longer than expectations. They give a possible explanation that the density of injected ions needs to accumulate for shocklike structures to grow.

So, there exist two main views to describe the reformation process: one view involves instabilities (Onsager et al., 1991a; Scholer, 1993; Winske et al., 1990) and takes a linear approach, while the other view is the deflection model (Onsager et al., 1990b and Scholer and Burgess, 1992) and takes a non-linear approach. It can be argued that while the linear approach describes the reformation process reliably, it is limited to only small amplitudes and so can only provide a picture of the process fairly locally. The non-linear approach may be more appropriate in the context of the reformation process where the wave amplitudes reach large values. This is discussed in more detail in the next section.

2.3 Ultra Low Frequency wave controversy

Some authors argue that SLAMS grow directly from ULF waves since their properties are consistent with growing out of a ULF wave field (Burgess, 1989; Scholer and Terasawa, 1990; Scholer and Burgess, 1992; Schwartz et al., 1992). ULF waves are produced by ion-beam instabilities triggered by the back-scattered particles and inflowing solar wind ions at the foreshock region (Le and Russell, 1992). These ULF waves, with amplitudes of $\Delta B/B_0 \sim 1$ and periods of 30 seconds, propagate sunward, but are convected earthward by the solar wind (Hoppe and Russell, 1983). They grow to 2-4 times their initial amplitude, into SLAMS, in as little as 5-20 seconds (Schwartz et al., 1992).

Scholer and Burgess, 1992 have shown, using 1-D hybrid simulations, that providing there is a cold ion beam, an upstream ULF wave can grow into SLAMS. Their work is described in some detail in the previous section. This study suggests that the ULF wave is a key ingredient of the reformation process.

A similar view is taken by Schwartz et al., 1992, who studied a number of SLAMS events using observations from AMPTE UKS and IRM satellites. They found that various characteristics such as the duration and polarisation of SLAMS are consistent with their growth from ULF wavefield. The SLAMS were found to be of short duration, in the range 5-20 seconds, which is similar to the ULF waves. The SLAMS are plane polarised, have a gradual linear rise and a steep trailing edge, similar to ULF waves. Figures 2.6 and 2.7 show the magnetic field magnitude time series plot and hodogram of the magnetic field of a SLAMS event and ULF wave. Apart from the difference in amplitude of the magnetic field, the magnetic signatures of the SLAMS and the ULF wave events are very similar, suggesting that the SLAMS grow directly out of the ULF wavefield.

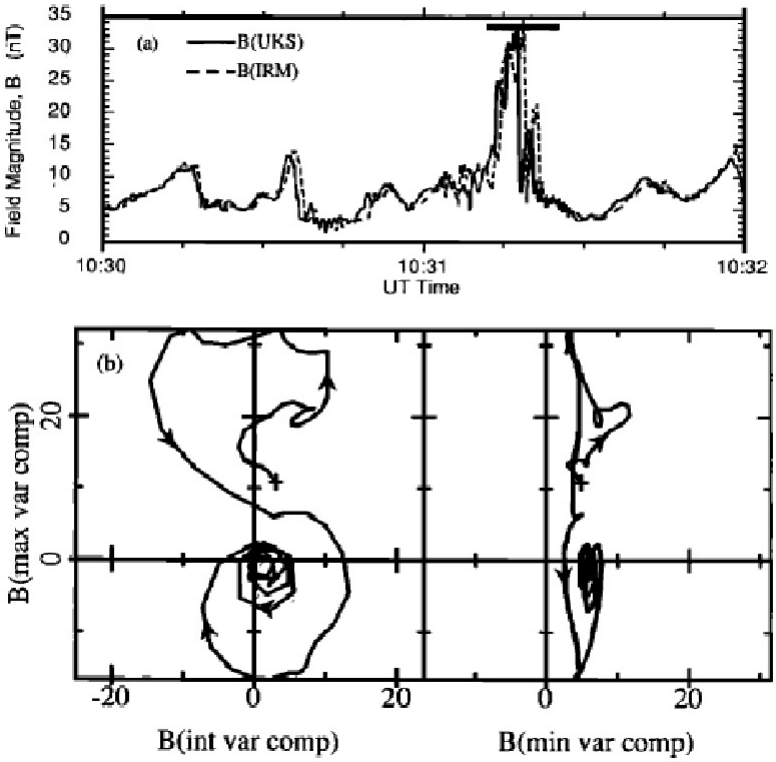

Figure 2.6: Magnetic field magnitude time series plot for an isolated SLAMS as observed by UKS and IRM (top) and hodogram of magnetic field for the same SLAMS event for the interval marked with the overbar (bottom) [figure 6 in Schwartz et al., 1992]

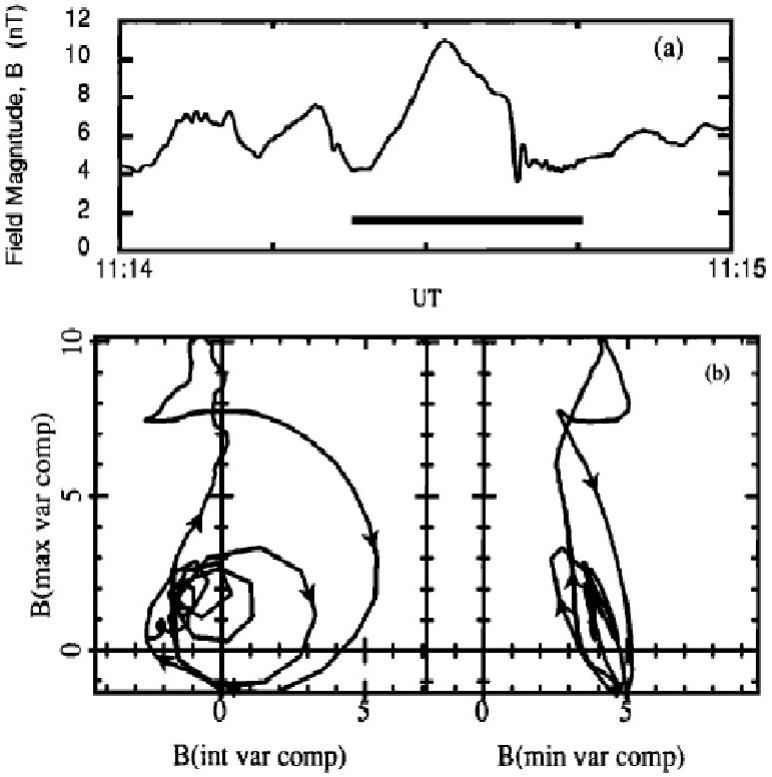

Figure 2.7: Magnetic field magnitude time series plot for an ULF wave as observed by UKS and IRM (top) and hodogram of magnetic field for the same ULF wave for the interval marked with the overbar (bottom) [figure 11 in Schwartz et al., 1992]

There are other authors who feel that the reformation process is not related to these upstream ULF waves (Winske et al., 1990; Thomsen et al., 1990; Onsager et al, 1991a). Winske et al., 1990 argue that the growth of SLAMS is due to the interface instability by the incident ions and the downstream ions. They say that that the reformation process takes place even without the ULF waves, by the generation of the local wave that results from the interface instability.

Onsager et al., 1991a found that both the resonant and the nonresonant instabilities exist in the interaction depending on the density of the reflected ion beam. In the low density portion of the beam, the coupling is due to the resonant instability and in the high density portion, the coupling in due to the non-resonant instability. Hence they argue that the upstream waves are not required in the reformation process, but instead the key ingredients are the reflected ions and the solar wind ions.

Onsager et al., 1991b argue that the relative importance of the ULF waves is related to the strength of the waves, density of the reflected ions, θ_{BN}, and M_A. When the reflected ion density is large (as in simulations of Onsager et al., 1991b), they suggest that it is the ions which determine where reformation occurs. When the reflected ion density is low (10 per cent of ρ_0) it is the waves that play the dominant role.

2.4 Diffuse ions versus reflected ions

The properties of diffuse and reflected ions are discussed in Wilkinson, 2003. Diffuse ions have broad, nearly isotropic angular distributions (Gosling et al., 1978). They have energies of up to 200 keV (Scholer et al., 1979; Thomas, 1985). There have been a number of theories for the origin of these ions. Gosling et al., 1978; Barnes et al., 1980 and Thomsen, 1985 have suggested that diffuse ions evolve from low energy (1 keV) field aligned beams. More recent evidence shows that this may be

unlikely because the alpha particle to proton ratio in the field aligned beams is smaller than in diffuse ions (Ipavich et al., 1988; Fuselier and Thomsen, 1992). Alternatively Fuselier et al., 1995 found that there were similar concentrations of He(2+) ions in diffuse ion distributions as gyrotropic ring beam ion distributions, which evolve from specularly reflected ions. Hence specularly reflected ions may be the seed population for diffuse ions. Some computer simulations disagree with this, and suggest that solar wind thermal ions trapped at the shock, gain energy in electric field and are returned upstream forming the diffuse ion population (Scholer et al., 1998).

Specularly reflected ions are observed at the quasi-parallel shock (Gosling et al., 1982, 1989; Onsager et al., 1990). These ions have energies 1-5 keV. Theoretically, these ions can travel a long way upstream because of the orientation of the IMF lines. However, in reality, the high level of turbulence in the transition zone prevents this from happening. Instead, the specularly reflected ions become gyrotropic (Gurgiolo et al., 1983; Onsager et al., 1990).

Onsager et al., 1990 suggest that specularly reflected beams contribute to ion thermalisation at the quasi-parallel shock. They find that these cold reflected beams are almost always observed near the shock ramp or shock-like structures. The beams they observe seem to be specularly reflected off the shock, since their direction of motion is the same as that expected by specular reflection. They suggest that when θ_{Bn} is locally close to 90 degrees, reflected ions return to the shock and contribute to dissipation. When the θ_{Bn} value does not allow the reflected ions to return to the shock, the ions are observed to spread in velocity space, possibly as a result of interacting with solar wind ions.

In some models, diffuse ions are a key ingredient for the growth of SLAMS and in other models, it is the specularly reflected ions that are important. Authors who highlight the importance of the diffuse ions include Scholer, 1993 and Dubouloz and

Scholer, 1993, 1995, while other authors that think that the specularly reflected ions are important are Burgess, 1989, Onsager et al., 1991a, Scholer and Burgess, 1992. It is a matter of controversy as to which type of ion distribution is more important in the reformation process, although it could be that that both the diffuse ions and specularly reflected ions that play a role. Scholer, 1993 argues that specularly reflected ions cause reformation cycles that have small reformation distances, while diffuse ions cause cycles with larger reformation distances.

2.5 Global hybrid simulations of the bow shock

For studying the bow shock or other parts of the outer magnetosphere ($R \geq 5-6R_E$) that are not much influenced by the ionospheric interactions, global hybrid simulations can be used. Global hybrid simulations attempt to model the full outer magnetosphere system including the kinetic effects of the ions. The hybrid method is described in section 3.3.3. These simulations take into account the curvature and coupling of different parts of the magnetosphere, but the model is simplified. Winske et al., 2003 describe an example of 2-D global hybrid simulations. Earth's magnetic field is represented as a line dipole, forming the center of the Inner Region. The simulation model does not describe this Inner Region. The electric field is set to zero and the magnetic field is kept constant in this region. The solar wind plasma is uniformly distributed throughout the simulation box and also injected consistently at $X = 0$ boundary, and can leave from the other three boundaries. The electric field at the $X = 0$ boundary is set to $V \times B$. The IMF is in $X - Y$ or $X - Z$ plane making an angle with the X axis.

In time, the different regions and boundaries, representing parts of the outer magnetosphere, can be seen. The global hybrid simulations have great potential for

understanding the magnetosphere, as properties within the simulated magnetosphere agree quantitatively with observations. However, in some instances it may be less realistic as it does not include the ionospheric interactions. Often results in one region of the simulation domain may be realistic, while results in another may not be, because plasma and field properties change within the magnetosphere.

Omidi et al., 2005 and Blanco-Cano et al., 2006 have carried out 2-D global hybrid simulations to study the bow shock. Their system was scaled down relative to the real magnetosphere by a factor of about 10. They found sinusoidal, almost parallel propagating waves and compressive, obliquely propagating waves. They showed that the compressive waves do not evolve from sinusoidal waves, as previously suggested, but instead both types of waves are generated by different backstreaming ions. At the moment the validity of comparisons to the Earth's bow shock is not clear due to the reduced dimensionality and unrealistic scaled size.

2.6 Discussion

As has been described in this chapter, the exact mechanism of reformation is still controversial. There is a controversy about the role of ULF waves in the process. While some authors feel that the presence of ULF waves may be crucial for reformation, others have found that reformation can occur even without ULF waves. There is also a difference in opinion about the reformation process with regards to whether it is triggered by instability or related to the reflected ion deflection model. There are some works that highlight the importance of specularly reflected ions in the reformation process and others which suggest that diffuse ions play a more distinctive role.

There could be a number of reasons for the discrepancies between the above results.

It may be difficult to compare results from simulations with spacecraft observations because of differences in parameters. There are difficulties associated with observations. It could be that phenomena being studied may vary in space and time as the spacecraft observes it, which may mean missing vital observations. The observations are often limited by the time resolution of the instruments being used and the number of spacecraft that are in the desired location at the appropriate time.

Similarly there are difficulties associated with simulations. The hybrid simulation method is used in most cases, which treats the electrons as a massless fluid and ions are particles. This means that the electron physics is not completely correct. The simulations are mostly done in 1-D, with some in 2-D and none in 3-D, so it is difficult to model 3-D effects accurately. Most simulations are for an ideal shock, but in reality the bow shock is curved with a foreshock that allows different parts to be in communication with each other. The simulations cover a small range of Mach number, but it is possible that behaviour may be different for stronger shocks.

Chapter 3

Simulation techniques

In this chapter we describe some of the techniques used to study plasmas with simulations, concentrating on the problem of wave-particle interaction. We first describe the test particle method and show results for the interaction of particles with a magnetic pulse. Then we briefly describe the self-consistent simulation of plasmas, concentrating on the hybrid method.

3.1 Test particle modelling: Method

3.1.1 Equation of motion

A test particle model is one where the particles do not have an affect on the electromagnetic fields. This model uses the equation of motion, which is defined from the Lorentz force equation. This is the force acting on a charge q of mass m travelling at a velocity $\mathbf{v}$ in vicinity of electric field $\mathbf{E}$ and magnetic field $\mathbf{B}$.

$$\mathbf{F} = q(\mathbf{E} + \mathbf{v} \times \mathbf{B}) \tag{3.1}$$

The $\mathbf{F} = q\mathbf{E}$ part of the Lorentz force is in the direction of the electric field for a positive charge and the magnetic force $\mathbf{F} = q(\mathbf{v} \times \mathbf{B})$ is perpendicular to both the velocity and the magnetic field. The magnitude of the magnetic force is $F = qvsin\theta$ where θ is an angle less than 180 degrees between the magnetic field and velocity. Thus the magnetic force on a particle that is stationary or moving parallel to the magnetic field is zero. Using Newton's law of motion and assuming negligible collisions and gravitational force, we can define the equation of motion from the Lorentz force.

$$m\frac{d\mathbf{v}}{dt} = q(\mathbf{E} + \mathbf{v} \times \mathbf{B}) \tag{3.2}$$

3.1.2 Numerical methods to solve equation of motion

Numerical methods are used to approximate the solution to the equation of motion at discrete times $t_1, t_2...t_n$. We can define the time step Δt as the difference $t_{n+1} - t_n$. One method used to solve the equation is Euler's method which, given the solution at time step n, approximates the solution at time step $n + 1$.

$$y_{n+1} = y_n + \Delta t f(t_n, y_n) \tag{3.3}$$

This is an explicit method since the RHS does not depend on y_{n+1}. This method converges to the true solution as Δt decreases. The method is simple to implement, but requires very small time steps. Another method is the Runge-Kutta method, where we can compute the function $f(t, y)$ at several points within the time interval. For example, a second order Runge-Kutta method is as follows.

$$y_{n+1} = y_n + \frac{\Delta t}{2}(k_1 + k_2) \tag{3.4}$$

$$k_1 = f(t_n, y_n) \tag{3.5}$$

$$k_2 = f(t_n + \Delta t, y_n + \Delta t k_1) \tag{3.6}$$

The Runge-Kutta method is also explicit since k_1 does not depend on k_2 and neither k_1 nor k_2 depend on y_{n+1}.

3.2 Test particle modelling: Interaction with magnetic pulse

3.2.1 Overview

In this section we discuss the interaction of a static pulse with a ion reflected at the quasi parallel shock. As noted by Kuramitsu and Hada, 2008, it should not be assumed that the interaction between the SLAMS and reflected ion is adiabatic since typical scale of SLAMS is 3000 km, comparable to the ion gyroradius of 4000 km when the magnetic field is 5 nT (Schwartz et al., 1992, Giacalone et al., 1993). Also, the magnetic field changes within the SLAMS are 1000 km or less, which is much less than the SLAMS scale (Lucek et al., 2004). Therefore the ion would feel a rapid change in the field, and the interaction may be non-adiabatic. For this reason, we investigate the non-adiabatic behaviour of the interaction using the Kuramitsu and Hada, 2008, model, in this section. We particularly look at the enhanced non-adiabatic reflection.

Kuramitsu and Hada, 2008, described a model that they use in order to study particle acceleration and the scattering mechanism by looking at the interaction between an ion and a magnetohydrodynamic (MHD) pulse. Their model is used to look at both adiabatic and non-adiabatic behaviour. They plotted the particle pitch angles before and after the interaction and described the different behaviour in small and large wave packet width regimes. They also generated plots of the reflection probability for different wave packet widths. We carry out an extension to their work by generating plots of reflection probability for different values of the parameters to study the enhanced non-adiabatic reflection.

Although extensive work has been done on reflection of particles from a MHD pulse in the adiabatic regime, relatively less focus has been on reflection in the non-adiabatic regime. In this section we outline some of the results of the reflection process with both the conservation and non-conservation of the magnetic moment with a pulse, as carried out by Kuramitsu and Hada, 2008 and from our own study.

3.2.2 Model of Kuramitsu and Hada, 2008

The mirror reflection of a particle can be described by the adiabatic invariant of magnetic moment μ_m.

$$\mu_m = \frac{m v_\perp^2}{2B} \tag{3.7}$$

Here m is the mass of the particle, $v_\perp$ is the perpendicular component of the particle velocity to the magnetic field and B is the strength of the magnetic field. The magnetic moment is conserved if the fields experienced by the particle change at a rate much slower than the gyrofrequency. The invariance of the magnetic moment can

be rewritten in terms of the particle pitch angle α, which is the angle between the magnetic field and the particle velocity. When the magnetic field strength changes from region 1 to region 2, the particle's pitch angle also changes in order to conserve the magnetic moment.

$$\frac{\sin^2 \alpha_1}{B_1} = \frac{\sin^2 \alpha_2}{B_2} \tag{3.8}$$

$$\frac{\sin^2 \alpha}{B} = \frac{1}{B_m} \tag{3.9}$$

Here B_m is the magnetic field where the particle is reflected, that is, where $\alpha = \pi/2$. We can define the critical pitch angle in terms of the maximum field strength B_{max} and the background magnetic field B_0.

$$\sin^2 \alpha_c = \frac{B_0}{B_{max}} \tag{3.10}$$

If the pitch angle is less than the critical pitch angle, then particle is transmitted through the wave packet and if the pitch angle is larger than the critical angle, then the particle is reflected by the wave packet. If the particle's magnetic moment is conserved then the behaviour is described as being adiabatic. For this, the field must change relatively slowly as compared to the particle's gyroradius.

Kuramitsu and Hada, 2008, studied adiabatic and non-adiabatic behaviour by following numerically the trajectory of a particle as it interacts with a single wave packet or pulse. This pulse is a planar structure with a normal in the x direction with field perturbations in y and z directions. The pulse is Gaussian and described by a complex function.

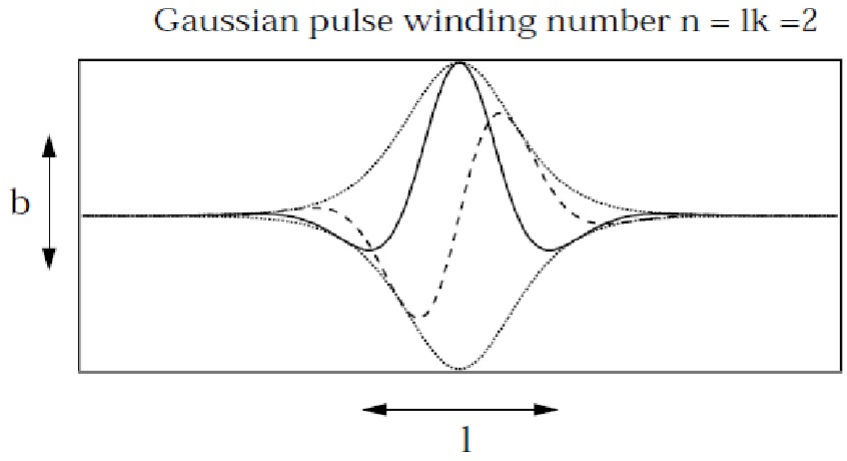

Figure 3.1: Gaussian pulse used in this model. The B_y and B_z components are shown as solid and dashed curves, and the envelope (dotted) is the magnetic field envelope. [figure 1 in Kuramitsu and Hada, 2008]

$$\delta B = By(x) + iBz(x) = Aexp[-(x/L)^2 + ikx + i\theta] \tag{3.11}$$

Here A is the amplitude of the wave, L is the width of the wave packet, k is the wave number of the carrier wave and θ is phase constant of the carrier wave. Figure 3.1 shows the Gaussian pulse used in the model. The Gaussian envelope is due to the $e^{-x^2/L}$ term, the cosine wave shape is due to the e^{ikx} term and the pulse phase is changed by the $e^{i\theta}$ term. The components B_x, B_y and B_z are then the background magnetic field, the real part of the complex function and the imaginary part of the complex function respectively.

In this model, all the quantities were normalised using the magnitude of the particle velocity V, the background magnetic field B_0 and the gyrofrequency $\Omega = eB_0/mc$. The normalised wave amplitude is $b = A/B_0$ and the normalised wave packet width is $l = L\Omega/V$. They also define the cosine of the pitch angle $\mu = \cos\alpha$ and the

inverse of the normalised wave packet width $\zeta = 1/l$. The winding number $n = Lk$ is the number of rotations that the transverse magnetic field makes within the wave packet. The gyrophase angle ϕ is the angle between the perpendicular velocity and z direction.

3.2.3 Methodology

In our simulation, particles were injected with different pitch angles and gyrophase angles towards the pulse from the positive side of the pulse. The particles were studied for $-5l < x < 5l$ along x. If a particle stopped before reaching the endpoint of the pulse, the particle was reflected by the pulse. However, if the particle went beyond the endpoint of the pulse, the particle was transmitted through it. The particles' pitch angles and gyrophase angles before and after the interaction were found. The initial velocity components are in terms of the pitch angle and the gyrophase angle. The output of the simulation gives the cosine of the outgoing pitch angle $\mu_{out} = \cos\alpha_{out}$.

$$V_x = V_{\parallel} = V\cos\alpha \tag{3.12}$$

$$V_y = V_{\perp}\sin\phi = V\sin\alpha\sin\phi \tag{3.13}$$

$$V_z = V_{\perp}\cos\phi = V\sin\alpha\cos\phi \tag{3.14}$$

The values of μ_{in} and ϕ were varied to investigate their effect on the value of μ_{out} at the end of the run. This was repeated for a number of different values of the wave packet width l. Then the reflection probability was calculated and plotted for

different μ_{in} and l values.

3.2.4 Results of Kuramitsu and Hada, 2008

In the plots of Kuramitsu and Hada, 2008, lines of $\mu_{in} = \pm\mu_{out}$ show the complete conservation of the first adiabatic invariant. When l is large, that is, the wave packet width is large, the particle feels the change in the field slowly. However when l is small, the particle feels a rapid change of field and that is the reason that the interaction becomes non-adiabatic. This can be seen in the plots of μ_{in} against μ_{out} for n=0 and b=2 in figure 3.2.

The plot with large l, (a), shows that the interaction corresponds well with adiabatic theory. Particles in the loss cone are transmitted through the pulse and those outside the loss cone are reflected by the pulse. The plot with smaller l, (b) shows that the adiabatic invariant breaks down, as some particles within the loss cone are reflected and some particles outside the loss cone are transmitted. Plots with even smaller l, (c), (d) and (e), show that there is little adiabatic interaction and the plot with smallest l, (f) shows that the particles are hardly reflected at all.

The reflection probability was found for different pitch angles of the particle. The plots in figures 3.3 - 3.5 show the reflection probability as a variable of μ (the cosine of the pitch angle) and ζ (the inverse of the pulse width). The shaded scale from 0-1 is the reflection probability with 1 being complete reflection and 0 being no reflection. The plots show different trends for small ζ (large pulse width l) and large ζ (small pulse width l).

When ζ is small, the pulse width is large, the particles feel the change in the field relatively slowly and hence the interaction can be described as adiabatic. For pitch angles less than the critical pitch angle, there is complete transmission and the prob-

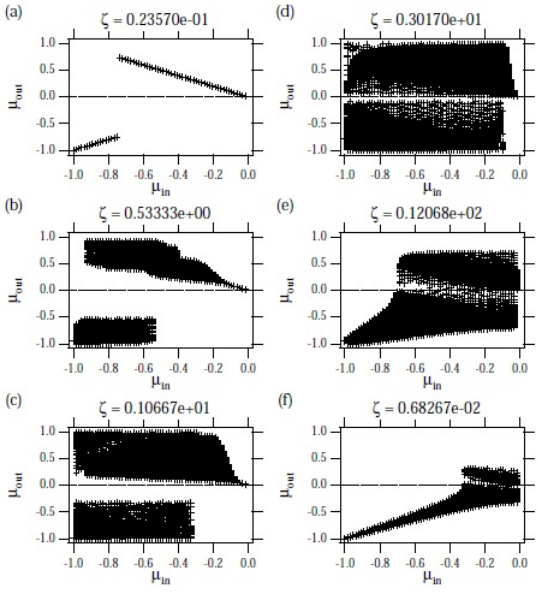

Figure 3.2: Plots of particle pitch angle before and after the interaction with pulse parameters n=0, b=2. Note that the value for ζ in panel (f) is in error in the original paper and should be $\zeta = 0.68267e + 2$. [figure 2 in Kuramitsu and Hada, 2008]

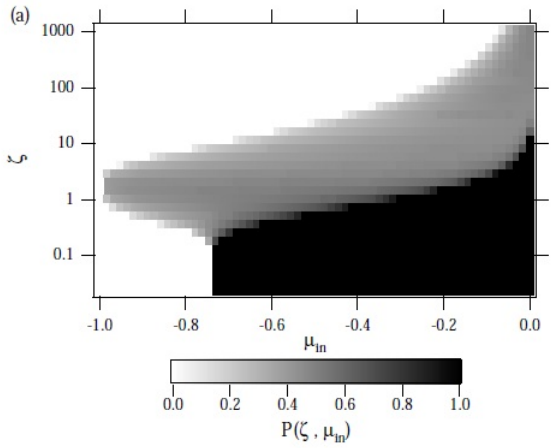

Figure 3.3: Plots of reflection probability $P(\zeta, \mu_{in})$ with pulse parameters n=0, b=2. [part of figure 4 in Kuramitsu and Hada, 2008]

ability of reflection is zero, while for pitch angles greater than the critical pitch angle, there is complete reflection. However, when ζ is large, the pulse width is small, and so the particles feel the change in the field relatively rapidly. In this case, adiabaticity breaks down and there is some reflection and some transmission depending on the gyroangle of the particles. Similar reflection probability plots were done for a larger pulse amplitude and winding number. It was found that there is some enhanced non-adiabatic reflection around $\zeta \sim 1$ in some cases. This is discussed in the next subsection.

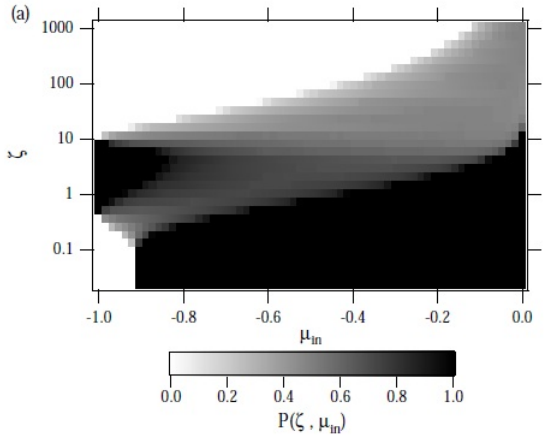

Figure 3.4: Plots of reflection probability $P(\zeta, \mu_{in})$ with pulse parameters n=0, b=6. [part of figure 5 in Kuramitsu and Hada, 2008]

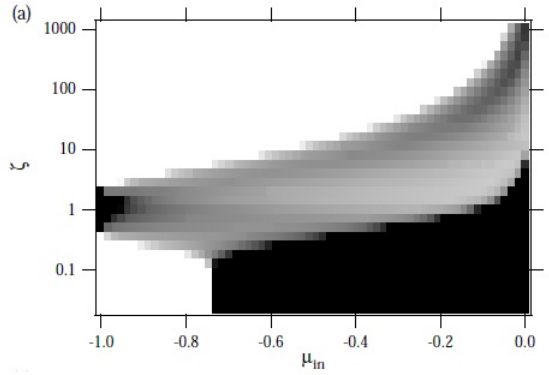

Figure 3.5: Plots of reflection probability $P(\zeta, \mu_{in})$ with pulse parameters n=2, b=2. [part of figure 8 in Kuramitsu and Hada, 2008]

3.2.5 Results of our simulation - enhanced non-adiabatic reflection

As an extension to the work of Kuramitsu and Hada, 2008, we looked at the enhanced non-adiabatic reflection in more detail. In addition to the complete reflection due to the adiabatic behaviour or conservation of the magnetic moment, there is also enhanced reflection related to non-conservation of the magnetic moment at around $\zeta = 1.0$, $\mu = -1.0$ for beam particles. We varied the parameters n and b and plotted the reflection probability for the case n=2, b=1, 2 and 4 and for the case n=-2, b=1, 2 and 4. We found the following interesting results.

Comparing figures 3.6 and 3.7 shows that enhanced non-adiabatic reflection occurs only for positive winding number n. In this case, as pointed out by Kuramitsu and Hada, there is a non-linear cyclotron resonance which is not present for negative n. Positive n corresponds to the sense of rotation of the magnetic field matching the sense of gyration of the incident particle. The non-adiabatic reflection probability depends on the pulse amplitude, starting at 1.5-2.0 B_0 (for n=2) and increasing rapidly with increasing amplitude. The implication of these results is that a pulse with the correct sense of rotation will tend to reflect incident ions, provided that the pulse is significantly large.

3.2.6 Summary

Kuramitsu and Hada, 2008, state that it should not be assumed that the interaction between the SLAMS and reflected ion is adiabatic since typical scale of SLAMS is 3000 km, comparable to the ion gyroradius of 4000 km when the magnetic field is 5 nT (Schwartz et al., 1992, Giacalone et al., 1993). Also, the magnetic field changes within the SLAMS are 1000 km, which is much less than the SLAMS scale (Lucek et al.,

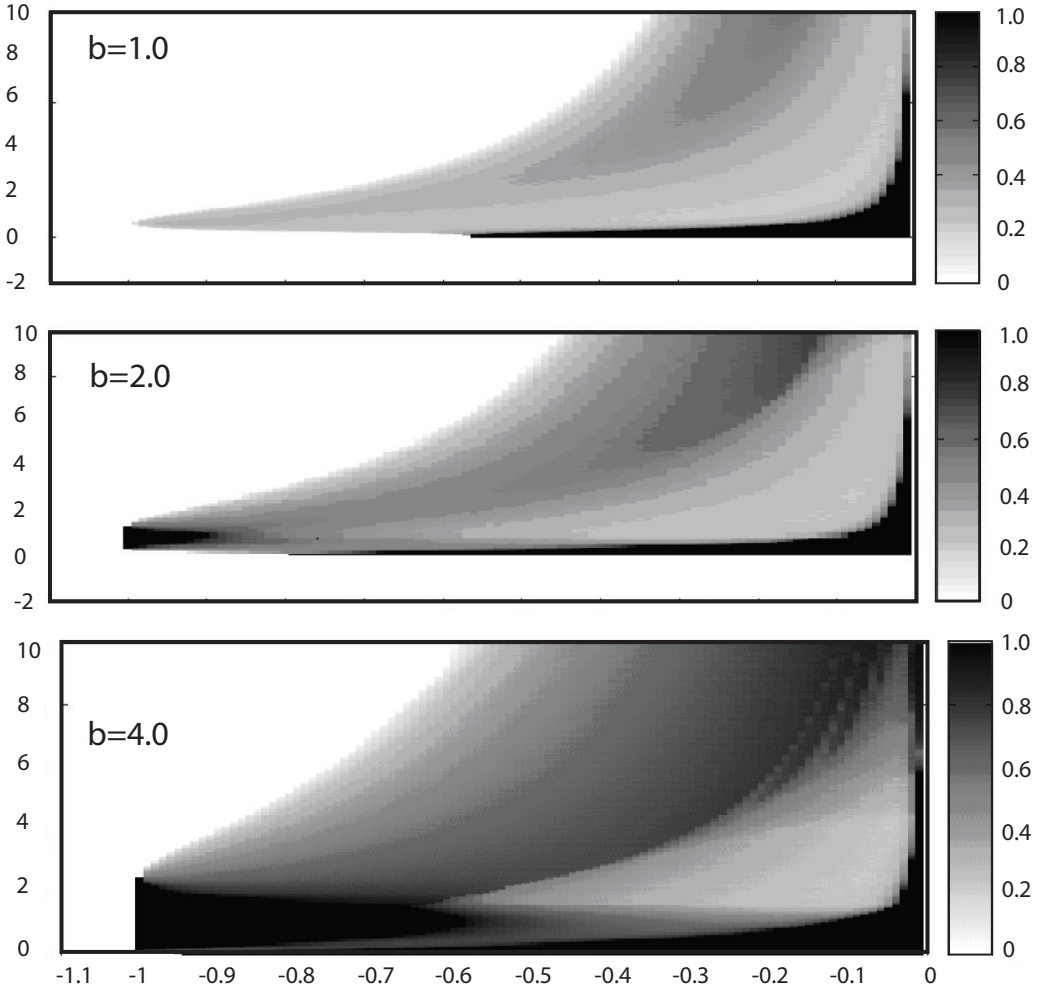

Figure 3.6: Reflection probability plots for n=2, where the greyscale is the reflection probability, the vertical axis is ζ (the inverse of the pulse width), and the horizontal axis is μ (the cosine of the pitch angles) of the particles. The plots are for b=1.0, b=2.0 and b=4.0 from top to bottom

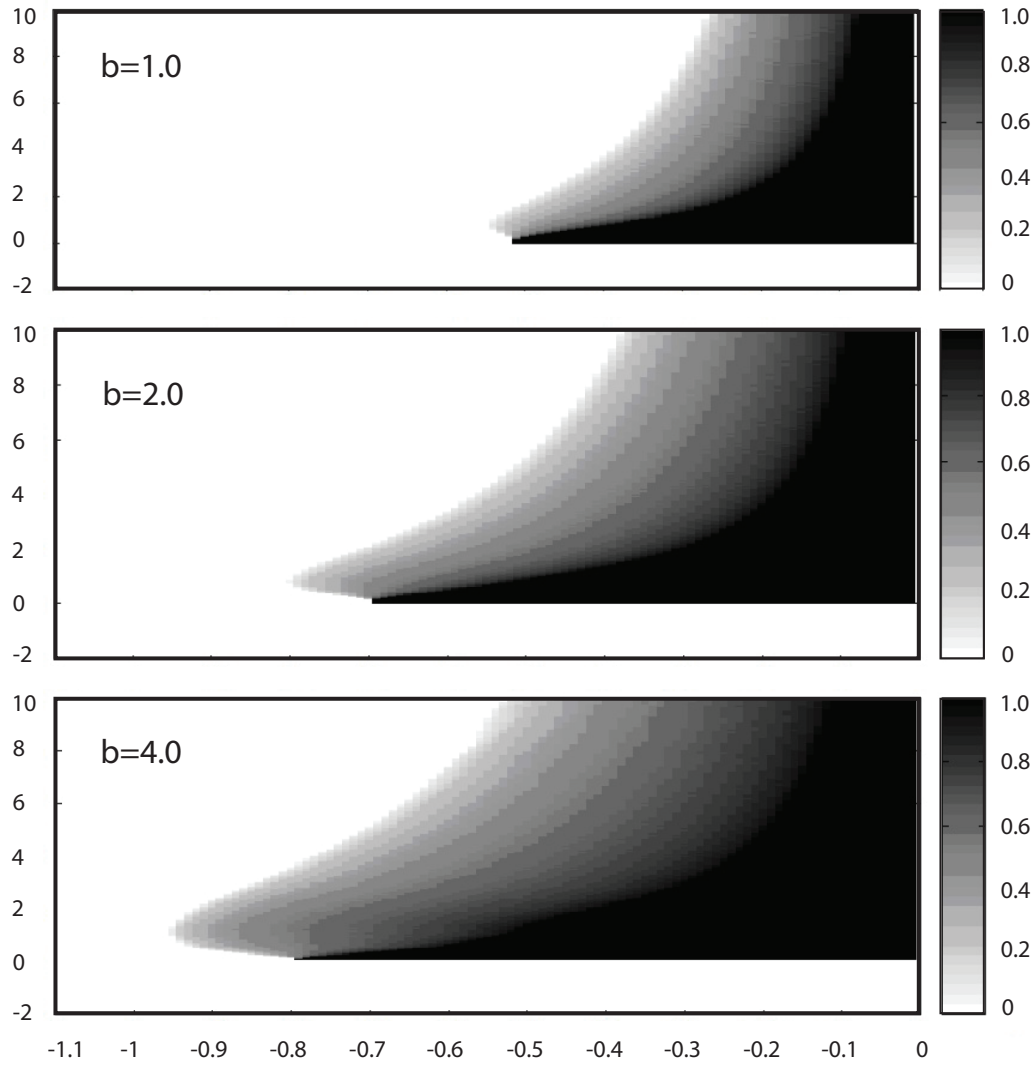

Figure 3.7: Reflection probability plots for n= - 2, where the greyscale is the reflection probability, the vertical axis is ζ (the inverse of the pulse width), and the horizontal axis is μ (the cosine of the pitch angles) of the particles. The plots are for b=1.0, b=2.0 and b=4.0 from top to bottom

2004). Therefore the ion would feel a rapid change in the field, and the interaction may be non-adiabatic. In this chapter we have described some of the results of Kuramitsu and Hada, 2008, showing the adiabatic and non-adiabatic behaviour of the interaction. We also describe the results of our simulation which is an extension of their work, where we focus on the enhanced non-adiabatic reflection.

We have plotted the reflection probability for the case of pulse winding number n=2, and pulse amplitude of b=1, 2 and 4, and for the case of pulse winding number n=-2 and pulse amplitude of b=1, 2 and 4. We find that the enhanced non-adiabatic reflection at around $\zeta = 1.0$, $\mu = -1.0$ increases with pulse amplitude. For a winding number of 2, this enhanced reflection starts at the amplitude of 1.5-2.0 B_0. We also find that this enhanced non-adiabatic reflection does not exist for negative winding number such as n=-2. This is because for positive n, there is resonance of the particles with the pulse, but this is not the case when n is negative.

3.3 Self-consistent plasma simulation

3.3.1 General principle

The simulations used in Chapter 4 are one-dimensional hybrid simulations, allowing for one spatial direction in shock normal direction and full three-dimensional velocities and magnetic and electric fields. The hybrid method has been much used to study quasi-parallel shocks since it accounts for the difference in time and length scales between the electrons and the ions by treating the ions as particles and electrons as a fluid. The equations used in the hybrid code are described in the following section.

Using the hybrid simulation, the initial formation of the shock can be modelled using

different techniques. One technique is to use Rankine-Hugoniot relations which define the upstream and downstream conditions. The shock is then a thin transition between the upstream and downstream regions and the system evolves in time. Another technique is to have the solar wind flowing towards the right wall of the simulation domain. The solar wind then gets specularly reflected off the wall and the shock forms as a result of the interaction between the incident and reflected ions.

However, we have used a different approach, so that we can study the wave-particle dynamics at the shock by varying the different parameters. We have a pulse propagating at Alfven velocity to represent an ULF wave, and then for the specularly reflected ion case, particles are injected from the right hand side of the pulse as if they were specularly reflected from the shock. In the diffuse ion case, the ions are modelled over a spherical shell moving at random velocities over the entire simulation domain. These initial conditions are described in more detail later. The intention is to study the dynamics of particle-pulse interaction without the full complexity of a shock simulation, so that basic processes can be identified. The simulation is done in the frame moving with the upstream flow, so that the background ions initially have zero velocity but have thermal motions. This section describes the details of the set up of the pulse, the specularly reflected ions and the diffuse ions.

3.3.2 Fluid, particle and hybrid methods

The fluid method, also known as Magnetohydrodynamics, is where plasma is treated as a conducting fluid with electric and magnetic forces and no kinetic effects are involved. The main equations used are the conservation of mass, conservation of momentum and equation of state. These equations can be derived from the Vlasov equation, which describes a collisionless plasma using kinetic description. Since the plasma is neutral on the scales of the fluid, the electric force is negligible. For the

quasi-parallel shock, where we need to study particle trajectories, wave growth and instabilities, the fluid method is inappropriate as it does not involve kinetic effects.

The basis for the particle method is the Vlasov equation which includes the distribution function of the particles in 6-dimensional phase space. This method often involves Particle-in-cell (PIC) numerical technique which is used to solve partial differential equations. Ion and electron macro-particles are followed in continuous phase space. Moments and distribution function are computed on a Eulerian mesh to solve self-consistent field equations. The particle method has to resolve the electron motion so needs very small time steps. This is a very large computational task and it is almost impossible to simulate large scales of quasi-parallel shock, which is on ion scales (100's of ion gyro-radii).

The hybrid method is a perfect alternative for simulating the quasi-parallel shock, as it treats the ions kinetically and electrons as a fluid. This method can be advanced on time step related to ion time scales, saving a lot of computational work. The next subsection describes the equations used in this method. The hybrid simulation that we use is written by Burgess, based on code from Krauss-Varban. The simulation uses a field solver with predictor-corrector and sub-stepping to improve accuracy.

3.3.3 Hybrid method equations

As outlined in Winske and Omidi, 1996, kinetic simulations involve solving Maxwell's equations based on source terms such as plasma density and currents. The particles are advanced in time a small amount by a time step to collect the source terms that are used to solve for the fields. The fields are found, and the particles are advanced again so that new source terms can be obtained. This process of advancing the particles to obtain the source terms and determining the fields is repeated over many time steps

until the simulation is run over the desired time interval. In the Maxwell equations **E** and **B** are the electric and magnetic fields respectively. Then, ρ is the charge density, **J** is the current density and c is speed of light.

Poisson's Law is:

$$\nabla \cdot \mathbf{E} = \frac{\rho}{\varepsilon_0} \tag{3.15}$$

Gauss's Law is:

$$\nabla \cdot \mathbf{B} = 0 \tag{3.16}$$

Faraday's Law is:

$$\nabla \times \mathbf{E} = -\frac{\partial \mathbf{B}}{\partial t} \tag{3.17}$$

Ampere's Law is:

$$\nabla \times \mathbf{B} = \mu_0 \mathbf{J} + \frac{1}{c^2}\frac{\partial \mathbf{E}}{\partial t} \tag{3.18}$$

These Maxwell's equations are used in the hybrid code except for Poisson's Law, which is replaced by the electron momentum equation. Since the electrons are treated as a massless fluid, mass of electron $m_e = 0$ makes the left hand side of the momentum equation zero and we can rearrange to solve for the electric field. In this equation, P_e is the electron pressure, e is the electronic charge, η is the resistivity (coupling between the electrons and ions), V_e is the electron flow velocity and V_i is the ion flow velocity.

$$\mathbf{E} = -\mathbf{V}_e \times \mathbf{B} - \frac{\nabla P_e}{e n_e} + \eta e n_e (\mathbf{V}_i - \mathbf{V}_e) \tag{3.19}$$

Ampere's Law is used to eliminate V_e in the electron momentum equation and Faraday's Law is used to advance the magnetic field in time. Apart from Maxwell's

equations and the electron momentum equation, an equation of state is also required to advance the electrons in electron pressure or temperature. This can be adiabatic or isothermal.

The ions are treated kinetically so that each ion of charge q_i and mass m_i is subject to the equation of motion.

$$m_i \frac{d\mathbf{V}_i}{dt} = q_i(\mathbf{E} + \mathbf{V}_i \times \mathbf{B}) \tag{3.20}$$

$$\frac{d\mathbf{x}_i}{dt} = \mathbf{V}_i \tag{3.21}$$

3.3.4 Limitations and advantages of hybrid method

Since the hybrid method does not treat electrons kinetically, these simulations save much computational work. The hybrid method allows simulations to be run for longer since they can be advanced on time step related to ion time-scales rather than electron time-scales and also on larger spatial scales so can have larger boxes. They are perfect for studying the quasi-parallel shock which is much larger than the electron scales. As this method treats ions kinetically, this method can be used to study the growth or damping of upstream and downstream waves, which are important at the quasi-parallel shock.

However, there are some limitations of the hybrid method. It cannot resolve electron motion since it does not include electron kinetic effects. As waves grow and steepen, they may produce structures with shorter scale lengths, and it may be important to resolve these at electron scales. Hence, the hybrid method may miss some of the intrinsic details and it is not an appropriate method to use for studying electron

cyclotron damping or electron instabilities.

Chapter 4

Self-consistent plasma simulation

4.1 Overview

Specularly reflected ions are particles which have their component of velocity normal to the shock reversed as they encounter the shock. These ions have been observed at the quasi parallel shock (Gosling et al., 1982, 1989; Onsager et al., 1990) and have energies of 1-5 keV. Depending on the angle that these ions make with the magnetic field lines upon reflection, they can either be field aligned beams or gyrating beams. Diffuse ions have broad, nearly isotropic angular distributions (Gosling et al., 1978). They have energies in a range of 10-200 keV. The origin of these ions is discussed in detail in Chapter 2. In this chapter we discuss both the specularly reflected ions, which can be field aligned beams or gyrating beams, and the diffuse ions.

The scenario modelled here is the interaction between the ions and a ULF wave. This interaction is thought to result in the growth of the pulsations, which ultimately leads to shock reformation as the pulsations propagate towards the shock and grow in amplitude. The reflected ion deflection mechanism and the diffuse ion mechanism,

whereby the ions cause the growth of the pulsations, are discussed in Chapter 2. In this chapter we describe the results of our simulation as they provide a further insight into the two mechanisms. Variables that are explored are the velocities of the ions, their density, the angle between the ion trajectory and magnetic field line and the initial amplitude of the pulse. Hence, it should be possible to determine the signatures of the process.

The simulations used here are one-dimensional hybrid simulations, allowing for one spatial direction in the shock normal direction and full three-dimensional velocities and magnetic and electric fields. The hybrid method has been much used to study quasi-parallel shocks since it accounts for the difference in time and length scales between electrons and ions, by treating the ions as particles and the electrons as a mass-less fluid. Our simulation model has similar initial conditions for the pulse as in the Kuramistu and Hada, 2008 model, but the use of the hybrid simulation allows for the self-consistent evolution of particles and fields. This is important for observing the growth of the pulse. Although the simulation technique is described in detail in Chapter 3, we start by giving a brief outline of the procedure that we used for both the reflected ion and the diffuse ion cases. After this we discuss the results of the specularly reflected ion case and then the results of the diffuse ion case.

We will present results for different scenarios of injected ions and a number of different initial parameters. The aim is to describe the range of behaviour that is seen in the pulse-beam coupling problem and thus to identify the conditions which are optimal for fast growth of a magnetic pulsation. In this way we can gain insight into the production mechanism of pulsations in the complex situation of a realistic shock.

4.2 Pulse set up

Kuramitsu and Hada, 2008 studied the interaction of ions with an isolated pulse using test particles. Our simulation has similar initial conditions for the pulse. The pulse is propagating in the x direction. The pulse is a Gaussian wave as in work of Kuramitsu and Hada, 2008.

$$\delta B = By(x) + iBz(x) = Aexp[-(x/L)^2 + ikx + i\theta] \tag{4.1}$$

Here A is the amplitude of the wave, L is the width of the wavepacket, k is the wavenumber of the carrier wave and θ is phase constant of the carrier wave. k can be written as $k = n/L$ where n is the winding number or the number of rotations that the transverse magnetic field makes in the pulse.

Kuramitsu and Hada originally used a system with the background magnetic field in the x-direction. We use an orientation of the magnetic field as at a quasi-parallel shock corresponding to an angle $\theta_{Bn} = 30°$. The background magnetic field B_0 has (x, y) components $(B_0 \cos\theta_{Bn}, B_0 \sin\theta_{Bn})$. The propagation of the pulse is assumed parallel to the field at the Alfven speed, with the corresponding x and y component of the propagation speed by projection. The ion velocity is varied through the magnetic pulse according to the relation between magnetic field and velocity for an Alfven wave, ie $\vec{B}_\perp/B_0 = \mp\vec{V}/v_A$, where the signs $\mp$ correspond to propagation towards $\pm x$-direction. Since the simulations we perform are one dimensional, the effect is that the pulse propagates in the x-direction at the speed $V_A \cos\theta_{Bn}$. The pulse represents the ULF wave and is centred at $x = 50c/\omega_{pi}$ in the simulation domain of size $100c/\omega_{pi}$.

The simulation frame corresponds to the solar wind flow frame, with the imposed pulse being an Alfven-like perturbation propagating in the x-direction. Beam injection is in the -x direction (leftward), consistent with assuming a shock normal in the -x direction. Our beam injection velocities are chosen using a nominal Alfven Mach

number of 5, so that injection at $v_x = -5v_A$ corresponds to zero velocity in the shock frame and velocities $v_x < -5v_A$ correspond to escape from the shock. We use initial conditions for the pulse such that it is propagating to +x in the plasma frame with RH spatial polarization for positive winding number. B_x is positive so the wave polarization would be referred to as LH. In the nominal shock frame the pulse is carried towards the shock by the super-Alfvenic flow. At the Earth's foreshock, waves generated by the resonant ion beam instability travel in the beam direction and are RH polarized. However, they too are convected backwards towards the shock, reversing their sense of polarization in the shock frame. The net effect is that, although the pulse in our simulations is not travelling away from the shock in the plasma frame, ions escaping from the shock experience the same left hand sense of rotation (for positive winding number) in the magnetic field as for foreshock waves at the Earth's bow shock.

4.3 Injected ion distribution

A beam of ions is injected at $x = 80-85c/\omega_{pi}$ and these travel in the -x direction. The injected ion distribution is chosen so that it has about the same energy corresponding to reflected solar wind that is backstreaming at a $M_A = 5$ shock. The beam is made up of two parts: the injection velocity that moves the beam in the -x direction parallel to the magnetic field and the shell velocity which changes the pitch angle of the particle. The particles are on a shell in velocity space centred on origin in de Hoffmann-Teller (HT) frame. The injection velocity is relative to the simulation frame, which corresponds to the solar wind speed so that with no shell velocity the particles move along the magnetic field direction. The shell velocity corresponds approximately to that of specular reflection, with a narrow shell width of $0.2V_A$. The orientation of the injection and shell velocities are shown in figures 4.1 and 4.2.

Figure 4.1 shows the velocity space regions occupied by the different ion populations which are important at the quasi-parallel shock. This is shown in the normal incidence shock frame, where the shock normal vector points towards the upstream region, and the upstream flow (marked $\vec{V}_{sw}$) is normal to the shock surface. Also marked on the figure is the origin of the de Hoffmann-Teller frame O_{HT}, and in this frame the inflow flow is aligned with the upstream mangetic field so the motional electric field is zero. Thus in this frame the energy of particles interacting with the shock, viewed as a time steady structure, is constant. The populations of particles which can be explained in this context are specular reflected ions (which reverse their normal component of velocity), and cold field-aligned beams (which have small pitch angle range close to the magnetic field direction). Also marked is the region in velocity space with a parallel velocity orientated away from the field, ie corresponding to the general class of backstreaming ions. In addition we indicate an isocontour for energetic diffuse ions which are isotropic in the plasma frame. These particles gain energy by interacting with the time dependent waves upstream and downstream of the shock, and so gain more energy than simply would be predicted by the constant energy surface in the de Hoffmann-Teller frame.

Figure 4.2 shows the velocity space of the injected beam particles and the parameters which are used to specify it. Injected particles lie on a spherical shell with velocity magnitude V_{shell}, or portion of that shell specified by given ranges in the pitch angle α and gyrophase angle ϕ. In addition to the spherical shell, it is possible to displace it along the magnetic field direction by an injection velocity $V_{injection}$. By changing the parameters of the injected population it is possible to model different types of initial populations, as indicated above. The parameter values used in the different simulations are listed for each run in Table 4.1.

The magnetic field is directed into the shock and is at an angle of 30 degrees to the shock normal, chosen as typical of quasi-parallel shocks. The shock normal is in -x

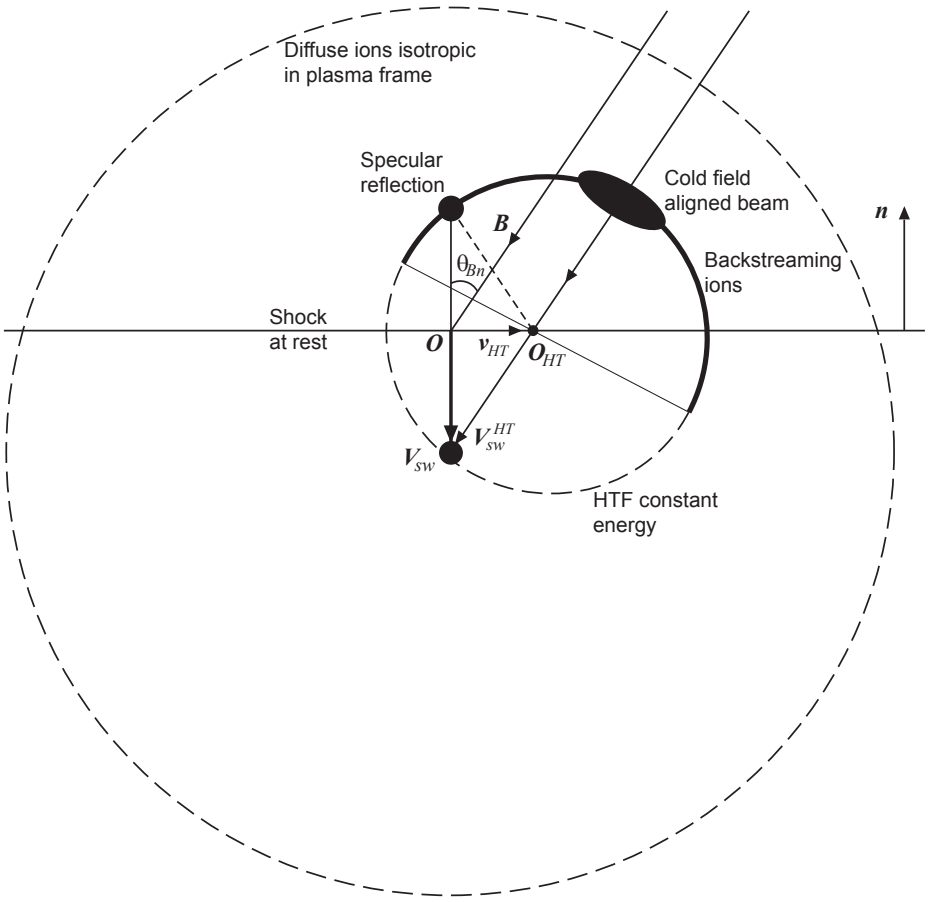

Figure 4.1: Diagram showing injection velocity from de Hoffmann Teller origin and shell velocity and types of ion distributions. The simulations are carried out in the solar wind frame. [Schematic by Burgess]

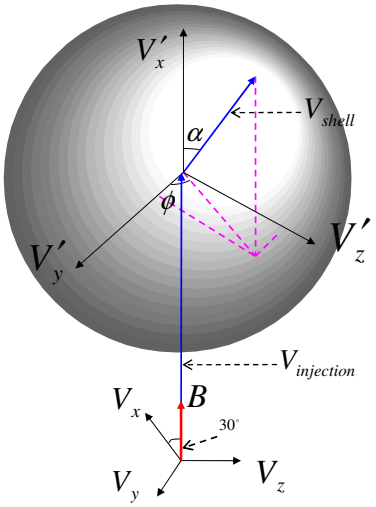

Figure 4.2: Figure shows orientation of shell velocity and injection velocity where the V' coordinates are rotated by 30 degrees from the V_x axis.

direction. The pitch angles were chosen specifically to study different ion distributions. To look at backstreaming ions, which are those that can arrive upstream from the shock, we used a range of 110 - 180 degrees. To look at field aligned ions, we used a range of 150 - 180 degrees and to look at gyrating ions we used a range of 110 - 130 degrees. Specularly reflected ions would have limited range in pitch angle and initially would also be limited in gyrophase angle, but would spread out in time and space.

The time is in units of the inverse of the ion gyrofrequency $\Omega = eB_0/m$, where e is the electronic charge, B_0 is the initial magnetic field and m is the mass of ion. Distances are in units of the ion inertial length c/w_{pi}, where c is the speed of light and w_{pi} is the

ion plasma frequency. Consequently, the velocity is in units of the Alfven velocity.

4.4 Diffuse ion distribution

Diffuse ions at the shock are roughly isotropic in the plasma frame. At the foreshock, they have a low normalized density of 0.01 or less relative to the solar wind density, while at the shock transition zone their normalized density may reach 0.1 - 0.2 in bursty regions. In order to look at the diffuse ions case, we model diffuse ions travelling at 25-30 V_A in random directions distributed across the whole simulation box. The runs that are carried out are without a density gradient in the diffuse ions. We use a uniform initial density throughout the simulation box. The initial density we use is up to 0.1 or 0.2, which is unrealistically high, but is used to observe the trends in the results more clearly, as the coupling with the pulse is much weaker in the diffuse ions case than for the backstreaming ion case. Close to the shock transition, diffuse ions are sometimes seen to be shifted relative to the plasma frame, so we add the effect of a shift in velocity, that is $v_{\parallel} = -2.5$. This may be a little high, but allows us to observe the effects.

The diffuse ions are modelled in a spherical shell, as in previous schematics. As outlined by Weisstein, it should be noted that it is incorrect to select spherical coordinates α and ϕ from uniform distributions of α in range $[0, \pi]$ and ϕ in range $[0, 2\pi]$, as the area element $d\Omega = \sin\alpha d\phi d\alpha$ is a function of α, and so the particles would be bunched near the poles. Figure 4.3 shows the incorrect way and correct way to model points on a sphere. In order to model the particles such that any small area of the sphere has same number of particles, we need u and v to be random variates on (0,1). The velocity components are as follows, where V_{mag} is the magnitude of the velocity of the particle.

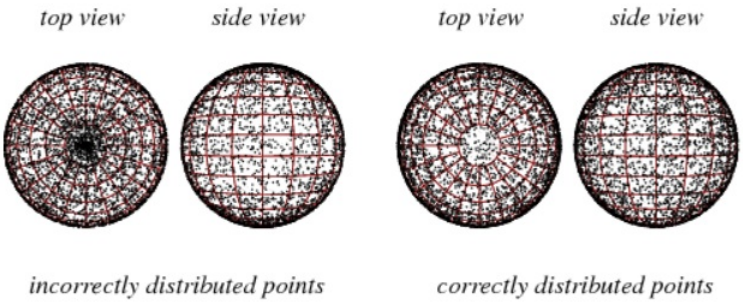

Figure 4.3: Figure shows incorrect way (left) and correct way (right) to model points on a sphere [http://mathworld.wolfram.com/spherepointpicking]

$$\phi = 2\pi u \tag{4.2}$$

$$\alpha = \cos^{-1}(2v - 1) \tag{4.3}$$

$$V_x = V_{mag} \cos\alpha \tag{4.4}$$

$$V_y = V_{mag} \sin\alpha \cos\phi \tag{4.5}$$

$$V_z = V_{mag} \sin\alpha \sin\phi \tag{4.6}$$

4.5 Results of injected ion case

4.5.1 Backstreaming ions run table

We carry out a sequence of simulations to explore the parameter dependence of the beam-pulse interaction. The runs for the injected ion case are shown in table 4.1. They are carried out with release position 80-85 (except E20) and all runs have pulse width $l = 10$. All runs are for a positive winding number $n = +2$ except E2 ($n = -2$). The injected velocity $v_{\rm inj}$ and the shell velocity $v_{\rm shell}$ are chosen as for nominal $M_A = 5$ shock with θ_{Bn} as 30 degrees except for runs E3 and E4. We confirmed that the initial conditions produced a propagating pulse with minimal transients, with right-hand spatial polarization for positive winding number n=+2. Since B is predominantly in the x direction and the ions travel towards negative x, they see the pulse as left-hand polarized. For negative winding number (e.g., n=-2) they see the pulse as right-hand polarized.

4.5.2 Reference case: run E1

In figure 4.4 we show an overview of the interaction for a case which can act as a reference for later runs. We show the time evolution of the magnetic field and its components and the number density of the energetic injected particles. In addition we show profiles of the magnetic field and components at timesteps 400 and 1000. There is a narrow feature that develops at simulation units $T = 4$ (in units of Ω_{cp}^{-1}) and this has a magnetic field amplitude of about 2. It develops at about the same time that the ions are reflected off from the pulse. This narrow feature weakens as it propagates and does not last long. The pulse splits into two parts, there is left ward and a right ward propagating waves launched at this time. The left ward propagating

Table 4.1: Backstreaming ion run table

Run	θ_{Bn}	$v_{\rm inj}$	$v_{\rm shell}$	pitch angle	gyrophase	b	n_{inj}	comment
E1	30	-6.0	5.9-6.1	110-180	0-360	1	0.1	
E2	30	-6.0	5.9-6.1	110-180	0-360	1	0.1	$n = -2$
E3	0	-5.0	4.9-5.1	110-180	0-360	1	0.1	
E4	0	-5.0	4.9-5.1	110-180	0-360	1	0.2	
E5	30	-6.0	5.9-6.1	110-180	0-360	2	0.1	
E6	30	-6.0	5.9-6.1	110-180	0-360	3	0.1	
E7	30	-6.0	5.9-6.1	110-180	0-360	4	0.1	
E8	30	-6.0	5.9-6.1	110-180	0-360	1	0.01	
E9	30	-6.0	5.9-6.1	110-180	0-360	2	0.01	
E10	30	-6.0	5.9-6.1	110-180	0-360	3	0.01	
E11	30	-6.0	5.9-6.1	110-180	0-360	4	0.01	
E12	30	-6.0	5.9-6.1	110-180	0-360	1	0.05	
E13	30	-6.0	5.9-6.1	110-180	0-360	1	0.2	
E14	30	-6.0	5.9-6.1	110-180	0-360	1	0.4	
E15	30	-6.0	5.9-6.1	110-180	0-360	1	0.6	
E16	30	-6.0	5.9-6.1	110-130	0-360	1	0.2	
E17	30	-6.0	5.9-6.1	150-180	0-360	1	0.2	
E18	30	-6.0	5.9-6.1	110-130	0-90	1	0.1	
E19	30	-6.0	5.9-6.1	110-130	180-270	1	0.1	
E20	30	-6.0	5.9-6.1	110-180	0-360	1	0.1	$x_{\rm inj} = 65 - 85$

wave develops a dispersive wavetrain and the components can be seen in the plots at $T = 10$. Most of the injected ions do eventually pass through the pulse, although some get trapped between the edges of the split pulse.

4.5.3 Cyclotron interaction: run E2

Run E2 is carried out with pulse winding number $n = -2$, that is a twist in the opposite sense. The protons move in a Left-handed sense round the magnetic field and the pulse with negative winding number has a Left-handed sense in space. However, the pulse is moving in time so the ions "see" the pulse in a Right-handed sense in time, thus there is minimal interaction and the pulse is almost unchanged. In the case where the pulse winding number is positive, it is Right-handed in space, but the protons "see" it in a Left-handed sense. Therefore there is strong coupling and energy transfer between the pulse and the ions. Consequently, we see an effective interaction between injected ions and the pulse in the case E1, but hardly any interaction in case E2. This can be seen by comparing figures 4.4 and 4.5. The interaction is dominated by cyclotron effects as the pulse is almost unchanged with very little interaction with negative winding number. For the rest of this chapter we use $n = +2$ corresponding to the strong cyclotron coupling situation.

4.5.4 Shock angle

We concentrate on shock angle of $\theta_{Bn} = 30$ degrees, as that is representative of quasi-parallel shock transition. However, here we compare the effects with a parallel shock by looking at run E3 ($\theta_{Bn} = 0, n_{inj} = 0.1$) and run E4 ($\theta_{Bn} = 0, n_{inj} = 0.2$). The results of these runs are shown in figures 4.6 and 4.7. We find that as in the reference case run E1 described earlier (figure 4.4), run E3 also gives a narrow peak at $T = 4$

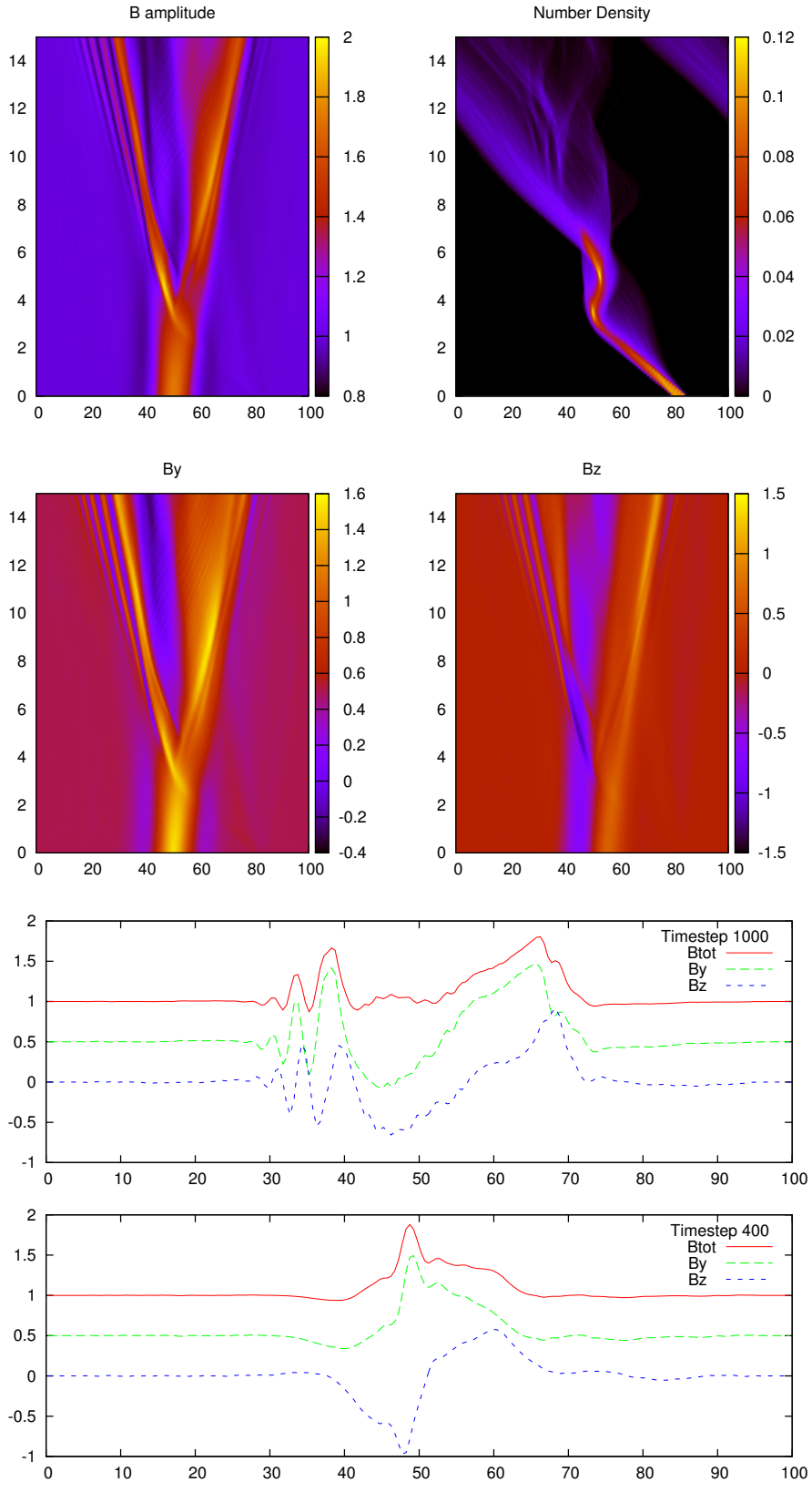

Figure 4.4: Run E1 summary where the top four panels show the time evolution of the magnetic field and the number density of the particles. The vertical axis is the timestep and the horizontal axis is the x position. The bottom two panels show the magnetic field components as a function of x, for fixed timesteps.

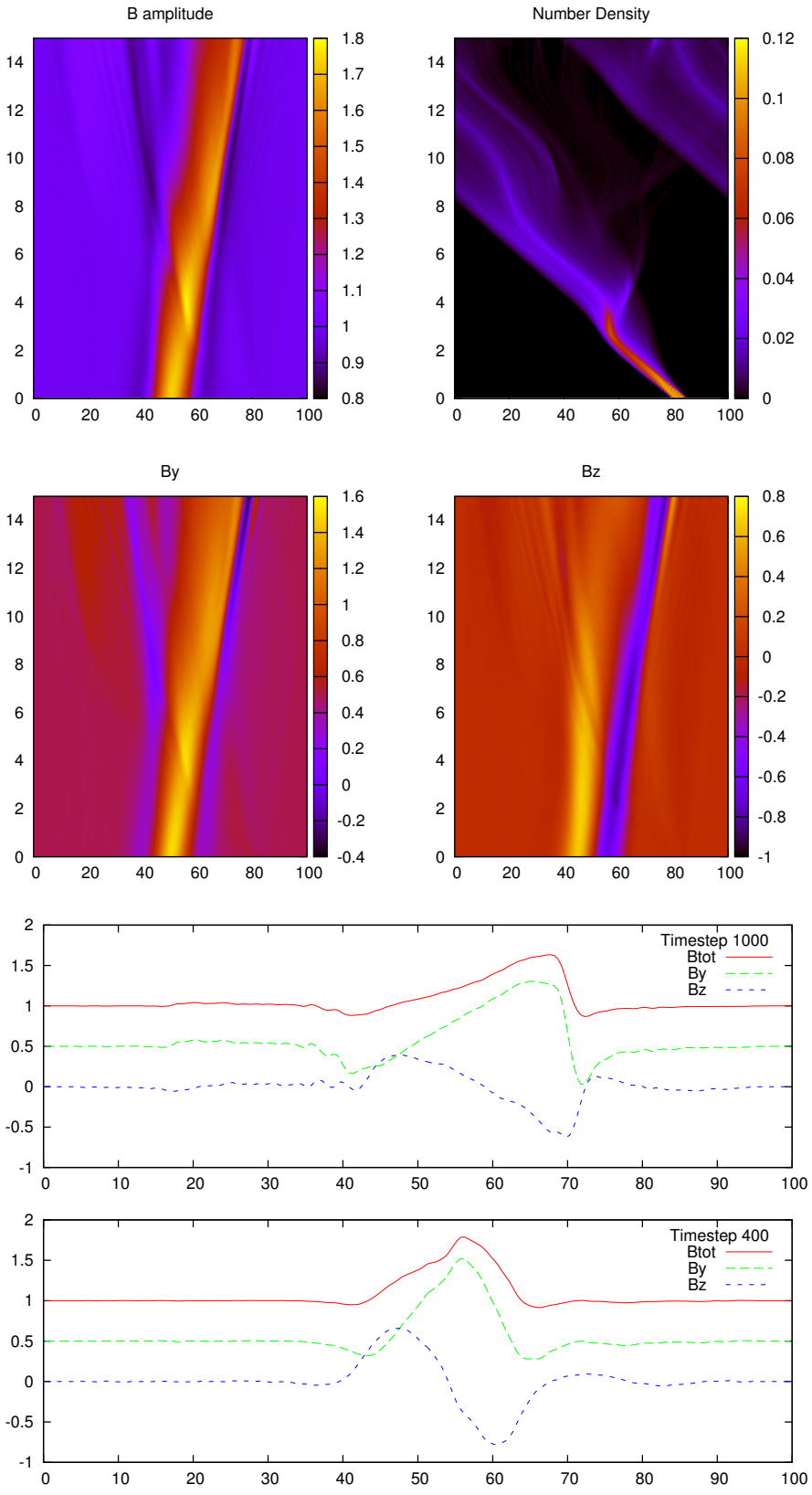

Figure 4.5: Run E2 summary: axes as in figure 4.4.

and then it fades. It launches a leftward wave as the pulse splits, but now the left wave is dispersion dominated. The backstreaming ions are mostly inside the split pulse. In run E4, where we use a higher injected ion density, the interaction is similar but stronger. Almost all the backstreaming ions are within the split pulse. The ions are trapped in the pulse for longer in the parallel shock case than in quasi-parallel ($\theta_{Bn} = 30$) shock case.

4.5.5 Effect of increasing size of initial pulse

We look at runs with different initial pulse amplitudes, namely E8 ($b = 1$), E9 ($b = 2$), E10 ($b = 3$), E11 ($b = 4$), shown in figure 4.8. These runs are with low density of injected ions, that is $n_{inj} = 0.01$, similar to just test particle case where the particle does not contribute to plasma density and current. The aim is to have just the effect of increasing the pulse size with little self-consistent effects. The runs show that as the pulse gets bigger there is an increase in reflection of the backstreaming ions. Reflection occurs for runs with $b = 3$ and $b = 4$. Ions which do end up transmitted spend longer in the pulse. As pulse size increases, there are more turnaround peaks in the backstreaming ion density.

Runs are also carried out for increasing pulse size, but with higher injected ion density, that is $n_{inj} = 0.1$. These runs are E1 ($b = 1$), E5 ($b = 2$), E6 ($b = 3$), E7 ($b = 4$), shown in figure 4.9. In this case we can see the effects of the self-consistent interaction since the backstreaming density is higher. The interaction causes some splitting of the pulse, which is most evident for run E1 ($b = 1$) and E5 ($b = 2$). The backstreaming ions have little effect on the largest pulse, that is in E7 ($b = 4$), but do cause some internal structure of the pulse. As the pulse size increases, ions spend a longer time being trapped within the pulse.

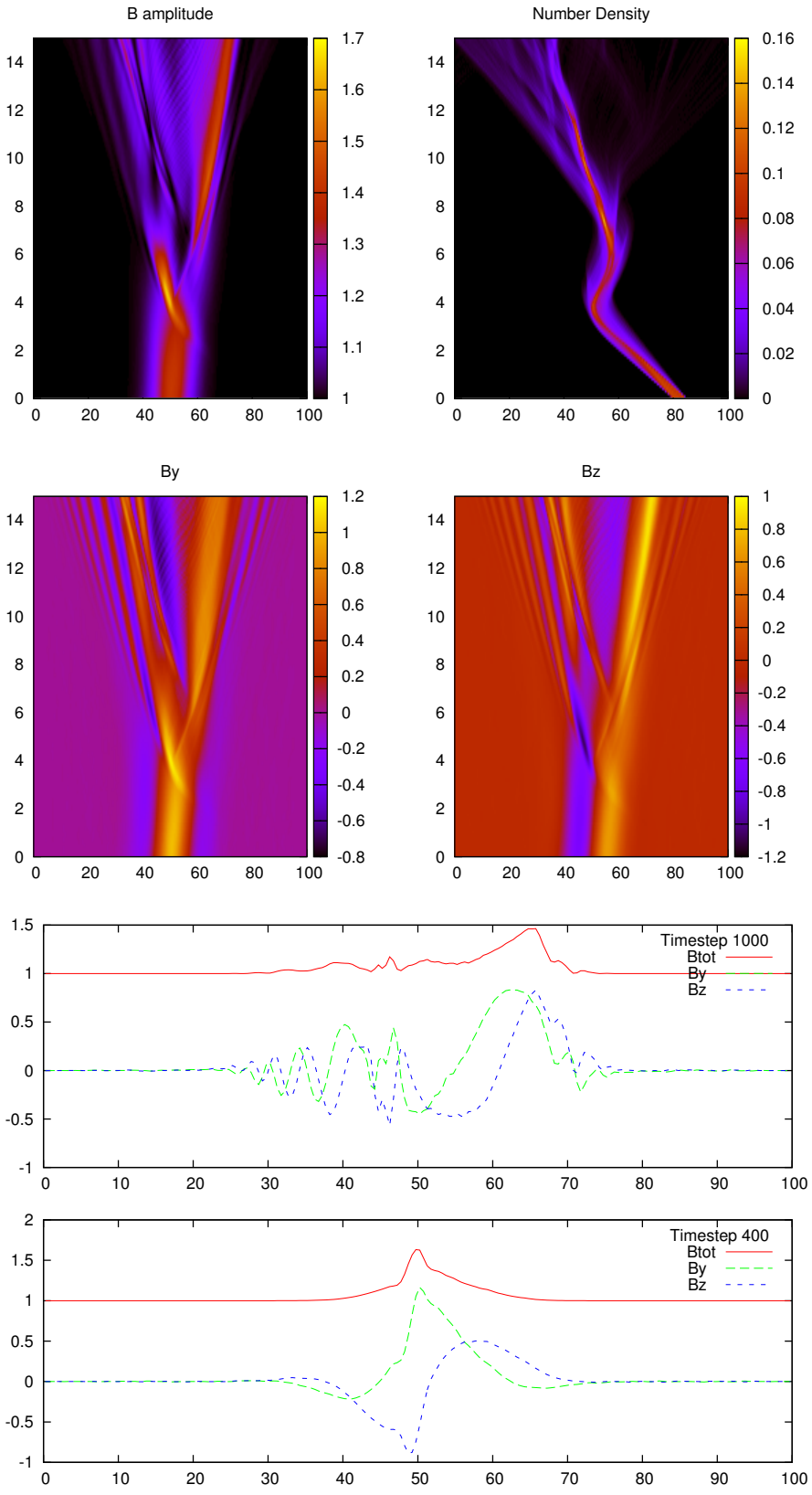

Figure 4.6: Run E3 summary: axes as in figure 4.4.

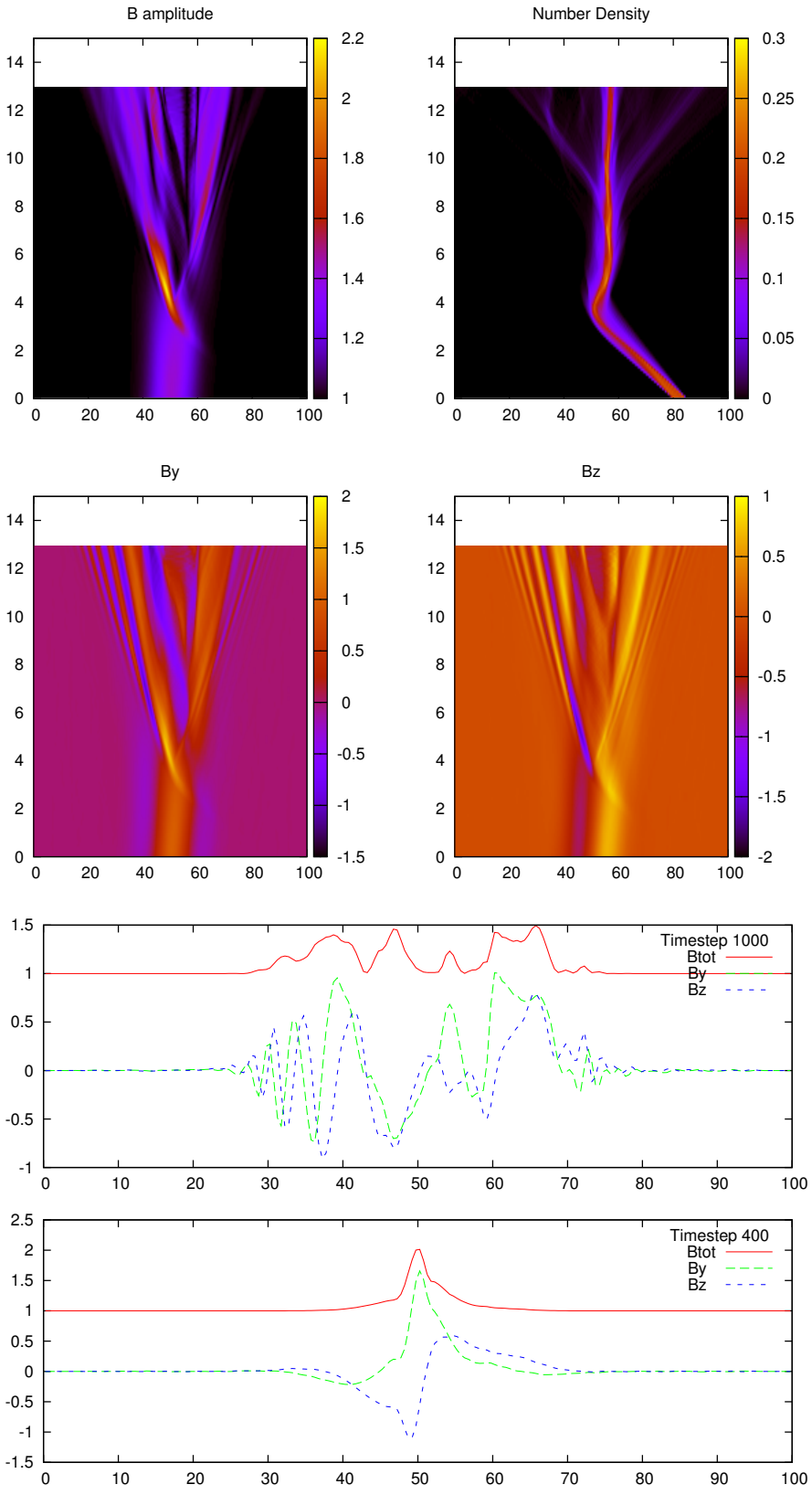

Figure 4.7: Run E4 summary: axes as in figure 4.4.

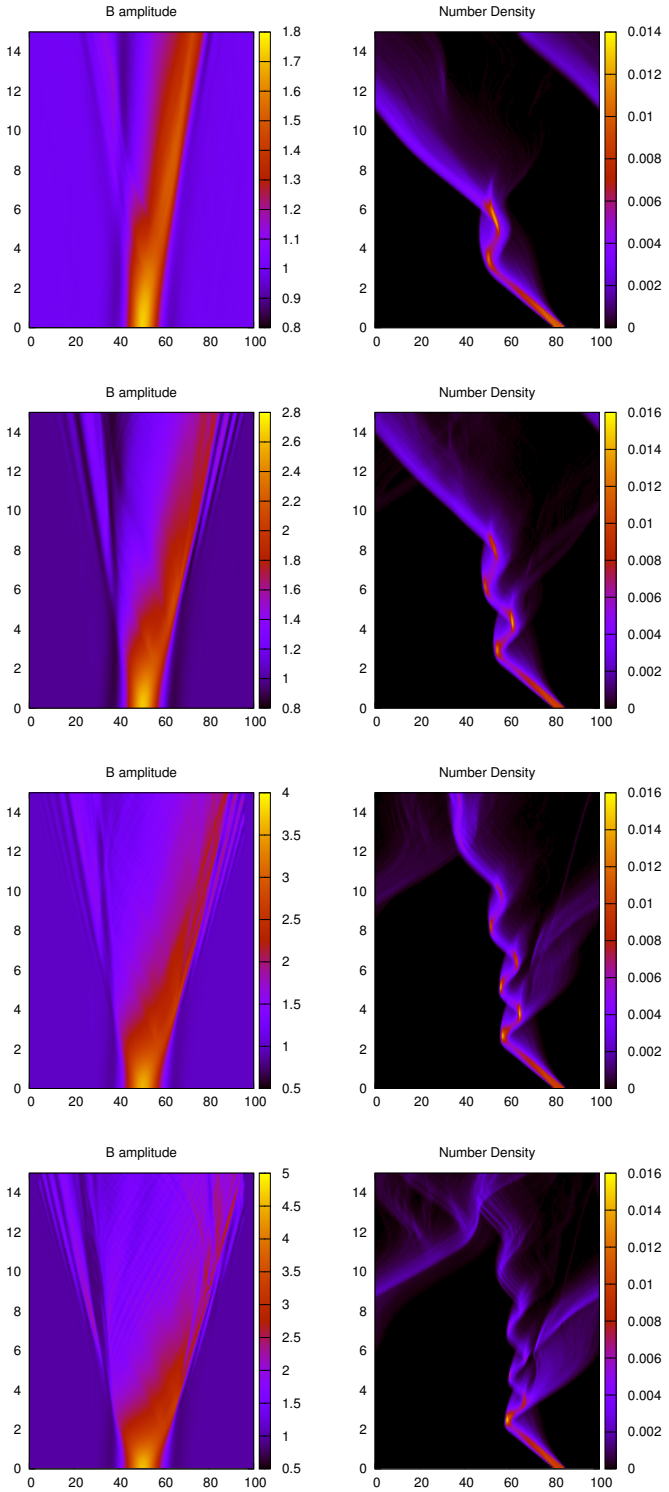

Figure 4.8: E8, E9, E10, E11 from top to bottom- increasing pulse size $n_{inj} = 0.01$: axes as in figure 4.4.

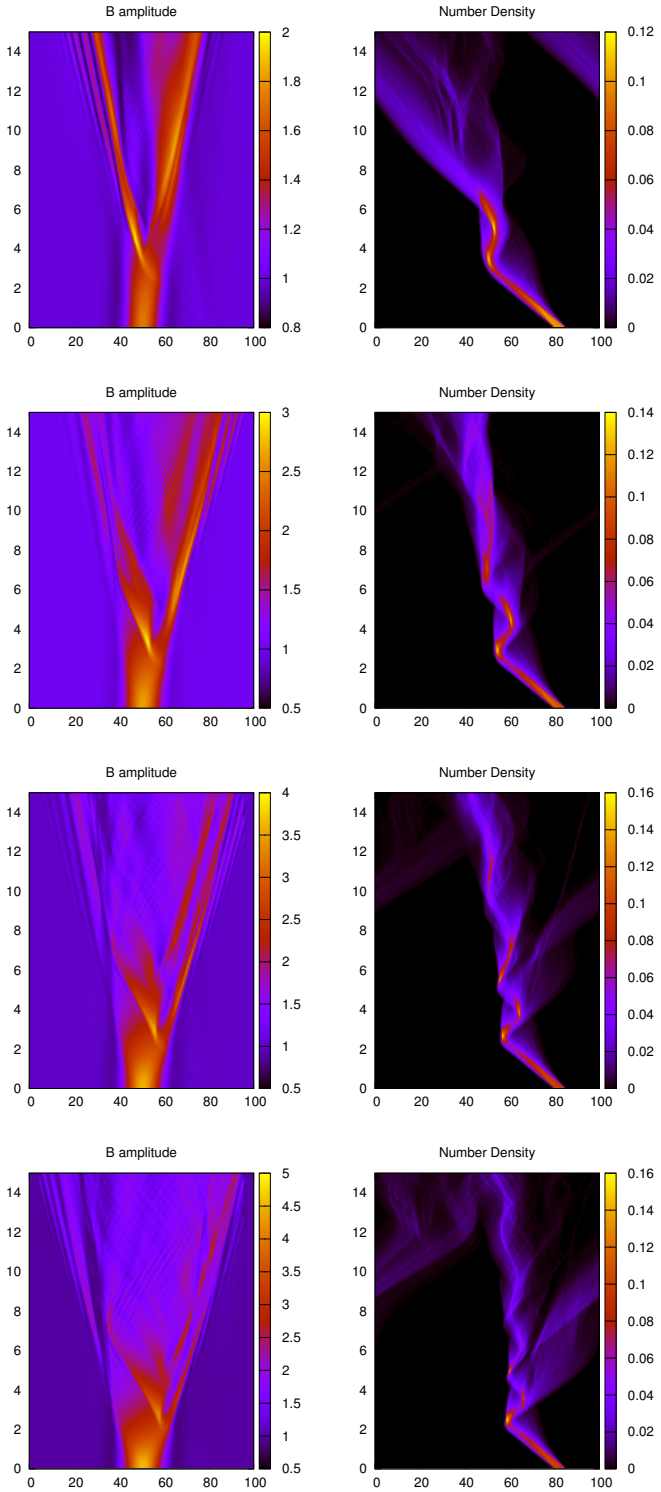

Figure 4.9: E1, E5, E6, E7 from top to bottom - increasing pulse size $n_{inj} = 0.1$: axes as in figure 4.4.

4.5.6 Increasing injection density for $b = 1$

Runs are carried out for different injection densities and these are E12 ($n_{inj} = 0.05$), E13 ($n_{inj} = 0.2$), E14 ($n_{inj} = 0.4$), E15 ($n_{inj} = 0.6$), shown in figure 4.10. As the density increases, the narrow interaction feature gets increasingly larger in amplitude, but remains narrow. For ($n_{inj} = 0.6$), it reaches 5.5 at $T = 4$. A leftward wave is launched, which weakens but remains relatively high. This leftward wave travels faster as n_{inj} increases. The number of backstreaming ions that are transmitted through the pulse are reduced as n_{inj} increases. More detailed results of run E15 are shown in figure 4.11.

4.5.7 Pitch angle ranges within backstreaming ions

We have also examined runs using a broad range of pitch angles of backstreaming ions. Now, we specifically look at gyrating and field aligned ions by controlling the pitch angle range. We keep the density at ($n_{inj} = 0.2$) for all these runs. So run E13 has full range of pitch angles for backstreaming ions, that is 110 - 180 degrees, run E16 has pitch angle range 110 - 130 degrees, that is, gyrating ions (but gyrotropic) and run E17 has pitch angle range 150 - 180 degrees, that is, field aligned ions. Figure 4.12 shows the results of these runs. The strongest narrow peak is seen in the case of the field aligned ions. The field aligned ions decelerate and couple to the background plasma. Gyrating ions produce a broader peak rather then the strong narrow peak from field aligned ions. All cases show pulse splitting and produce leftward propagating wave.

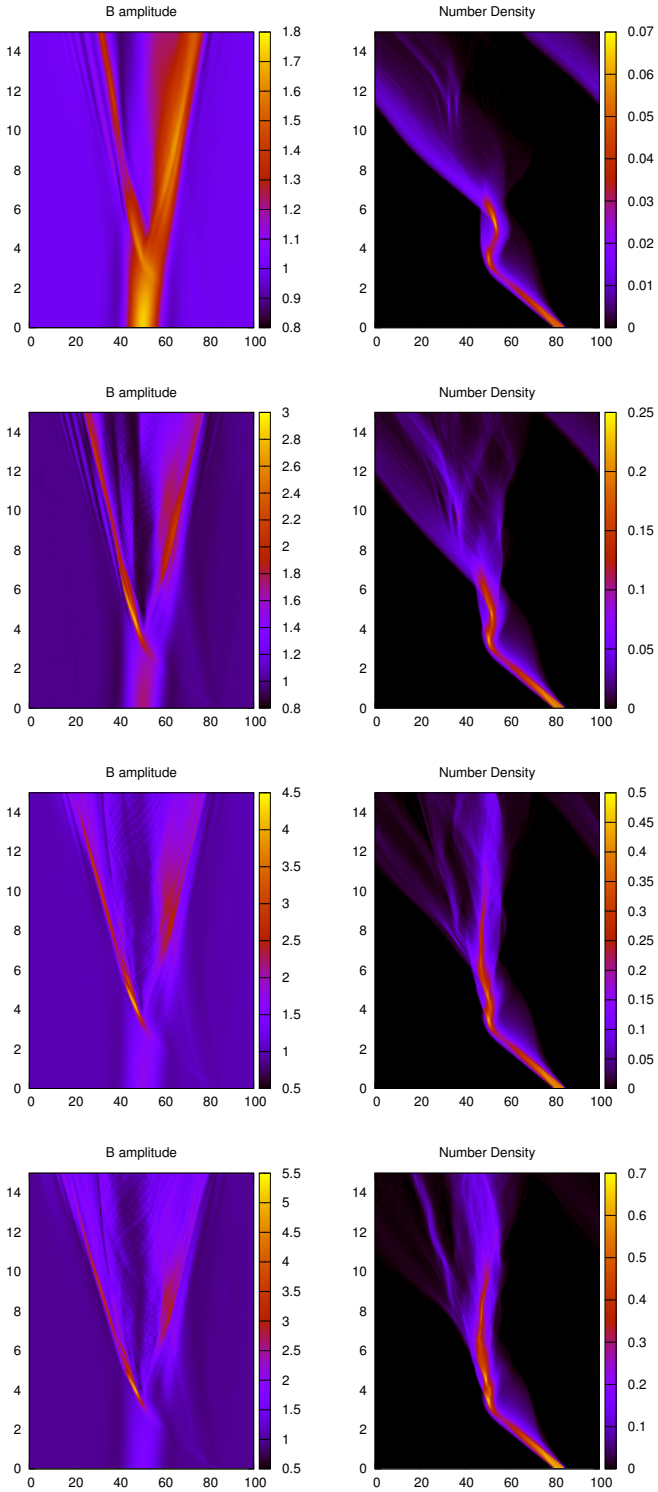

Figure 4.10: E12, E13, E14, E15 from top to bottom - increasing backstreaming ion density: axes as in figure 4.4.

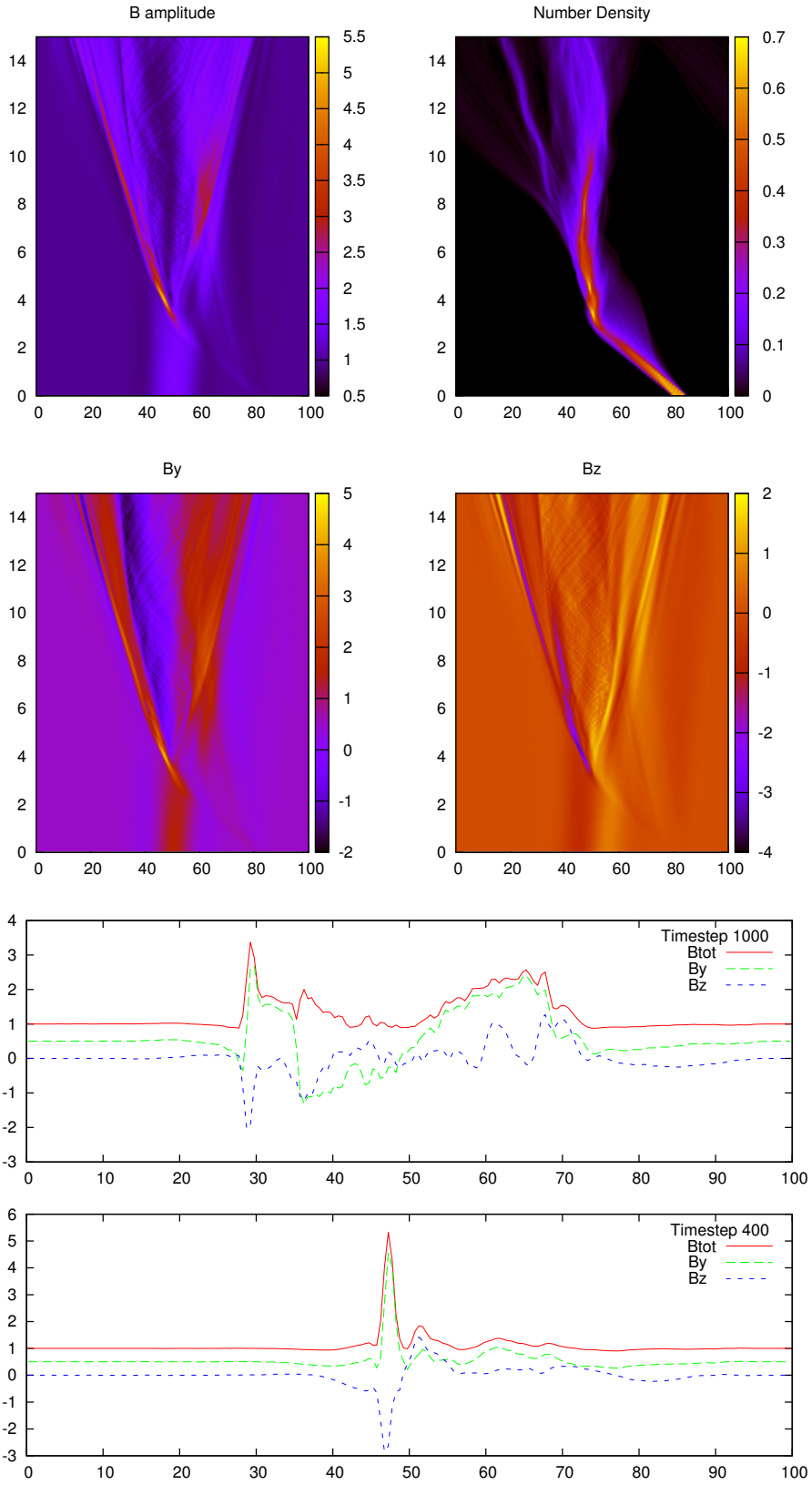

Figure 4.11: Run E15 summary: axes as in figure 4.4.

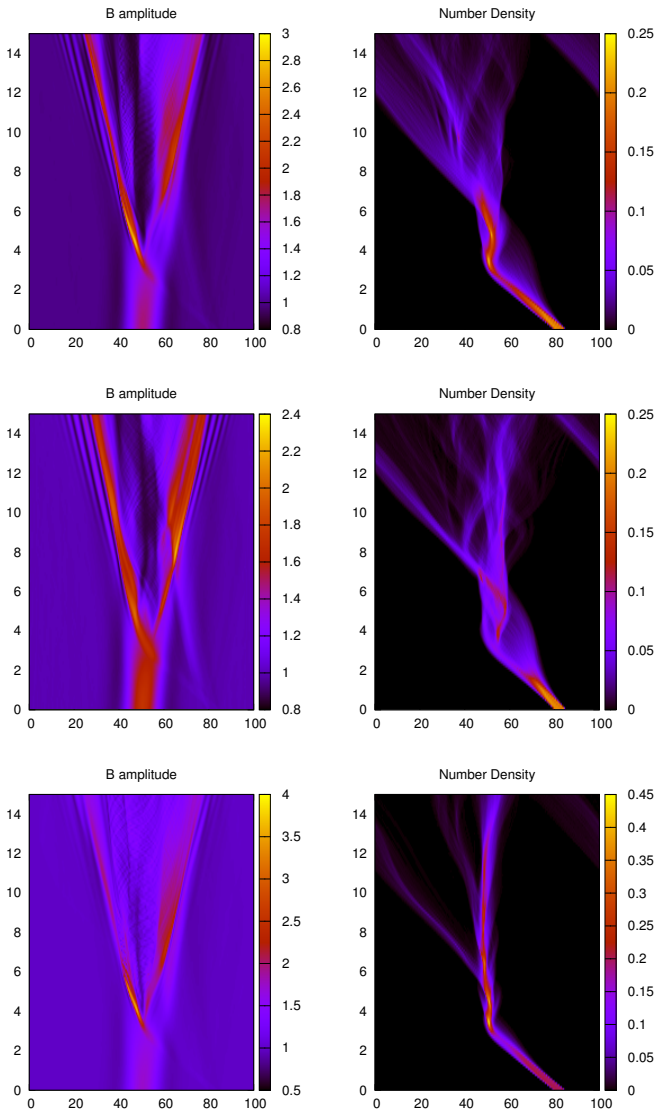

Figure 4.12: E13 (full pitch angle range), E16 gyrating, E17 field aligned: axes as in figure 4.4.

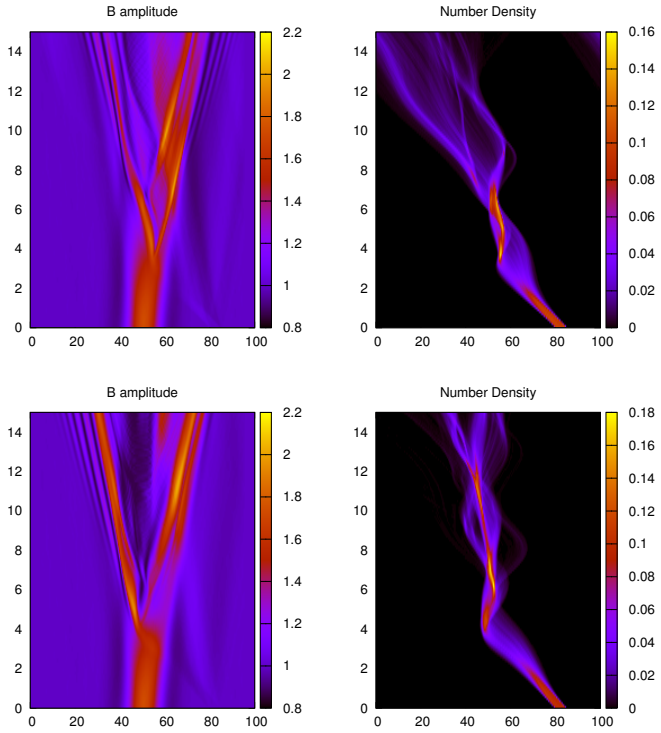

Figure 4.13: Gyrating: Non-gyrotropic E18 gyrophase angle 0-90, E19 gyrophase angle 180-270: axes as in figure 4.4.

4.5.8 Non-gyrotropic gyrating

In this case the runs are for ions that are non-gyrotropic, that is, non-uniform in gyrophase angle. Run E18 is for ions with pitch angle 110 - 130 degrees and gyrophase angle 0 - 90 degrees. Run E19 is for ions with pitch angle 110 - 130 degrees and gyrophase angle 180 - 270 degrees. The results of runs E18 and E19 are shown in figure 4.13. Results are not very different to those of run E16, which is for gyrotropic gyrating ions. Run E19 shows that the gyrating ions with that gyrophase angle range get trapped within the split pulse rather than getting transmitted like the ions of run E18.

4.5.9 Large injection zone

Finally for E20, the injection zone is very large, 65-85, while the injection density is $n_{inj} = 0.1$. This can be seen in figure 4.14. There is very fast wave growth with larger injection zone and the magnitic field magnitude peak reaches 4.0. There is a fast leftward wave travelling at about $2.7V_A$. The backstreaming density increases to 0.3. We note that at timestep 400 the leftward travelling wave has a monolithic appearance with little structure, but with a steep upstream edge that develops into what looks like a low Mach number shock. There are several similarities with the properties of observed SLAMS.

4.6 Results of Diffuse ions case

4.6.1 Diffuse ions run table

The diffuse ion run table 4.2 shows the runs for different parameters used. All runs have pulse width $l = 10$ and are for a positive winding number $n = +2$.

4.6.2 Reference case: run D1

Run D1 (shown in figure 4.15) is for diffuse ions with $n_{inj} = 0.1$ and a pulse of $b = 1, n = +2$. The shock angle is taken to be 30 degrees as in the backstreaming ion case. This run is for case where there is no $v_{\|}$ drift in the diffuse ions. There is no sign of a narrow structure as seen in the backstreaming ion case. In this case there is some evidence of a leftward propagating wave that develops at about $T = 10$. There is little effect on the density of the diffuse ions.

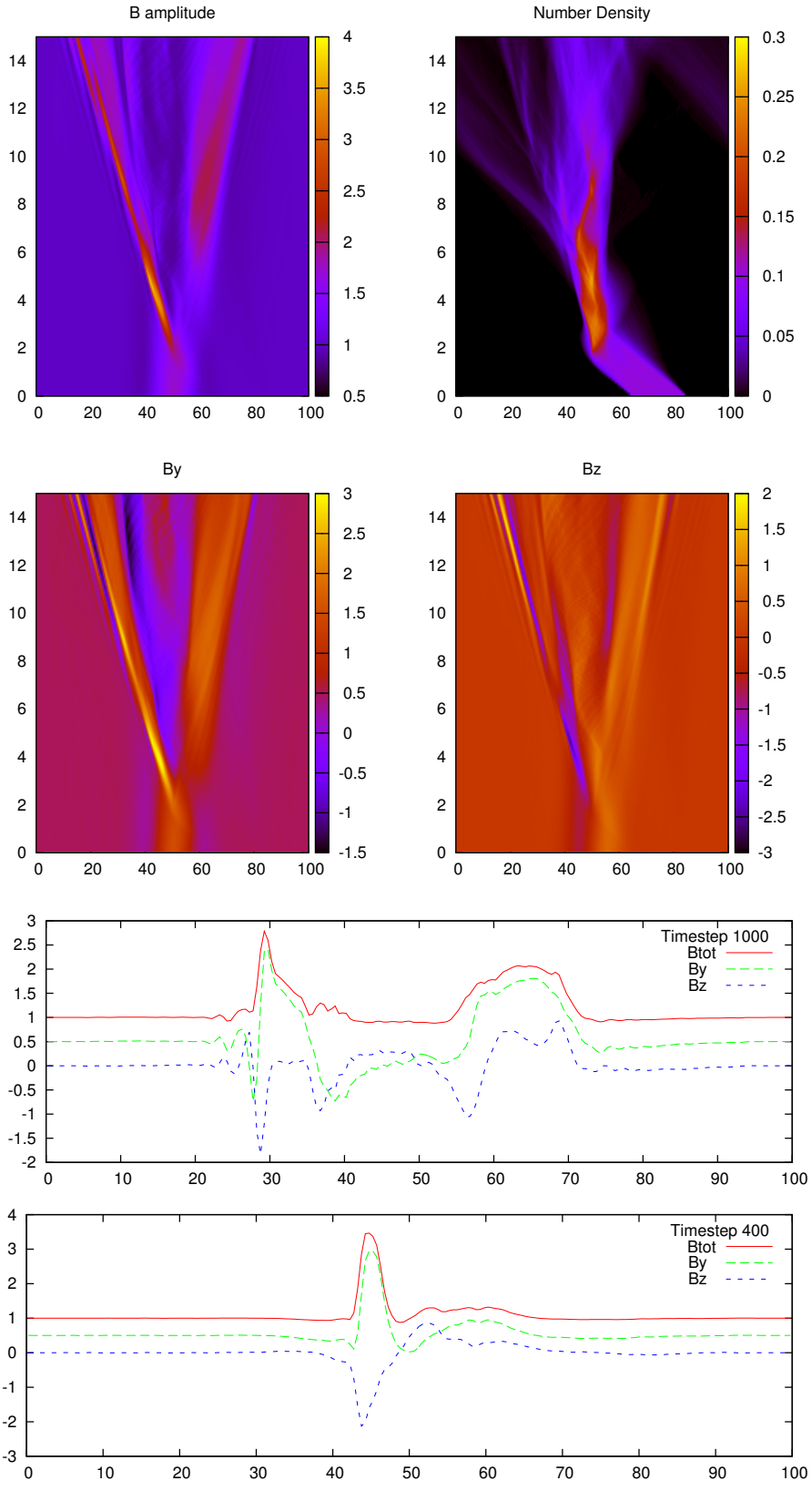

Figure 4.14: E20 - large injection zone summary: axes as in figure 4.4.

Table 4.2: Diffuse ion run table

Run	θ_{Bn}	$v_{\parallel}$	n_{inj}	v_{shell}	b
D1	30	0.0	0.1	25-30	1
D2	30	-2.5	0.1	25-30	1
D3	30	-2.5	0.2	25-30	1
D4	30	-1.0	0.2	25-30	1
D5	0	0.0	0.2	25-30	1
D6	0	-2.5	0.2	25-30	1
D7	30	0.0	0.2	25-30	2
D8	30	-2.5	0.1	25-30	2
D9	30	-2.5	0.05	25-30	1
D10	30	-2.5	0.01	25-30	1
D11	30	-2.5	0.1	25-30	4
D12	30	-2.5	0.01	25-30	4

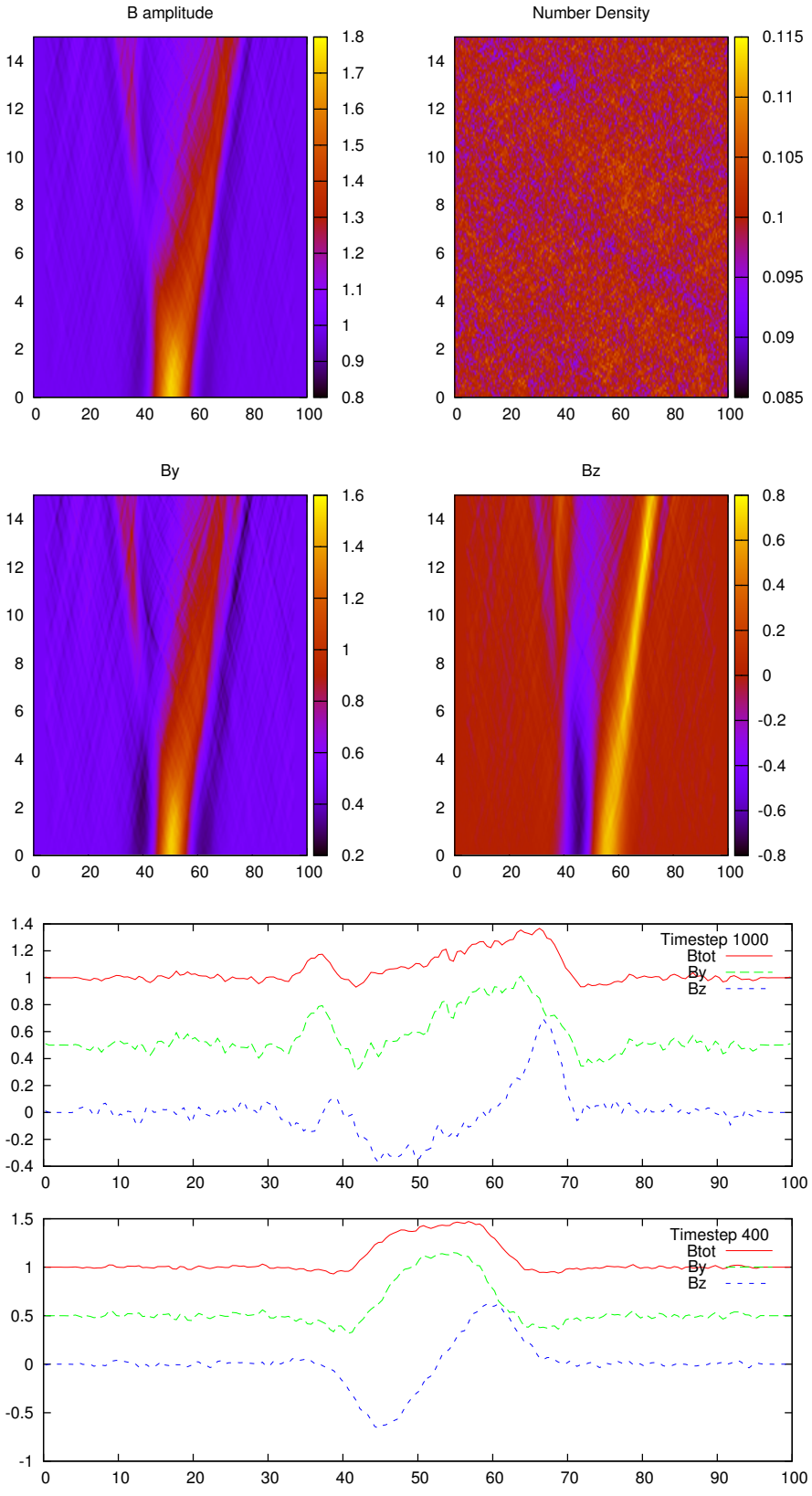

Figure 4.15: Run D1 summary: axes as in figure 4.4.

4.6.3 Effect of $v_{\|}$ drift: run D2

Close to the shock transition, diffuse ions are sometimes seen with a small upstream directed velocity shift relative to the plasma frame, so we add the effect of a shift in velocity, that is $v_{\|} = -2.5$. This may be a little high, but it used to show the effects clearly. Figure 4.16 shows the results of run D2. The pulse splitting is strongly evident in this with the drift and a leftward propagating wave is launched earlier on than in case without the drift. This is similar to backstreaming ion case.

4.6.4 Effect of increasing size of initial pulse

We look at runs D2 ($b = 1$), D8 ($b = 2$) and D11 ($b = 4$), so that we can see the effect of increasing the initial pulse amplitude. The results can be seen in figure 4.17. It is evident that the pulse size has to be large, that is about $b = 2$, before there is an effect on increasing the background diffuse ion density.

4.6.5 Increasing diffuse ion density for $b = 1$

Runs are carried out for different diffuse ion density. These runs are D10 ($n_{inj} = 0.01$), D9 ($n_{inj} = 0.05$), D2 ($n_{inj} = 0.1$) and D3 ($n_{inj} = 0.2$). The results can be seen in figure 4.18. The leftward propagating wave that is seen at $T = 10$ increases in size with increasing density and is strongest for $n_{inj} = 0.2$.

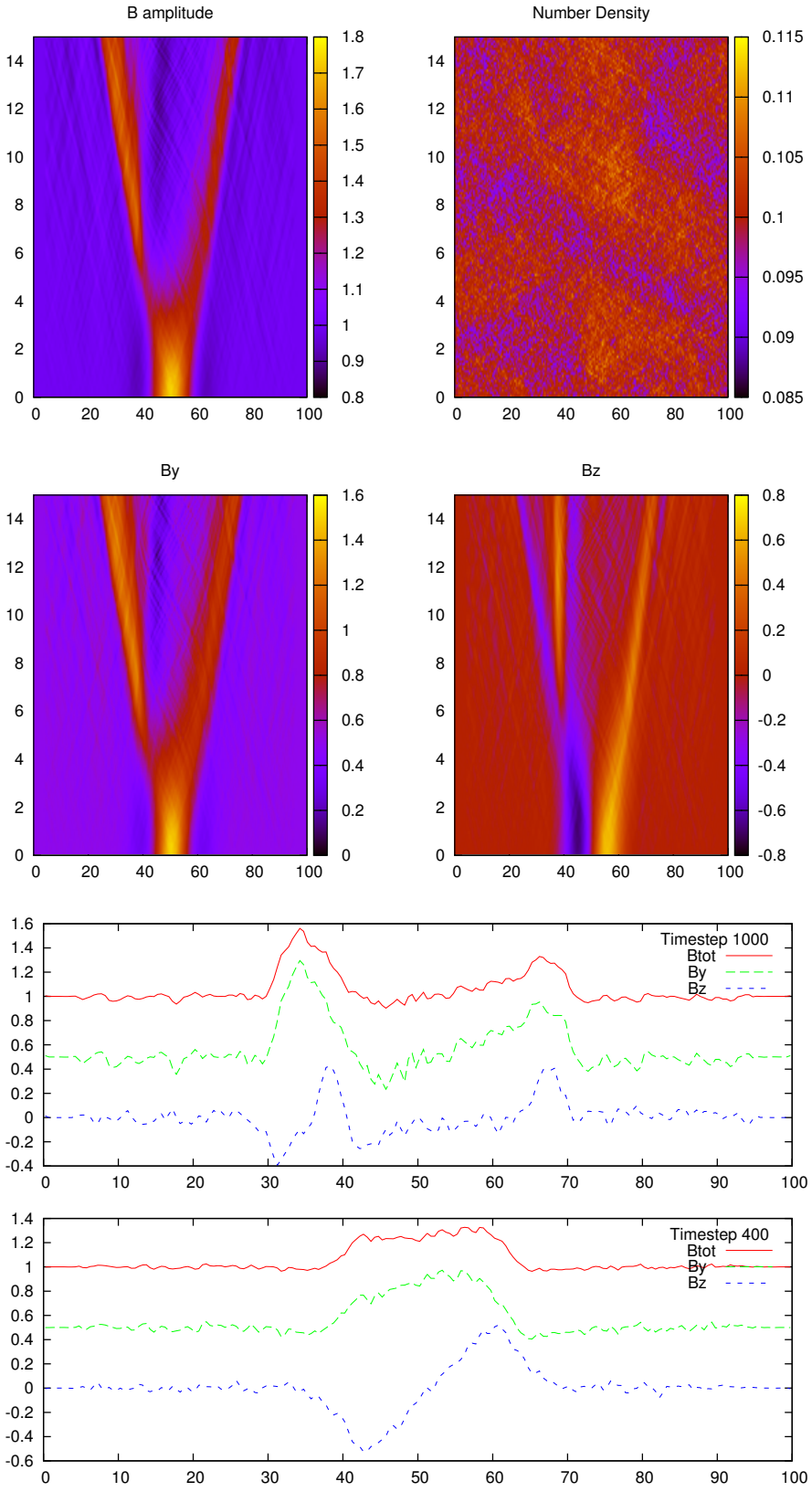

Figure 4.16: Run D2 summary: axes as in figure 4.4.

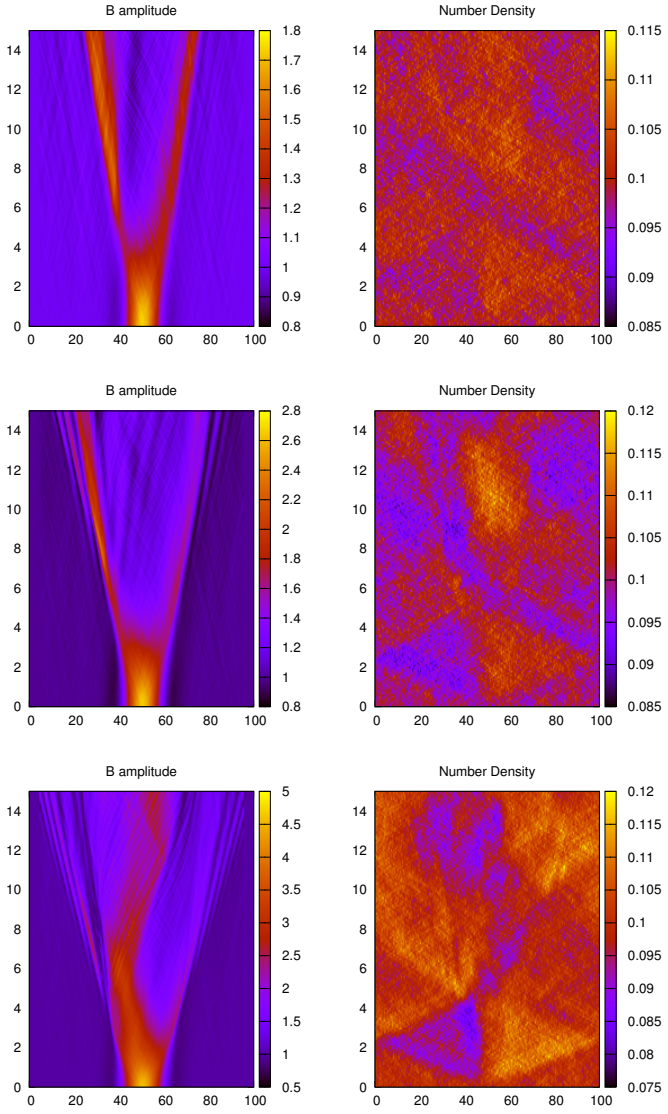

Figure 4.17: Diffuse ions D2,D8 and D11 - increasing pulse size: axes as in figure 4.4.

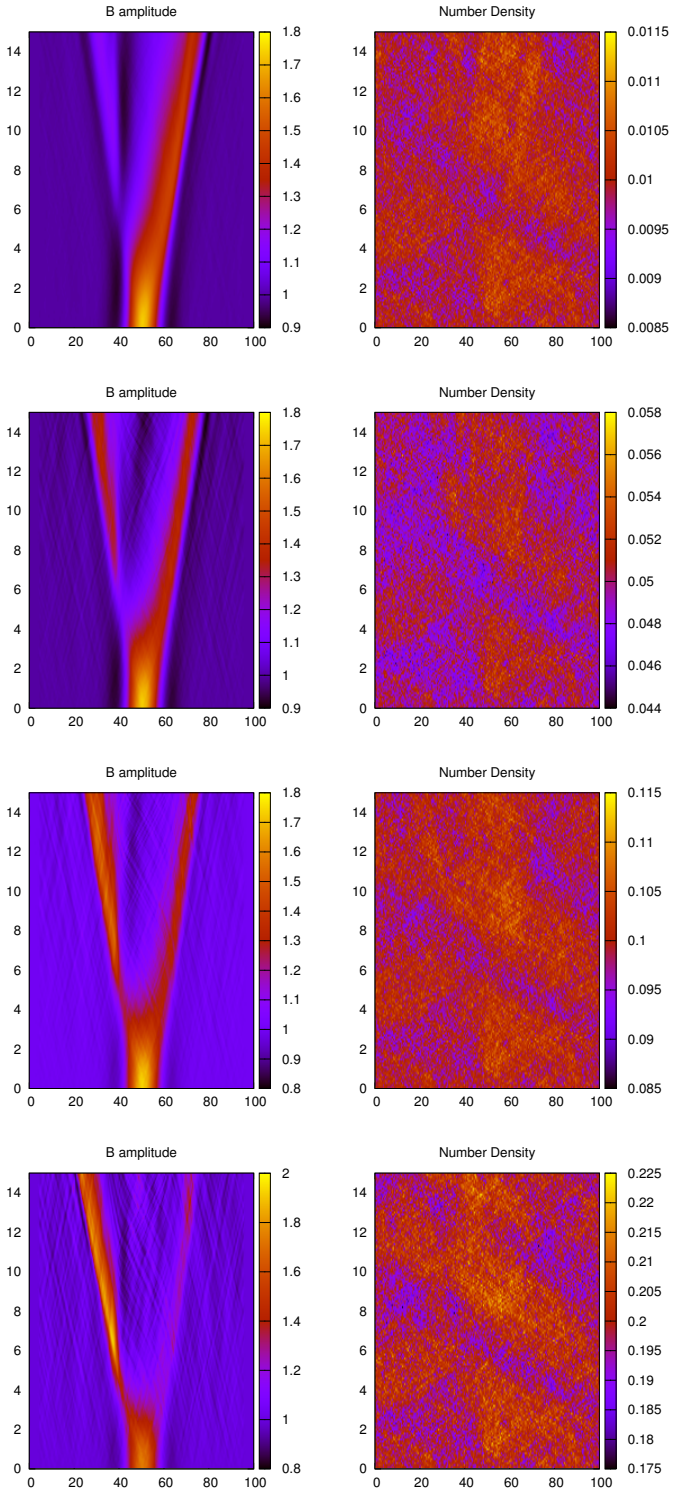

Figure 4.18: Diffuse ions D10, D9, D2 and D3- increasing diffuse ion density: axes as in figure 4.4.

4.6.6 Shock angle

We can look at the effect of a shock angle by comparing run D3 ($\theta_{Bn} = 30$) with run D6 ($\theta_{Bn} = 0$). Run D3 and D6 are shown in figures 4.19 and 4.20 respectively. A stronger leftward propagating wave is launched in run D3 which is the quasi-parallel case, than in run D6, the parallel case. The reason for this might be that the wave is propagating at an oblique angle to the field, and is more compressive, leading to non-linear steepening in the B_y component. There is little effect on the density in both runs D3 and D6.

4.7 Discussion

The mechanism for the interaction between the backstreaming ions and the pulse is described by Scholer and Burgess, 1992. Ions are decelerated and deflected by the pulse, causing a local density enhancement. Since the flow is frozen-in with the flux, the magnetic field increases. This causes a positive feedback loop to develop and background ions get decelerated and deflected by the enhanced magnetic field. We find that there is a local density enhancement during the interaction, which is consistent with the mechanism described by Scholer and Burgess, 1992 and with results of Onsager et al., 1991a.

Our findings in this chapter are consistent with the reflected ion deflection model, but may also highlight some additional features of this mechanism. The interaction causes a very narrow wave to develop. This then splits and launches a leftward propagating wave. Some ions get trapped within the pulse, some do eventually pass through, while in some cases they are reflected by the pulse. As the injection density increases, the number of ions that are transmitted through the pulse reduces. As the pulse size

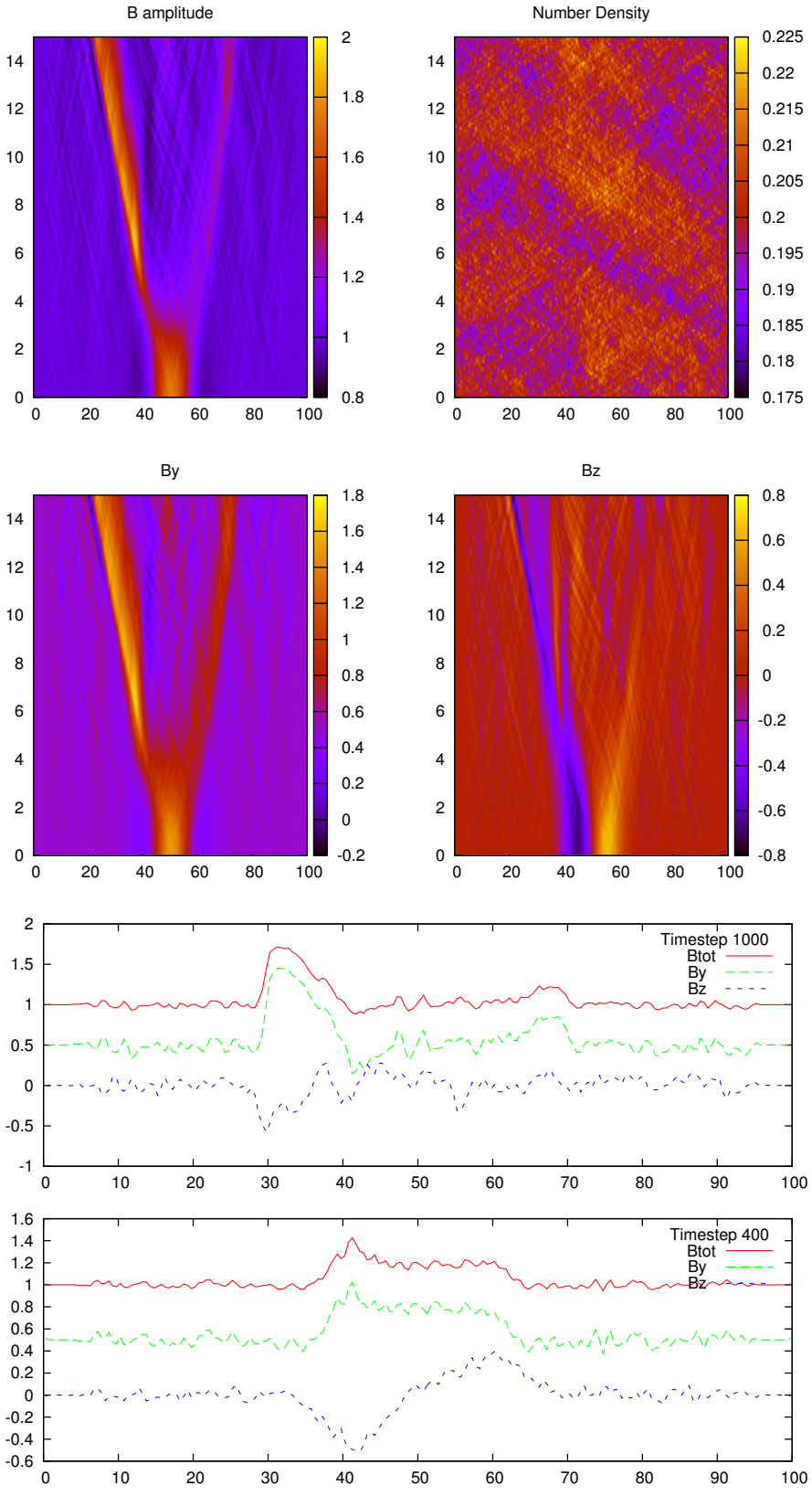

Figure 4.19: Run D3 summary for $\theta_{Bn} = 30°$: axes as in figure 4.4.

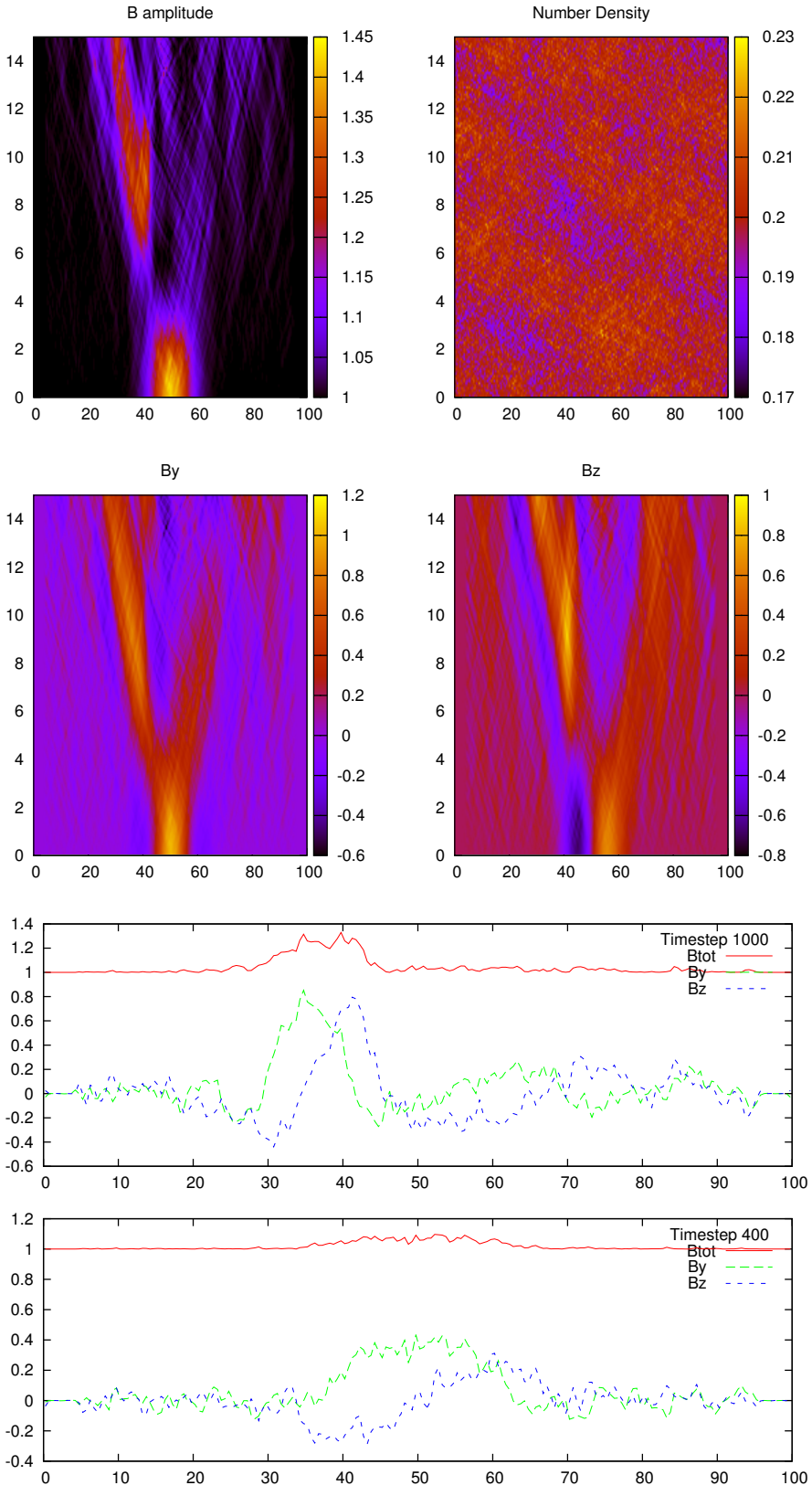

Figure 4.20: Run D6 summary for $\theta_{Bn} = 0°$: axes as in figure 4.4.

increases, the ions spend a longer time being trapped and reflected within the split pulse.

As ion injection density increases, the narrow feature that develops get increasingly larger and the leftward propagating wave that is launched, travels faster. The field aligned ions produce a stronger narrow peak than the gyrating ions. With a very large injection zone, there is very fast growth and amplitude of the magnetic field magnitude reaches 4.0. But a large injection zone might not correspond to the probable injection parameters in a real shock.

In the case of the diffuse ions, there is some growth of the pulse, but no narrow feature forms like in the backstreaming ions case. There is pulse splitting and a leftward propagating wave is launched. When $v_{\|}$ drift is not included, the leftward propagating wave is launched much later than in backstreaming ions case. The initial pulse size has to be large, that is about $b = 2$ before there is an effect of increasing the background diffuse ion density. When the density of the diffuse ions is increased, the leftward propagating wave increases in size. However, any strong interaction requires a diffuse ion density that is probably considerably greater than what is really observed.

The newly launched leftward propagating wave may have some properties of solitons such as larger the wave, the faster it travels and also larger the wave, the narrower it is.

Chapter 5

Analysis of SLAMS events using Cluster observations and simulations

5.1 Overview

In this chapter we describe the work done to determine signatures of different SLAMS events using Cluster observations and compare this with simulation work. We look at events that involve diffuse ions, gyrating ions and field aligned beam ions. For this work, we study Cluster orbit plots and magnetic field data from Cluster Fluxgate Magnetometer (FGM) instrument to identify SLAMS events. Then plots from Cluster Ion Spectrometry (CIS) instrument are used for the analysis of the events. The CIS plots used are ion distribution plots in velocity space. The findings of the analysis are compared with similar ion distribution plots obtained from simulation work.

The chapter starts with an introduction of the Cluster mission and the instruments on

board, with a detailed description of CIS and FGM instruments. We then describe the methodology used to obtain the findings from Cluster data and from simulation work. The results include typical signatures of SLAMS events, which are compared with ion distribution plots from simulation work and the chapter ends with a discussion section.

5.2 Cluster mission

5.2.1 Mission objectives

Earth's Magnetosphere has been explored over many years with in-situ measurements, as it is a region where many interesting phenomena can be seen. The magnetosphere is always changing shape and size often as a result of varied solar wind conditions or through the impact of Coronal Mass Ejections from the Sun. As a result, many of the processes going on inside it may vary in time and space or in both simultaneously. Hence it is a necessity to be able to distinguish between spatial and temporal changes within the magnetosphere.

Many single spacecraft missions have been used to explore this region. However, these type of missions present limitations as they cannot be used to distinguish between spatial and temporal changes of a particular quantity, such as magnetic field, plasma density and temperature. The problem was not solved by using two spacecraft such as ISEE and AMPTE, as this only allows finding out the variations along the line between the spacecraft. With three spacecraft it would be possible to work out the variations in a particular plane, but not in 3-dimensions. However, Cluster is able to solve this problem, as the mission involves a quartet of identical spacecraft. The instruments onboard can take measurements at the same time and different places in space to allow relative temporal and spatial variations of a quantity to be found.

Cluster can analyse many magnetospheric boundaries from multi-point measurements. During the mission, it crosses the dayside Bow shock and the magnetopause many times, so observations of these boundaries can be carried out in great detail. Cluster also spends a significant time exploring the magnetotail in order to investigate the structure and evolution of the plasma sheet during substorms. The observation of the current sheet and its magnetic signatures require high time resolution measurements to be carried out at different places simultaneously and Cluster is able to accomplish this.

5.2.2 Orbits and spacecraft separations

The four Cluster spacecraft (denoted by C1, C2, C3 and C4) were launched on board two Soyuz-Fregat launchers in July and August 2000. The spacecraft are in nearly identical and highly eccentric orbits, with an apogee of 19.6 R_E and a perigee of 4 R_E and a time period of 57 hours. In February or mid-winter, Cluster moves over the Northern Polar Cap, crosses the magnetopause and the Bow shock and then moves over the Southern Polar Cap towards the perigee. In August or mid-summer, it follows a path that crosses the magnetotail. These two orbits are shown in figure 5.1.

The orbits are planned in a way that the four spacecraft are located at the vertices of a tetrahedron when any major boundary is being crossed, thus enabling a proper analysis of the boundaries. The separation distances between the spacecraft change between 100 km and tens of thousands of km during the mission, as can be seen in figure 5.2. This allows the study of the phenomena over different scales. In orbit the spacecraft spin axis will have approximately 90 degrees angle with the Sun, which will enable us to get the optimum performance from their solar power generators and thermal-control subsystems.

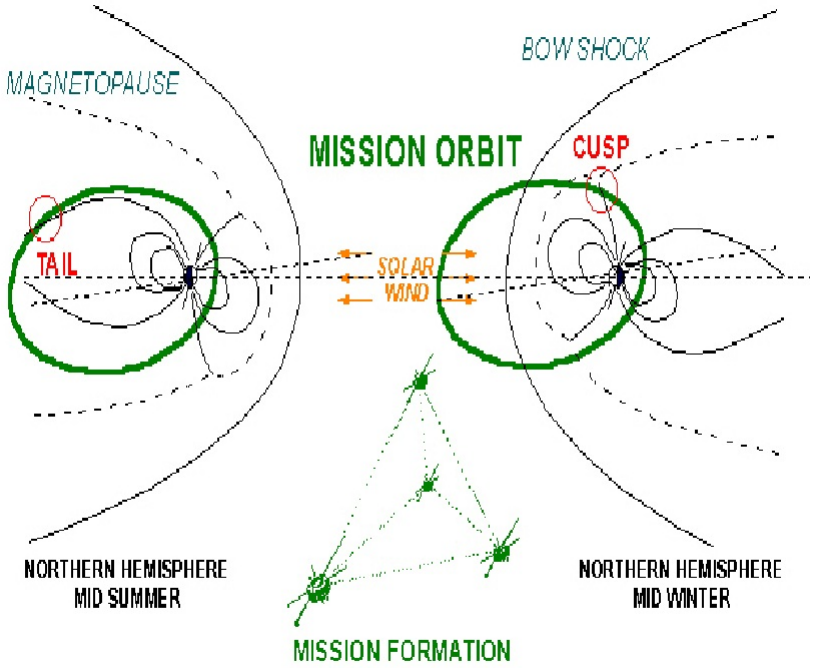

Figure 5.1: Cluster orbits for mid-summer (left) and mid-winter (right) [http://www.esa.int/esapub/bulletin/bullet84/images/credl842.gif]

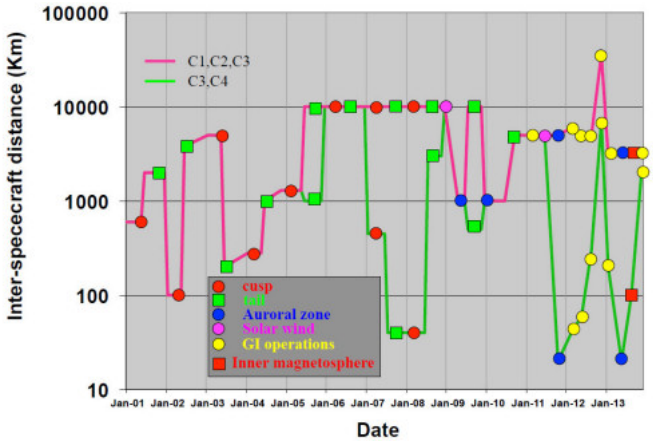

Figure 5.2: Spacecraft separation distances planned for each year of the mission [http://sci.esa.int/cluster/23160-constellation-geometry-over-time]

5.2.3 Cluster instruments

In order to carry out the scientific studies, the four spacecraft each carry a set of 11 identical instruments that measure electromagnetic fields and particle populations over a range of frequencies and energies. The Cluster instruments are described below [Space Science Reviews 1997, Volume 79, Issue 1-2:
http://link.springer.com/journal/11214/79/1/page/1].

1) Fluxgate Magnetometer (FGM) measures the magnetic field vectors. It has two tri-axial fluxgate sensors and an electronics box, which contains the instrument power and sensor electronics controlled by the Data Processing Unit. The sensors are mounted on tip of a 5.0 m radial boom in order to minimise interference from the spacecraft.

2)Spatio-Temporal Analysis of Field Fluctuations experiment (STAFF) looks at the way that magnetic fields change with time. It has a three-axis search coil magnetometer and two data analysis packages: a digital spectrum analyser and a signal processing unit. The spectrum analyser receives signals from the four electric field probes of EFW experiment. The signal processing unit allows observation of three magnetic waveforms.

3)Electric Field and Wave experiment (EFW) observes how the electric field around the spacecraft changes with time. It has four orthogonal cable booms carrying sensors. The potential difference between the two opposite sensors provide the average electric field in two directions.

4)Waves of High frequency and Sounder for probing of electron density by relaxation (WHISPER) measures the density of the hot plasma originating from the sun. A radio wave transmitter sends a wave train at a limited time period at a fixed frequency. This excites natural resonances of the plasma in the frequency range that it covers. A radio receiver is then connected to a dipole electric sensor to determine the signal

around the frequency. The process is repeated at the next frequency step and a series of steps forms a sweep.

5)Wide Band (WBD) makes high time/frequency resolution measurements of the electric field. It processes signals from two antennae of EFW and STAFF search coil magnetometer. The waveforms are digitised and transmitted.

6)Digital Wave Processor (DWP) enables the wave-experiment instruments to be flexible in order to make effective use of the limited spacecraft resources of power. It uses transputers with parallel processing.

7)Electron Drift Instrument (EDI) measures the drift of a beam of test electrons emitted in a certain direction. The drift is related to the electric field and to the gradient in the magnetic field.

8)Active Spacecraft Potential Control Experiment (ASPOC) tries to earth the spacecraft by eliminating excessive positive surface charge by emitting indium ions.

9)Cluster Ion Spectrometry (CIS) analyses the composition and dynamics of particles surrounding the spacecraft, especially slowest moving ions. This is described in some detail in the next subsection.

10)Plasma Electron and Current experiment (PEACE) investigates the distribution, direction and flow and energy distribution of electrons from low to medium energies. It has two sensors with electrostatic energy analysers with positive sensitive microchannel plate detectors.

11)Research with Adaptive Particle Imaging Detectors (RAPID) is a particle detector for the analysis of suprathermal plasma distributions. It uses two different detector systems for detection of electrons and nuclei.

This study uses data from the Fluxgate Magnetometer (FGM) and Cluster Ion Spectrometer (CIS) instruments and hence these are described in some detail here (The Cluster Active Archive by Laakso, Taylor and Escoubet, 2010).

5.2.4 Fluxgate Magnetometer (FGM)

The FGM instrument measures the magnetic field in the vicinity of the spacecraft. It consists of two triaxial fluxgate magnetometers and a Data Processing Unit (DPU). The DPU commands the functions of the FGM. The fluxgate magnetometers function in the following way.

Each fluxgate magnetometer consists of a primary coil, a secondary coil and a ferromagnetic core. If the ambient field is zero, the secondary coil will produce a symmetrical voltage waveform. This waveform has positive pulses (A) and negative pulses (B). If an external magnetic field is then applied, the magnetic flux in the core becomes asymmetric and the phase relation between A and B pulses will shift. A voltage is applied to the secondary coil as part of a feedback circuit to cancel out the phase difference between the A and B pulses. This method ensures that the instrument operates in the regime where the response is most linear.

The fluxgate magnetometers onboard Cluster can function in five ranges, which provide good resolution in the solar wind and in the Magnetosphere. In the solar wind, the field magnitudes can range from 3 nT to 30 nT and in the Magnetosphere it can be as high as 1000 nT. The selection of the range is carried out by the DPU, according to the region that the spacecraft is in. If a magnetic field component is greater than a set fraction of a particular range, an up-range command is sent to the magnetometer.

In order to ensure that the background magnetic noise does not affect the data, one of the sensors or coils is located at the end of a 5.1 m boom and the other coil is at 1.5 m

from the end of the boom. Any of the sensors can be the Primary sensor, as instructed by a command from the ground. The inter-calibration of the magnetometers on the four spacecraft is fundamental as the analysis of FGM data is based on the differences between the four spacecraft. Therefore the error analysis and calibrations are carried out routinely.

5.2.5 Cluster Ion Spectrometer (CIS)

CIS measures hot and cold ion populations with sufficient mass, angular and energy resolution. The instrument has a time resolution of 1 spin, which is 4 seconds. CIS covers a wide range of differential energy flux from 10^3 to 10^{10} $(cm^2 ssr)^{-1}$. This is made possible by having two sensors with different geometric factors. The sensors are the time of flight ion Composition and Distribution Function sensor (CODIF) and the Hot Ion Analyser (HIA).

HIA sensor has a quadrispherical, symmetrical analyser, also known as "top-hat" geometry, which has been previously used with great success. It analyses ions by energy/charge by electrostatic deflection inside this analyser. A cross section of the HIA sensor is shown in figure 5.3. The particle imaging is done by microchannel plate (MCP) electron multipliers and position encoding discrete anodes. The sensor has a 2 x 180 degree field of view sections. These two sections have different geometric factors with a factor of 25 between the high geometric factor and low geometric factor. The low geometric sector gives high angular resolution in the polar direction. This is achieved by having 8 x 5.625 degrees central anodes and 8 x 11.25 degrees other anodes. The high geometric factor section is divided into 16 x 11.25 degrees anodes. The anode sectioning can be seen in figure 5.4.

CODIF sensor is a mass/charge spectrometer with a 360 x 8 degrees field of view. In

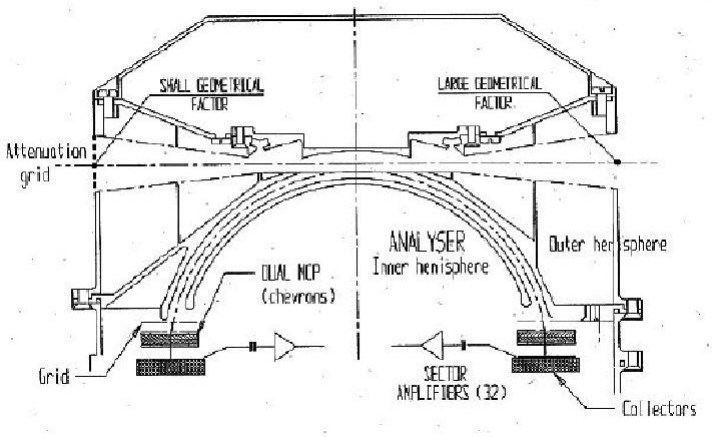

Figure 5.3: Cross section of HIA sensor [Reme et al., 1997]

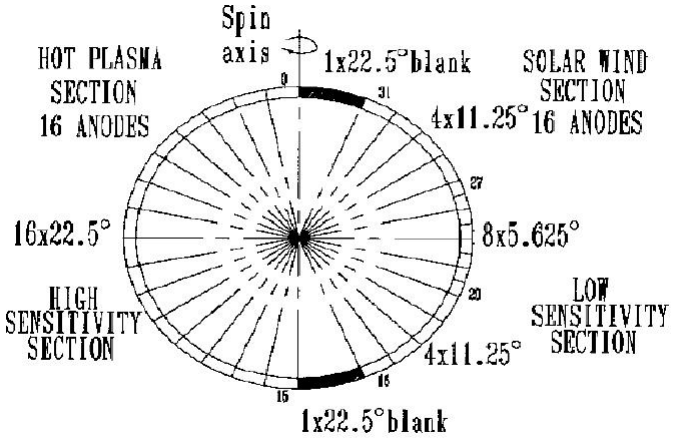

Figure 5.4: Anode sectioning in HIA sensor[Reme et al., 1997]

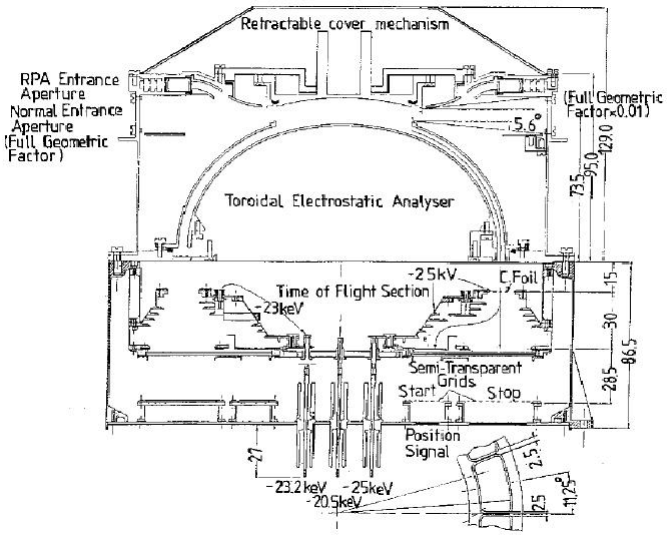

Figure 5.5: Cross section of CODIF sensor[Reme et al., 1997]

one spin it measures the 3D distribution function of different ion species including H+, He++, He+, O+. The cross section of this sensor is shown in figure 5.5. CODIF also uses two different geometric factors in order to cover the large dynamic range. It uses energy/charge selection by deflection in a rotationally symmetric toroidal electrostatic analyser and then Time of Flight (TOF) analysis. The angular resolution is achieved by the analyser being divided into 16 channels of 22.5 degrees each. A grid, which covers the entrance, provides 1 percent transmission over half the analyser entrance and 95 percent transmission over the other half of the entrance. The high transmission part covers azimuthal angle range of 0 to 180 degrees, while the low transmission part covers 22.5 to 157.5 degrees.

On-board data processing is used to overcome the problem of not being able to have continuous transmission of ion distributions due to limited downlink telemetry. The Data Processing System (DPS) controls the data collection from the two sensors. It formats the data for the telemetry channel, receives and executes any commands, and compresses the data.

5.3 Methodology

In this chapter we describe the work done to determine signatures of different SLAMS events using Cluster observations. We look at events that involve diffuse ions, gyrating ions and field aligned beam ions. For this work we study Cluster orbit plots and magnetic field data from Cluster FGM instrument to identify SLAMS events. Then plots from Cluster CIS are used for the analysis of the events. The CIS plots used are ion distribution plots in velocity space and these plots are generated using the clweb tool [http://clweb.cesr.fr]. The findings of the analysis are compared with similar ion distribution plots obtained from simulation work.

SLAMS events were identified in the following way. We first had to choose months when Cluster's orbit was crossing the appropriate region. Cluster had to be orbiting the dayside instead of the magnetotail so we had to choose events in mid-winter. Also Cluster had to be crossing the magnetopause or bow shock region as oppose to being well within the magnetosphere region. We used 6 hour orbit plots to determine these times.

Within these time slots, a number of SLAMS events were chosen by looking at FGM data from Cluster Active Archive and recording times where the magnetic field was significantly amplified by at least a factor of two above the background level. The FGM plots were also used to ensure that the events were at a time when the shock was predominantly quasi-parallel. Three of the SLAMS events chosen were from study by Lucek et al., 2008.

For the times that SLAMS events were observed, we studied the CIS HIA plots, showing the ion distribution in velocity space. We carried out an analysis using a code, provided by Steve Schwartz, Imperial College, to determine the shock normal vector on the plots. The shock normal is calculated from a model bow shock, based

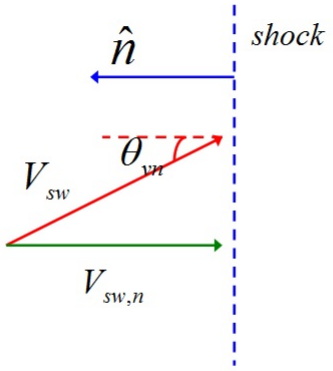

Figure 5.6: Schematic showing solar wind vector at angle θ_{vn} to the shock normal.

on the location of the spacecraft at the time of the shock crossing. This enabled us to identify the type of ions being observed in the plots. The code requires an input of x, y, z position of the spacecraft and the solar wind speed and it calculates the shock normal based on the chosen shock model.

Once the shock normal is found, the following steps enables us to determine whether the ions are specularly reflected ions, assuming that they have just been reflected: 1) Superimpose the shock normal vector on the $V_x - V_y$ velocity plot from the Cluster CIS data. 2) Add the shock plane perpendicular to the shock normal on the plot. 3) Add the solar wind velocity vector in the $-V_x$ direction. 4) Take the component of the solar wind vector in the shock normal direction ($V_{sw,n}$) and reflect it in the shock plane. 5) Add this vector to the plot and this indicates the region in velocity space where specular reflection starts. If this coincides with the enhanced ion activity in the plot then that shows that those ions are specularly reflected. This is illustrated in the schematics in figures 5.6 and 5.7. We have neglected the v_z component, which is most appropriate for shock crossings in the ecliptic plane. The clweb data is for the $v_z = 0$ plane, so we have made this simplifying assumption.

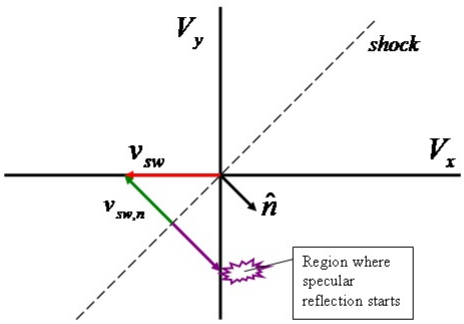

Figure 5.7: Schematic showing shock normal and region where specular reflection starts. The coordinate system is GSE, for comparison with the plots of observed ion distributions.

We chose events that were comparable to the simulations. If specularly reflected ions were present during the event, we determined whether they were gyrating or field aligned beams by superimposing the magnetic field vector onto the ion distribution plots. We looked at typical signatures of these events, such as timing of particle activity compared to timing of pulse, amplitude of pulse, whether the event is near shock nose or flanks.

We compare the signatures that we observe with similar ion distribution plots that we obtain from simulations. The method to obtain these plots is illustrated in figure 5.8. For these plots we select an x-range over which we want to observe the ions in the simulation box. For example, the range could be from $x_1 = 20.0$ to $x_2 = 80.0$. Then we choose a 2-D array of V_x against V_y with maximum velocity of $\pm V_m$. In this case $V_m = 20.0$ was appropriate for our simulation. For each ion within the chosen x-range, we determine its velocity components. If the velocity components lie within the range $-V_m < V_x < V_m$ and $-V_m < V_y < V_m$, then the counter is incremented.

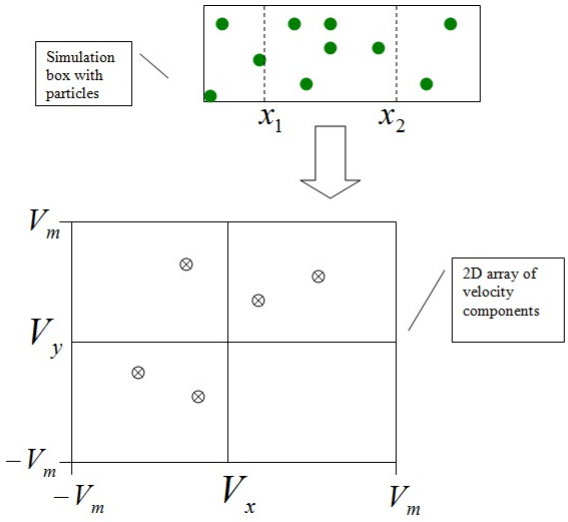

Figure 5.8: Schematic showing ions within a chosen x-range in a simulation and the corresponding velocities in the 2-D array

This is done for all the particles in the chosen x-range.

5.4 SLAMS events

5.4.1 Events table

The events table, which is table 5.1, shows the date, time in U.T and shock normal associated with some of the events that we studied. A selection of events were identified, and the two studied in more detail are shown in this table. Plots from Cluster FGM and CIS are used for the analysis. The FGM plots shows the time evolution of the magnitude of the magnetic field as measured by the four Cluster spacecraft for the events. The CIS plots are created from data from the HIA sensor and show the ion distribution function of H+ ions as described earlier in this chapter.

Table 5.1: Events table

event number	date	time (UT)	shock normal
1	30/03/2006	18:49:00 - 18:49:15	0.979,-0.135, 0.152
2	20/02/2002	17:07:10 - 17:07:18	0.888, 0.201, 0.413

5.4.2 Case study: event 1

In this case study we look at an event from the pulsation zone, where the pulsations seem to be in their growth phase. A SLAMS event that is labelled event 1 occurred on 30/03/2006, while Cluster is near the nose of bow shock. The pulse lasts from 18:49:00 UT to 18:49:15 UT, and reaches to about 20 nT above a background of about 5 nT. The shock normal is (0.979, -0.135, 0.152). We use data from Cluster spacecraft $C1$ and $C3$, which have a large separation distance between them. $C1$ is further out and at a GSE position of (13.09, -2.05, 3.23), while $C3$ is at a GSE position of (12.82, -3.38, 2.56). The x separation between them is 1700 km. From the magnetic field plots for this event (figure 5.9), it can be seen that $C3$ sees a period of pulsations for a longer time than $C1$. This suggests that the average position of the bow shock is moving outwards and then inwards because of the average nested signature from the two spacecraft observations.

We would expect to see pulsations being convected downstream and growing in the flow in the pulsation zone in this period. There is some evidence that the data suggests this. The plots showing magnetic field data for a shorter time interval (figure 5.10), show evidence that the pulsations are in their growth phase. With large spacecraft separations, it is difficult to make a correlation between pulsations seen at one spacecraft and then seen later at another spacecraft. Timings are strongly affected by the orientation of the wave fronts and the pulsation may change shape as it grows and propagates. Nevertheless, the data clearly shows younger pulsations in

$C1$ data, as expected since C1 is upstream of C3, with a major pulsation at 18:49:00 and a second smaller and narrower pulsation at 18:50:00. These can be compared to the complex structures consisting of four large pulsations seen in $C3$ at 18:50:00 and at 18:51:00. The increase in the number of pulsations indicate that the region of pulsation growth is being sampled. Assuming these pulsations are surrounded by unshocked solar wind with velocity approximately 300 km/s (Cluster Active Archive data), and with a C1-C3 separation of 1700 km, this implies that the pulsations are convecting and growing over approximately 5-10 seconds. This time scale is consistent with full shock simulations (Scholer et al., 2003).

The CIS C1 ion data (figure 5.11) shows several instances of cold beams, that are probably reflected gyrating beams, before the pulsation such as at 18:48:52. Between this time and the time pulse peaks, there are some complicated features such as gyrating bunches. There is also an arc seen in positive V_z at 18:48:56, which may be due to the deceleration and gyration of the reflected gyrating bunch seen earlier. During the pulsation, there is some evidence of additional cold components that have similar energy to solar wind. This indicates that the broadening and slowing of the solar wind distribution, which is seen in the energy spectrogram (CAA data, not shown), is due to multiple cold components rather than real thermalisation. The ion distributions are taken as cuts at $v_z = 0$ and therefore liable to miss any narrow range component out of this plane. Our conclusions are preliminary since a full analysis would require the three-dimensional geometry to be taken account including the directions of the magnetic field and shock normal. However, there is clear evidence of cold additional components, typically of reflected gyrating ions.

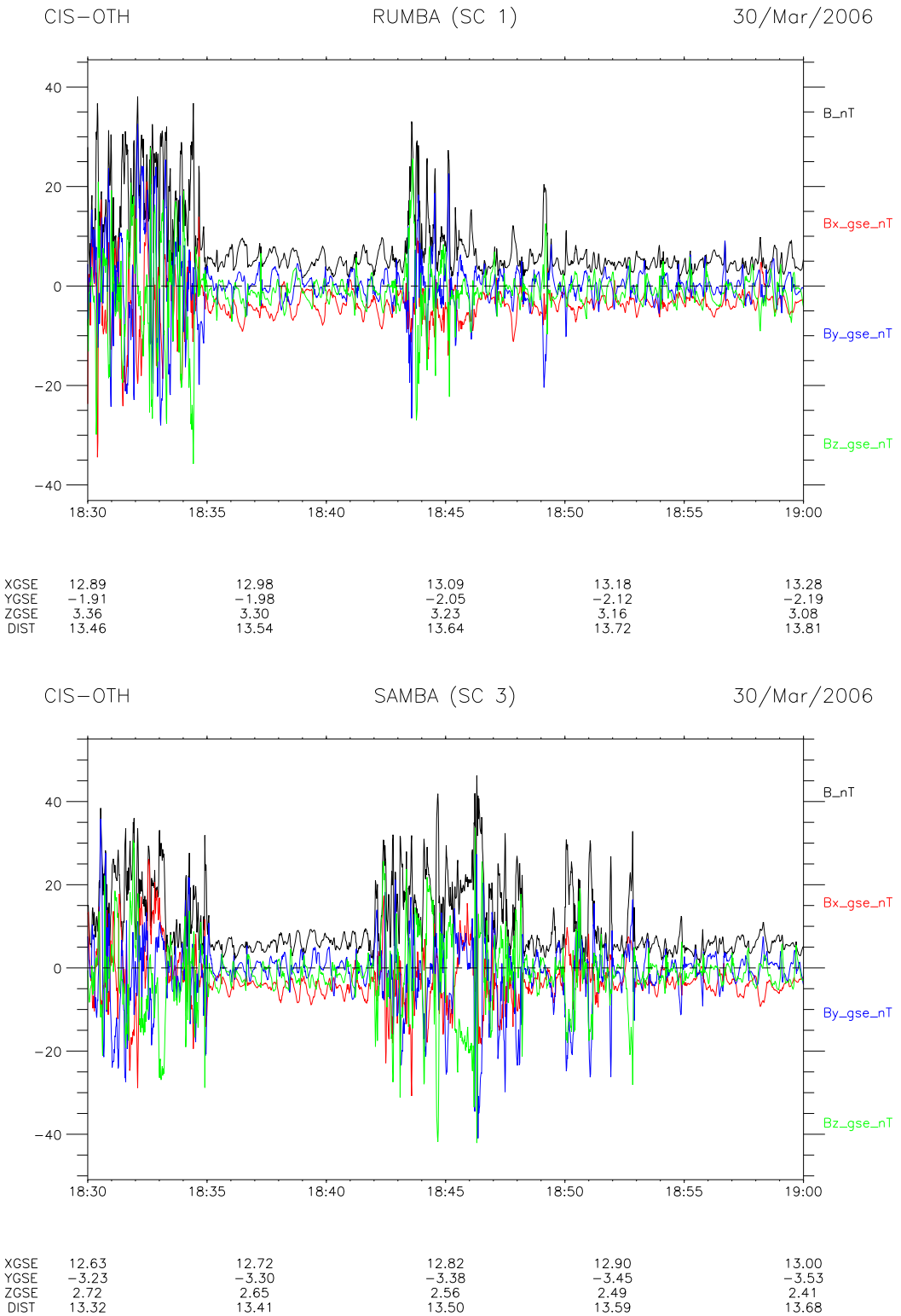

Figure 5.9: Case study event 1: C1 and C3 overview - magnetic field magnitude and components. Data at 1 second resolution [http://stereo.cesr.fr/clweb]

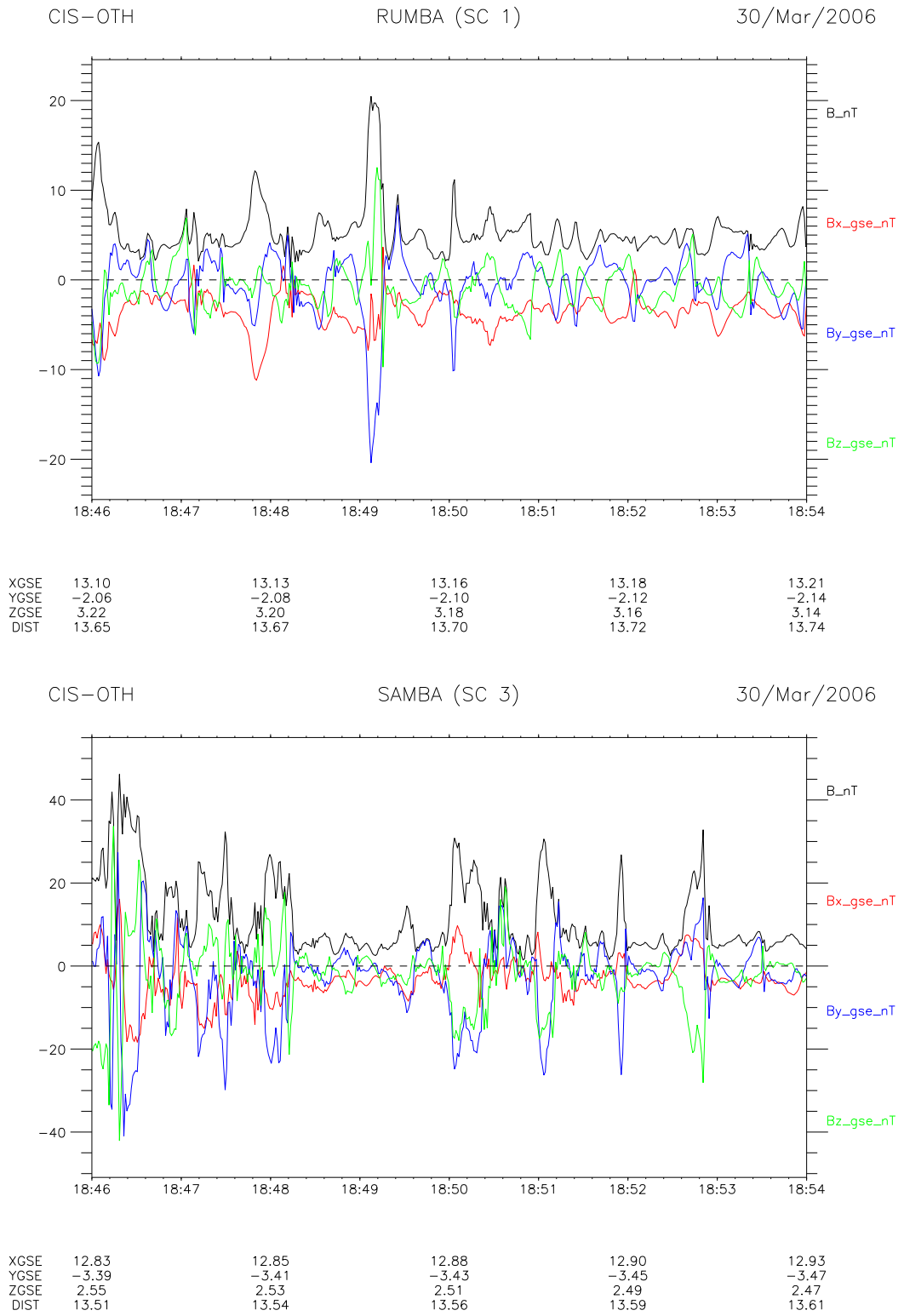

Figure 5.10: Case study event 1: C1 and C3 detailed view of pulsation events [http://stereo.cesr.fr/clweb]

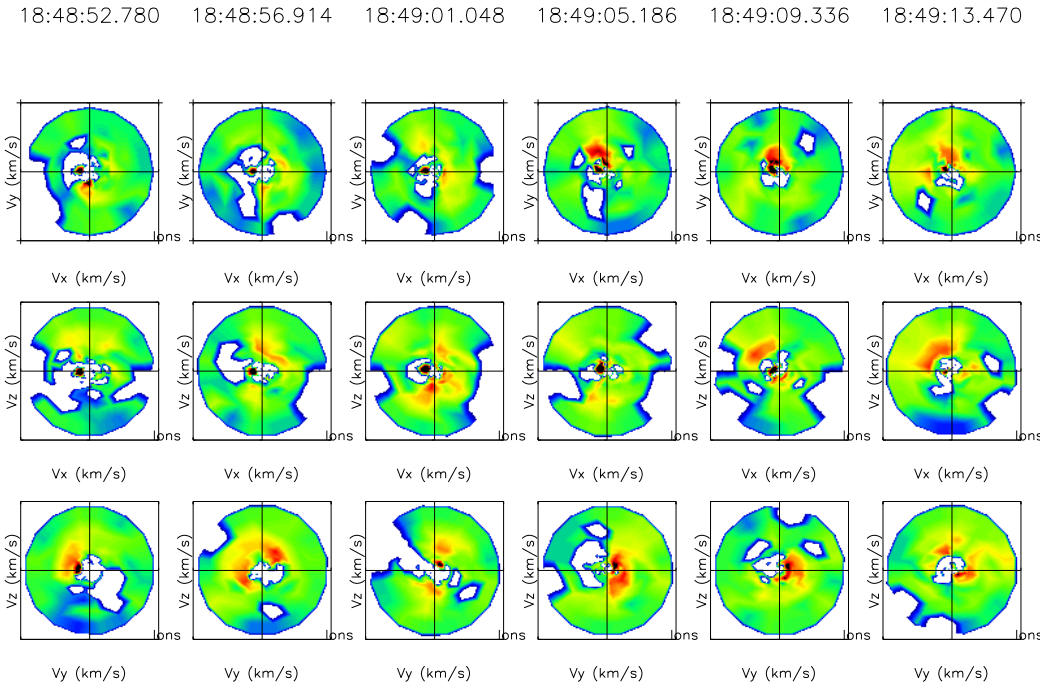

Figure 5.11: Case study event 1: CIS HIA data for interval around pulsation at 18:49:00 [http://stereo.cesr.fr/clweb]

5.4.3 Case study: event 2

A SLAMS event that occurred on 20/02/2002 shown in figure 5.12. This event is observed while Cluster is near the nose of the bow shock, and this is an isolated event. In this case the pulse lasts from 17.07.10 UT to 17.07.18 UT and reaches an amplitude of 47 nT. The shock normal is (0.888, 0.201, 0.413). There is a strong feature in the CIS HIA plots just prior to the event at 17.06.57 UT and last till 17.07.21 UT, so there is a considerable period over which the ions last. However, this is not seen in the other spacecraft and so it may be a anomalous result. There is no signs of splitting of the pulse in this case.

This event is an isolated event where the pulsation is surrounded by solar wind, so we can expect there to be presence of diffuse ions in the locality of the event. The Cluster spacecraft separation is small and there is very little variation between the spacecraft, as can be seen from the $C1234$ overview figure of the magnetic field (figure 5.13). We can see from figure 5.14 that magnetic field magnitude plot shows that there is a period of enhanced fluctuations (higher frequency than elsewhere) just before the large amplitude pulse that begins at 17:07:10. Broadening of the solar wind starts in this interval before the main pulse, indicating that this period is important for its interpretation.

An important feature to note can be seen in the ion spectra figure in $C3$ above 10 keV for 1 spin at the time of the main pulsation. This feature is more clearly visible in the HIA plots from $C3$ for this event (figure 5.12) shown in previous section at 17:07:09. However, this feature is not seen in $C1$, although the spacecraft separation is small during this event. It is difficult to interpret whether the strong feature is real or not. It could be an instrument anomaly, which occurs just at the time of this isolated pulse. Alternatively, it could be a strong beam feature, but the timings of $C1$ and $C3$ may mean that it is not seen by $C1$.

CODIF data exists for $C1$ every 8 seconds. The CODIF plots (figures 5.15 and 5.16) show the presence of cold (narrow) features at solar wind - like energy seen at 17:06:50, which is just prior to the solar wind broadening seen in the ion spectra. There is a secondary population at $v_x = 0, v_y > 0$, which could be consistent with reflected gyrating ions, at 17:06:58 in the pre-pulse period of fluctuations. There is a broader signature in velocity space seen in the next distribution at 17:07:06, and then it returns to reflected gyrating beam at 17:07:14. It is possible that the broadened feature shown in the CODIF plot at 17:07:06 may be important, like the strong feature in the HIA plot at 17:07:09.

The event may look like an isolated event, but can be seen as having two parts: the pre-pulse period of enhanced fluctuations with signatures of reflected gyrating ions (cold, narrow features at solar wind-like temperature and energy) and a main pulse. This event is similar to that shown in Wilkinson et al., 1993 (figure 5.17), which also shows a disturbed period close to the pulsation, but in this case, after the main pulse. The presence of reflected gyrating ions during this event indicates that the spacecraft was closer to the pulsation zone than the isolated appearance indicates. The average bow shock position seems to have reached the spacecraft so that reflected gyrating ions are being produced nearby.

It is difficult to explain the differences with the Wilkinson et al., 1993 event, where the enhanced fluctuation period lies after the pulsation rather than before. It may be due to the combination of the motion of the pulsation through convection by solar wind and the average motion of the shock as it passes across the spacecraft. However, it is difficult to distinguish between the individual motion of pulsation and shock motion.

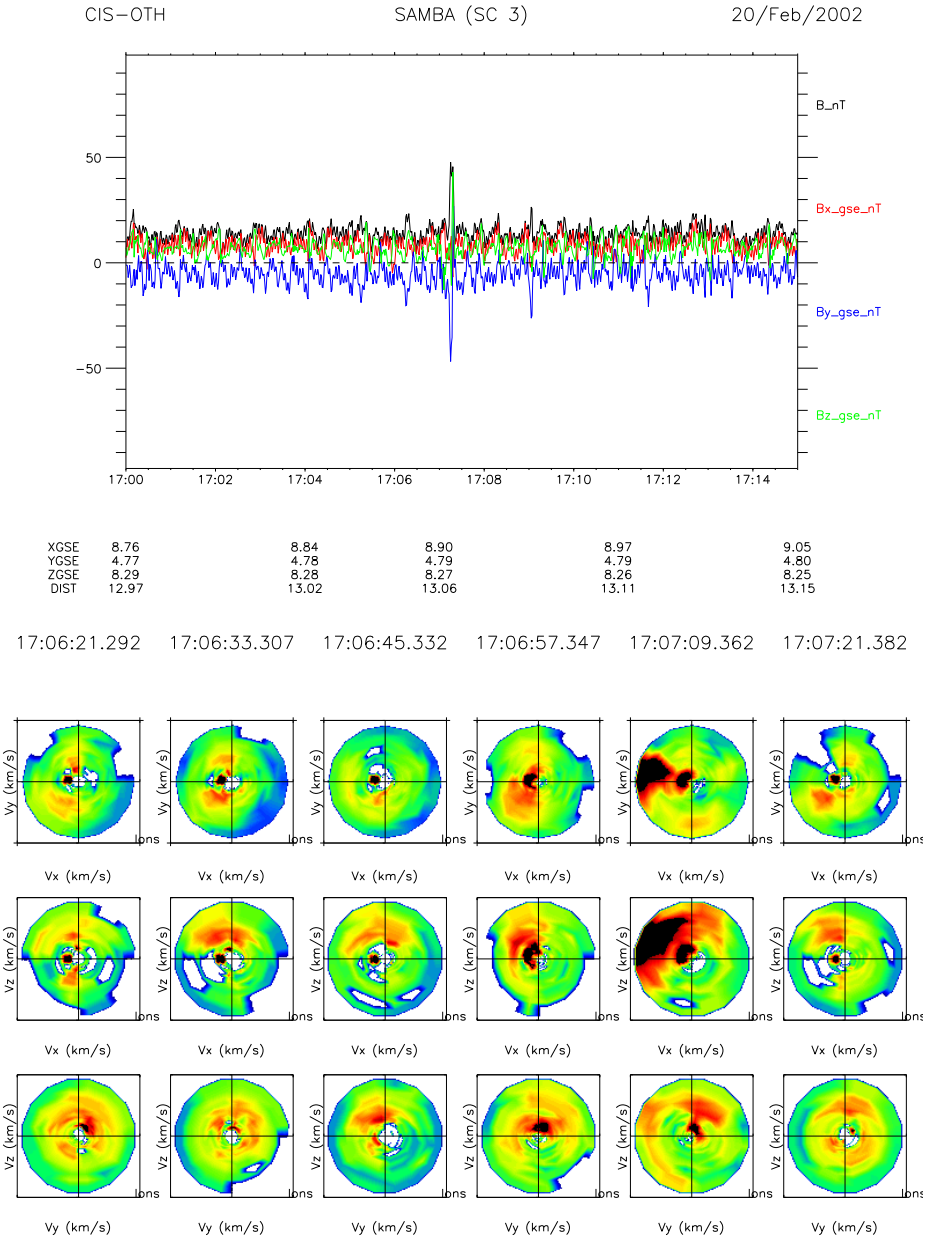

Figure 5.12: Event 2: FGM magnetic field plot (top) and CIS HIA particle distribution plot (below) [http://stereo.cesr.fr/clweb]

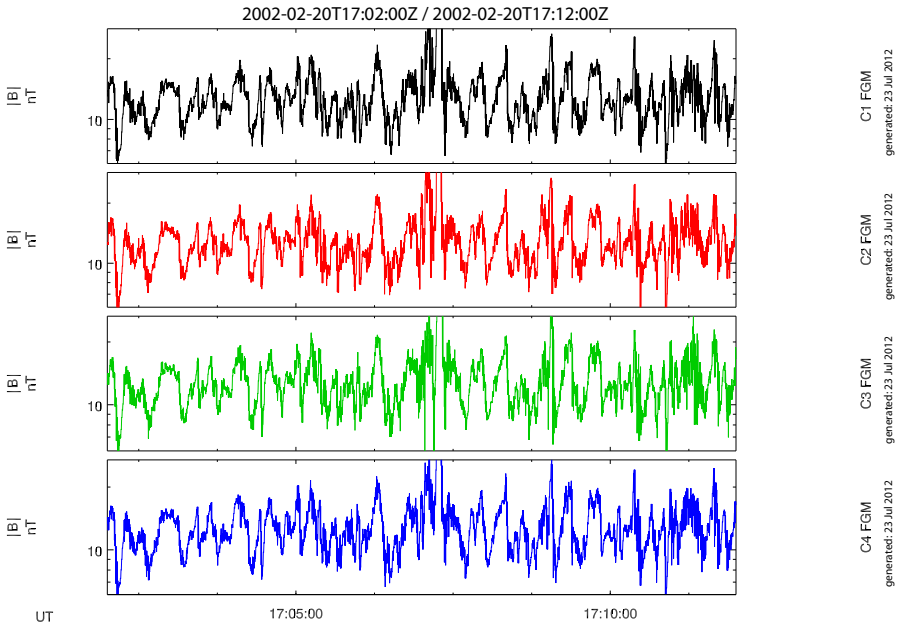

Figure 5.13: Case study event 2: C1234 overview [Cluster Active Archive]

5.5 Particle distribution plots

Although the simulations shown in chapter 4 are for a highly simplified system, we have plotted particle number distributions to identify any possible signatures of the interaction that might also be comparable with the Cluster observations. Simulations are carried out to generate plots of contours of particle partial density of the injected ions projected onto the $V_x - V_y$ plane and the $V_x - V_z$ plane. All particles are counted, not just those in the plot plane. This does not correspond exactly to the presentation of the CIS data from clweb, but does give a complete view of velocity space. The runs that are studied are E14 and E16 (see table 4.1 and figures 4.10 and 4.12 in chapter 4). Run E14 is an example of a strong interaction which has an injection density of 0.4 and is the backstreaming ions case for full pitch angle range of 110 - 180 degrees. Run E16 has injection density of 0.2 and pitch angle range of 110 - 130 degrees, so is for gyrating ions case.

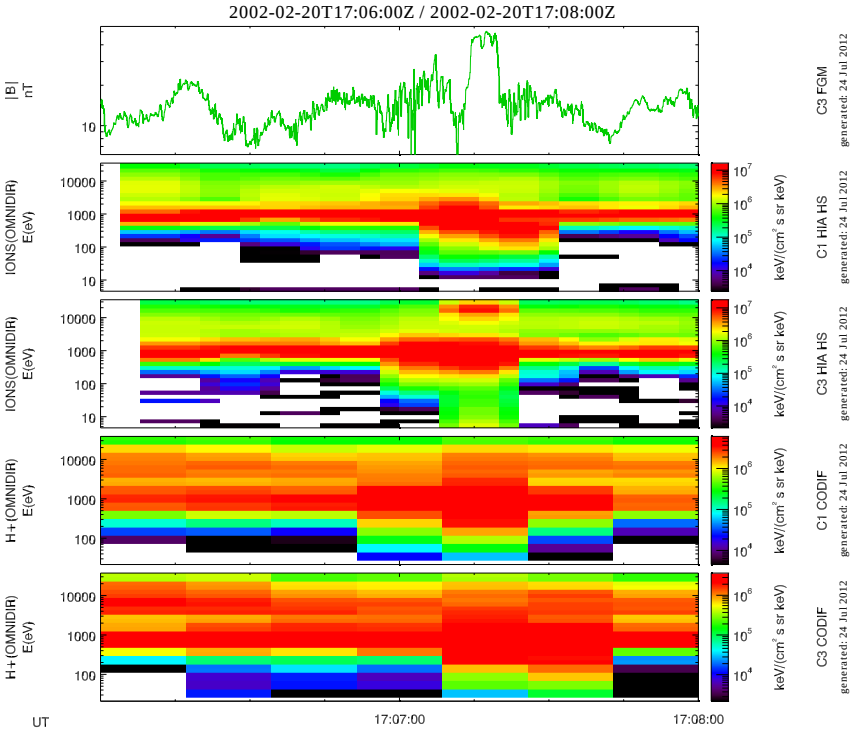

Figure 5.14: Case study event 2: C1 C3 ion spectra [Cluster Active Archive]

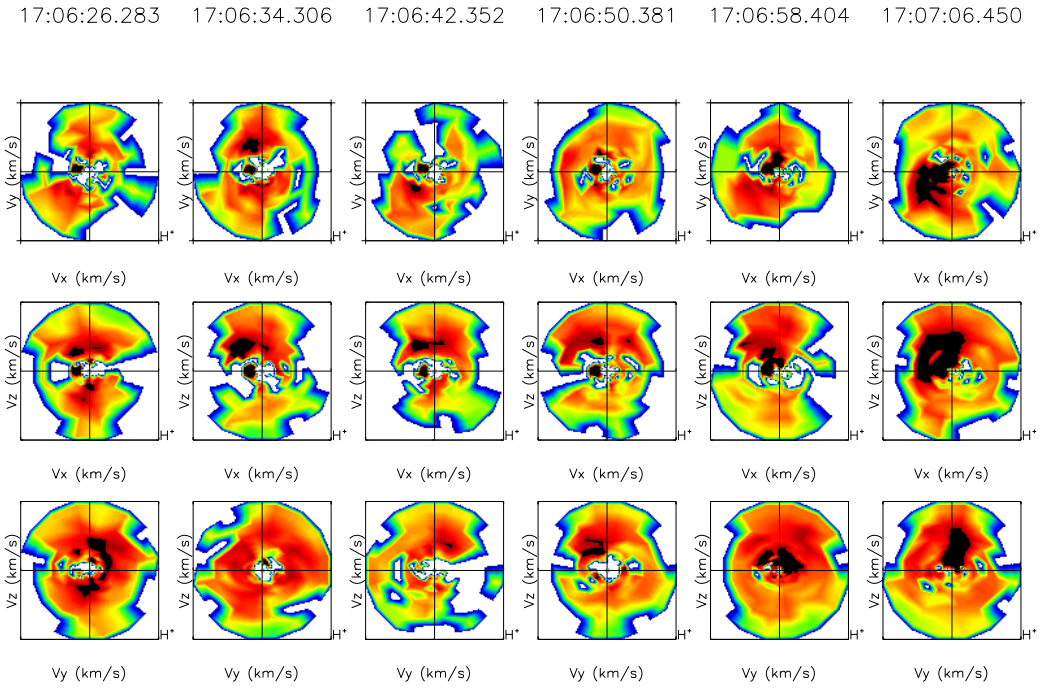

Figure 5.15: Case study event 2: C1 data of CODIF protons [http://stereo.cesr.fr/clweb]

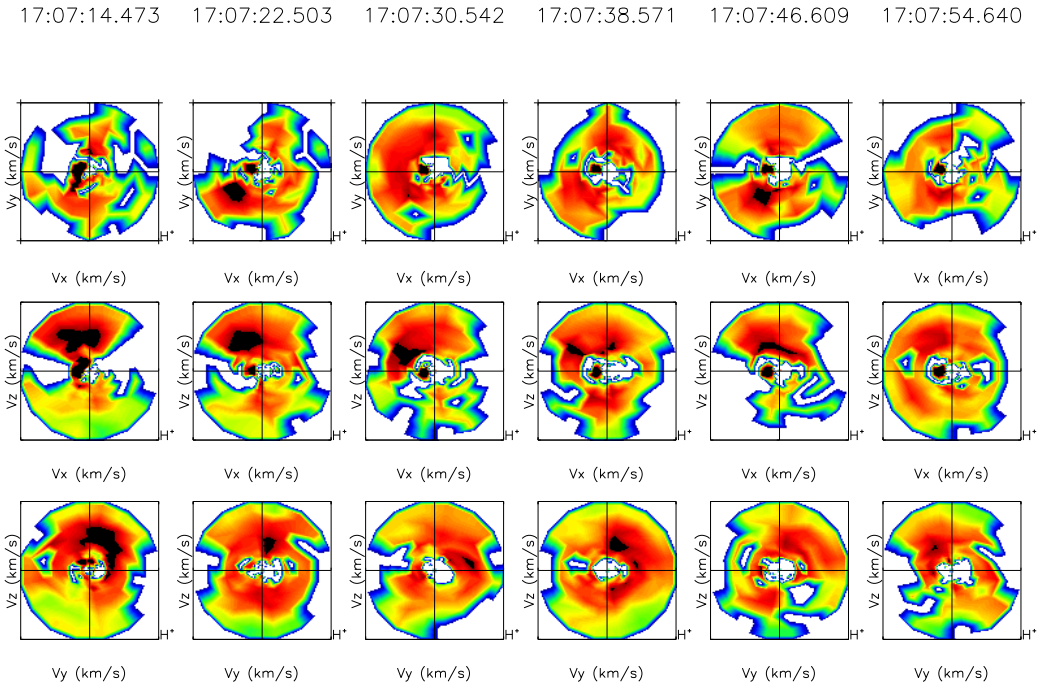

Figure 5.16: Case study event 2: C1 data of CODIF protons [http://stereo.cesr.fr/clweb]

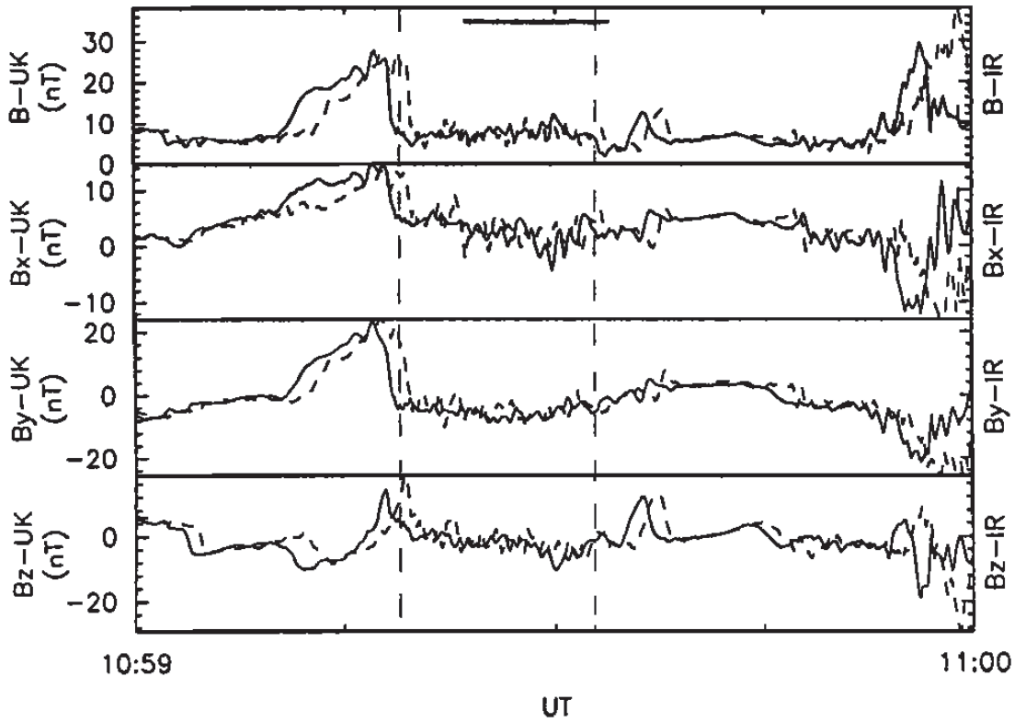

Figure 5.17: Magnetic field plots for SLAMS event as described in Wilkinson et al. 1993, figure 3b

After the launch of the leftward propagating pulsation seen in the magnetic field plot for run E14 in chapter 4 (see figure 4.10 at timestep 400 at x=50-55), there is evidence of deceleration of the energetic beam, with a characteristic arc in the $V_x - V_y$ plane. There is also a remnant positive V_z component, which eventually passes through the pulsation. These results can be seen in figure 5.18. Later in the interaction, at timestep 600 and at x=45-50 in run E14 in figure 4.10, we see that inside the split pulse there is a evidence of energetic ions with low average velocity in the plasma frame. There is a clear positive V_z signature indicating bunches of gyrating ions. This can be seen in figure 5.19. Much later in the interaction, plots in figure 5.20 show particles with low average velocity in plasma frame. There is a small spread in velocity from the origin.

Looking at run E16 at timestep 300 at x=50-55, in figure 4.12, we show corresponding plots in figure 5.21 for the time just after the interaction which launches the leftward propagating pulsation. The plots show deceleration of particles in the x direction and gain of negative V_z during the interaction with the wave. The plots in figure 5.22 show a mix of populations, mostly gyrating bunches but also a field aligned component. At a much later time and in the middle of the interaction region, the plots in figure 5.23 show gyrating clumps of particles.

5.6 Discussion

Comparisons of simulations with Cluster observations is difficult due to the uncertainties involved. The pulsations may change spatially and temporally on shorter timescales than can be resolved by the instruments. The spacecraft separation for a particular event may not allow the pulsation growth signatures to be recorded. As mentioned in Lucek et al., 2008, when the separation is small, any differences in the

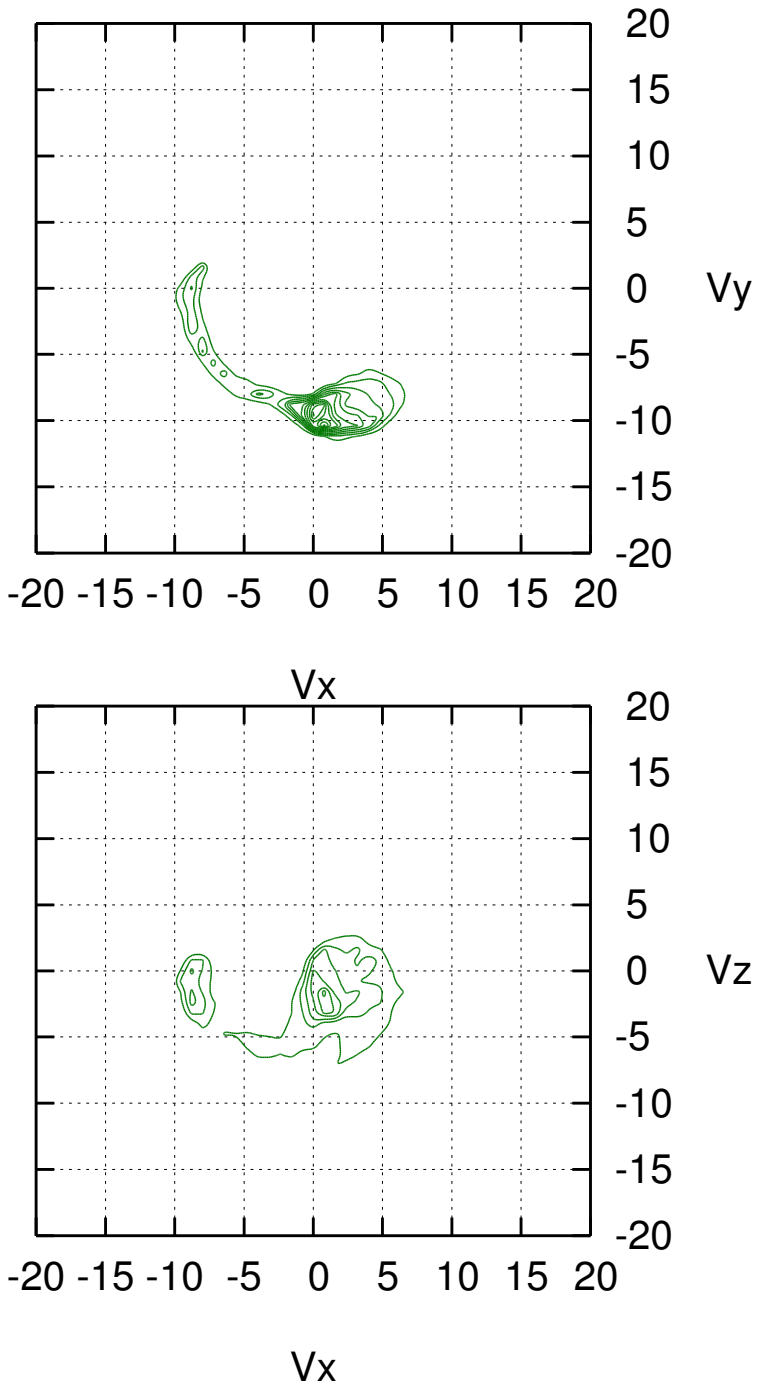

Figure 5.18: Particle number distribution with equal linearly spaced contours for run E14 - for $x = 50 - 55$ and timestep 400

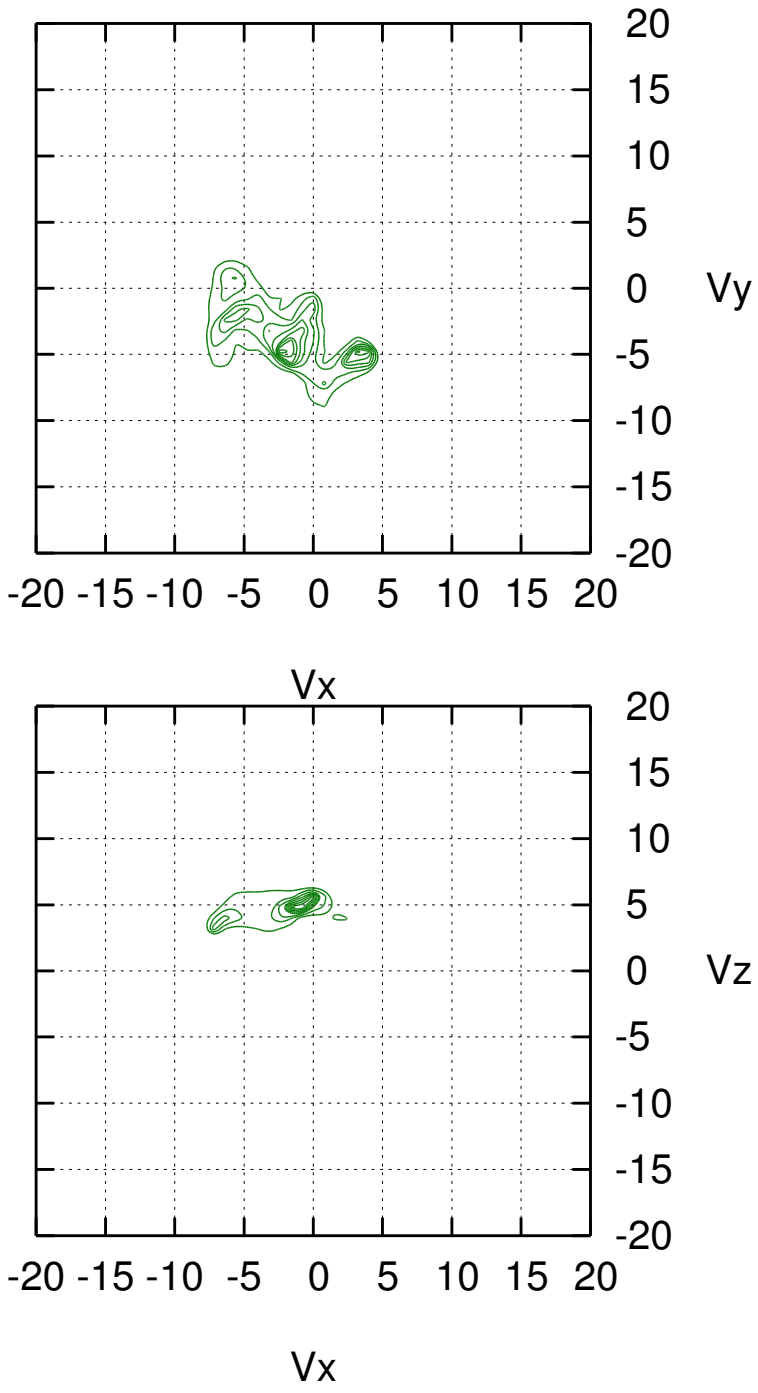

Figure 5.19: Particle number distribution with equal linearly spaced contours for run E14 - for $x = 45 - 50$ and timestep 600

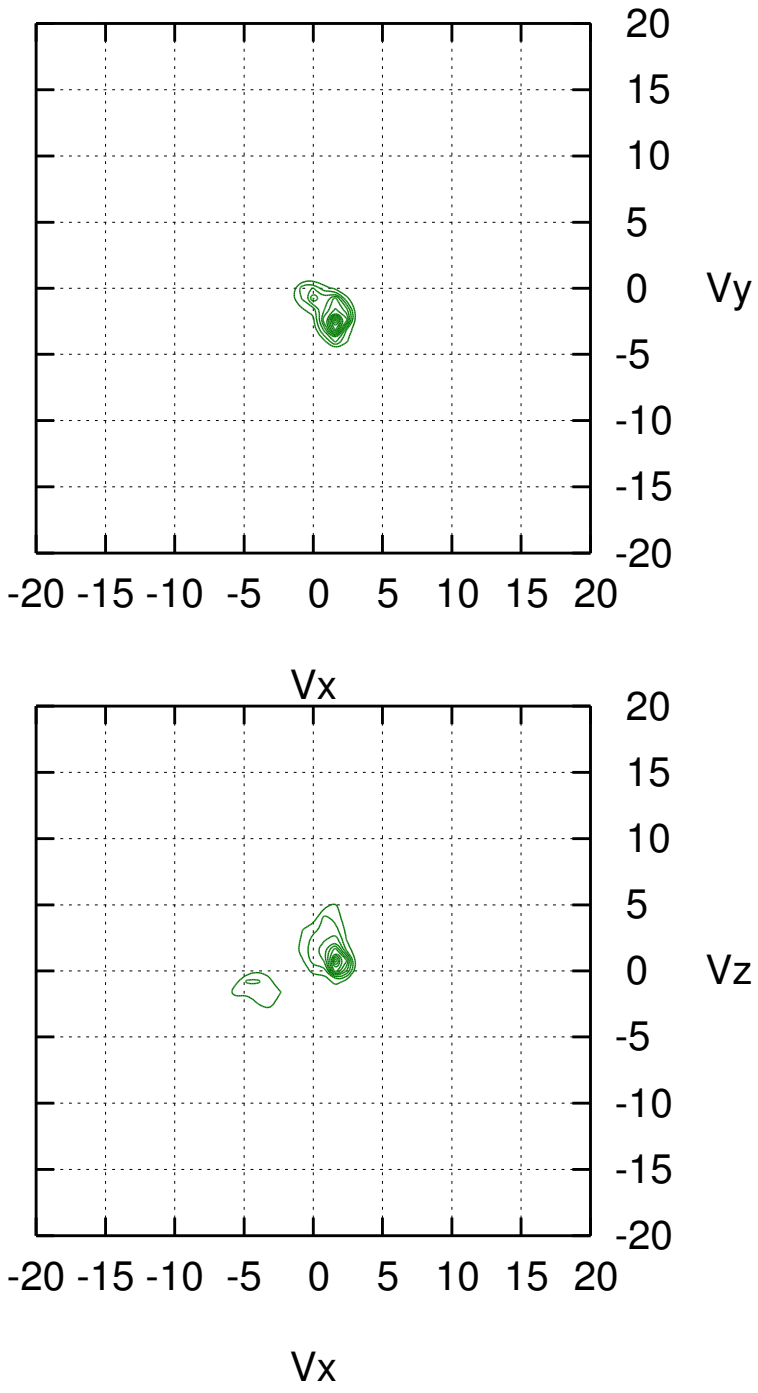

Figure 5.20: Particle number distribution with equal linearly spaced contours for run E14 - for $x = 50 - 55$ and timestep 1200

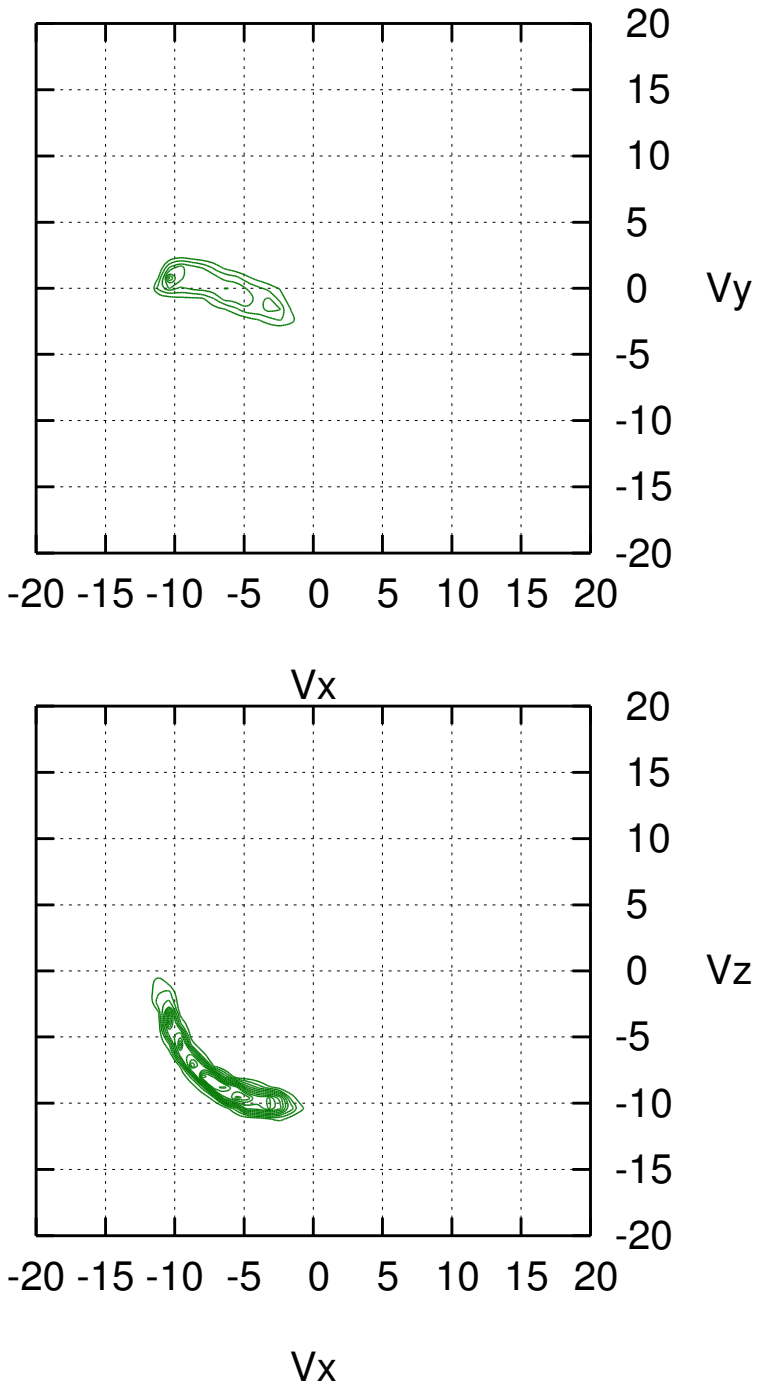

Figure 5.21: Particle number distribution with equal linearly spaced contours for run E16 - for $x = 50 - 55$ and timestep 300

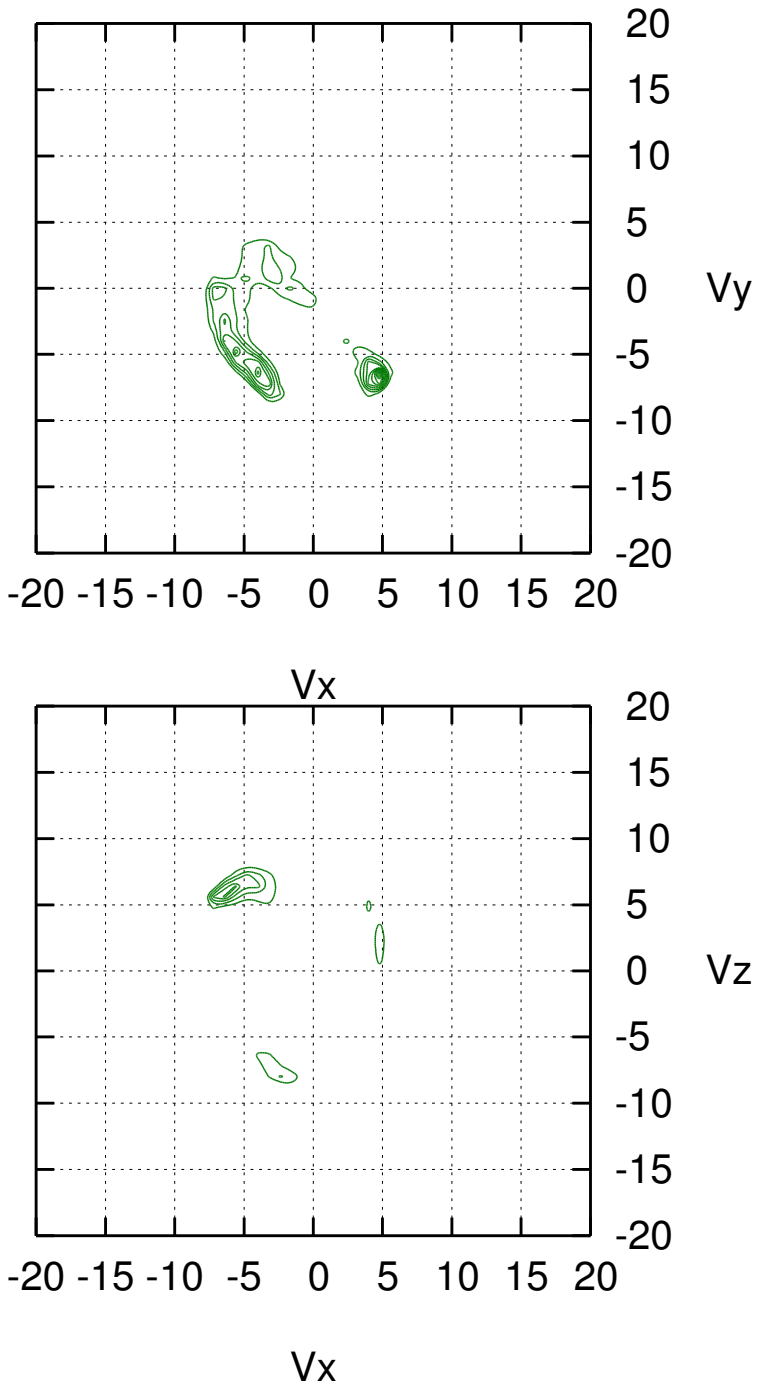

Figure 5.22: Particle number distribution with equal linearly spaced contours for run E16 - for $x = 50 - 55$ and timestep 600

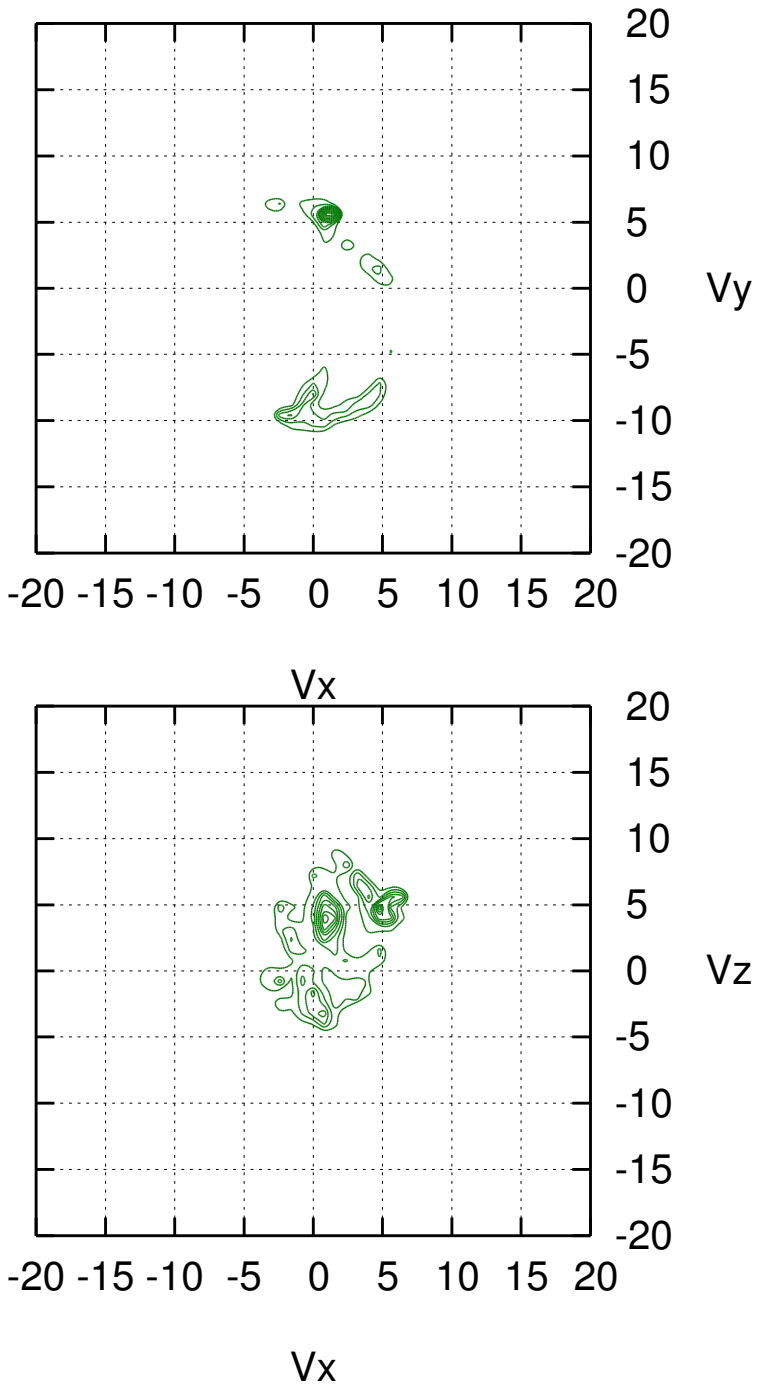

Figure 5.23: Particle number distribution with equal linearly spaced contours for run E16 - for $x = 50 - 55$ and timestep 1200

profile of the pulsations may be due spatial gradients in the magnetic field structures rather than due to time evolution of the pulsations. Also, the time taken to record the ion distributions may be large relative to the magnetic field changes, so it may be difficult to assess the exact situation. It may be difficult to distinguish between the motion of average position of bow shock relative to the spacecraft and the motion of the pulsations being convected by the solar wind and these may affect the results. Often the events are embedded pulsations and so it is difficult to disentangle the full history of any one pulsation.

The simulations suggest that the pulsation, once launched, does not remain with the ions responsible for the interaction. This is different from the picture where the pulsation simply grows from the existing ULF wave, in which case one expects the ions responsible for the growth to stay with the wave.

The simulations suggest that coupling to the pulse can be strong, so that there is a prominent component of ions at the end of the interaction with low average velocity in the plasma frame. For the case of the gyrating beam interaction, the remnants are gyrating bunches, which may explain the velocity space structure seen in the quasi parallel pulsation zone. Distributions at the start of the interaction show strong deceleration of backstreaming ions and a gyrating signature with a positive V_z component. However, in the diffuse ions case, there is no evidence of strong pulsation growth except for unrealistically high densities.

An interesting and strong feature is observed in the Cluster CIS HIA particle distribution plots at the time of a pulsation for one of the events. However, there is some uncertainty as to whether it is real or not as it is seen in one of the spacecraft but not the other, even when the spacecraft separation is small.

In some of the events we see a period of high fluctuations or shocklets just prior to or just after a pulsation. Whether the shocklets are observed before or after the

pulse may be due to some combination of motion of the average position of the bow shock and the downstream convection of the magnetic structures by the solar wind. However, it is difficult to disentangle the effects of these in the observations.

Chapter 6

Discussion

Both the simulation and Cluster observation work show that the backstreaming ions and diffuse ions are associated with the growth of the SLAMS pulsations. Although the backstreaming ions cause strong coupling with the pulse and cause a narrow feature to develop, the diffuse ions show a relatively weaker interaction with the pulse and no narrow feature is generated. A strong interaction with the diffuse ions requires an unrealistically high density. However, in both cases, it is clear that the ULF wave does not simply just grow, as the pulse does not remain with the ions that cause the interaction. Instead the pulse splits and launches a new leftward wave in the simulation frame. This result may explain the spacecraft observation that pulsations appear to slow down. The pulsations may appear to slow down in the spacecraft frame as a result of the production of the leftward propagating wave in the simulation frame.

The model presented here is different to the model originally suggested (Schwartz et al., 1992) where large SLAMS grow from the wave field and propagate faster in the solar wind frame in the upstream direction (away from the shock) and so appear

to be moving slower in the shock frame, until they eventually stand in the shock frame. The problem with this model is that there is no mechanism specified for the wave growth. The simulations support a new model where the beam-pulse coupling is strong enough to launch a pulse in the beam direction, away from the shock. This explains why pulsations are not always seen with associated gyrating or beam ions. The remnants of beam-pulse coupling explain regions where ions are seen.

Our findings are consistent with the mechanism for the interaction between the back-streaming ions and the pulse as described by Scholer and Burgess, 1992. Ions are decelerated and deflected by the pulse, causing a local density enhancement. Since the flow is frozen-in with the flux, the magnetic field increases. This causes a positive feedback loop to develop and background ions get decelerated and deflected by the enhanced magnetic field. We find that there is a local density enhancement during the interaction, which is consistent with the mechanism described by Scholer and Burgess, 1992 and with results of Onsager et al., 1991a.

We also find some additional features of this mechanism. The interaction causes a very narrow wave to develop. This then splits and launches a leftward propagating wave. Leftward here is equivalent to being in the direction upstream away from the shock. Some ions remain trapped in the remnants of the beam-pulse coupling region, some do eventually pass through, while in some cases they are reflected by the pulse. As the injection density increases, the number of ions that are transmitted through the pulse reduces. As the pulse size increases, the ions spend a longer time being trapped and reflected within the split pulse.

As ion injection density increases, the narrow feature that develops get increasingly larger and the leftward propagating wave that is launched, travels faster. The field aligned ions produce a stronger narrow peak than the gyrating ions. With a very large injection zone, there is very fast growth and amplitude of the magnetic field

magnitude reaches 4.0.

In the case of the diffuse ions, there is some growth of the pulse, but no narrow feature forms like in the backstreaming ions case. There is pulse splitting and a leftward propagating wave is launched. When $v_{\parallel}$ drift is not included, the leftward propagating wave is launched much later than in backstreaming ions case. The initial pulse size has to be large, that is about $b = 2$ before there is an effect of increasing the background diffuse ion density. When the density of the diffuse ions is increased, the leftward propagating wave increases in size. However an unrealistically high density is required to for strong coupling with the pulse.

It seems that diffuse ions cause more gradual growth of the pulsations, rather than the dynamic behaviour of the backstreaming or reflected ions. This agrees with the locality of the two different types of ions at the quasi-parallel shock. For the diffuse ions, either a very high almost unrealistic density is required or having a density gradient, which we have not included, compensates for it.

Particle distribution plots showing contours of particle partial density from simulations are compared with ClS HIA particle distribution plots from Cluster observations. However, it is difficult to compare the results of simulations with Cluster observations in this case due to the uncertainties involved. The pulsations may change spatially and temporally on shorter timescales than can be resolved by the instruments. The spacecraft separation for a particular event may not allow the pulsation growth signatures to be recorded. As mentioned in Lucek et al., 2008, when the separation is small, any differences in the profile of the pulsations may be due spatial gradients in the magnetic field structures rather than due to time evolution of the pulsations.

Also, the time taken to record the ion distributions may be large relative to the magnetic field changes, so it may be difficult to assess the exact situation. It may be difficult to distinguish between the motion of average position of bow shock relative

to the spacecraft and the motion of the pulsations being convected by the solar wind and these may affect the results. Often the events are embedded pulsations and so it is difficult to disentangle the full history of any one pulsation.

Nevertheless, there is some evidence of complex structure within the pulsations, which may correspond to the splitting seen in the simulations. The splitting is particularly evident in some events where there is presence of gyrating ions and a possible explanation is that the ion density may be high enough in this case to cause the splitting. The splitting is seen in plots of time evolution of the magnetic field and it would be better to use plots of magnetic field variation in x direction. However it is difficult to obtain a high level of accuracy in such plots.

Both observations and simulations suggest that for the case of the gyrating beam interaction, the remnants are gyrating bunches. This may explain the velocity space structure seen in the quasi parallel pulsation zone. An interesting and strong feature is observed in the Cluster CIS HIA particle distribution plots at the time of a pulsation for one of the events. However, there is some uncertainty as to whether it is real or not as it is seen in one of the spacecraft but not the other, even when the spacecraft separation is small.

In some of the events we see a period of high fluctuations or shocklets just prior to or just after a pulsation. Whether the shocklets are observed before or after the pulse may be due to some combination of motion of the average position of the bow shock and the downstream convection of the magnetic structures by the solar wind. However, it is difficult to disentangle the effects of these in the observations.

To conclude, we have found a number of interesting features from both the simulations and the Cluster observations and have reported these above. It should be noted however, that there are some limitations in the methods used and these need to be taken into account. There are difficulties associated with observations. It could be

that pulsations being studied may vary in space and time as the spacecraft observes it, which may mean missing vital observations. The observations are limited by the time resolution of the instruments being used and the number of spacecraft that are in the desired location at the appropriate time.

Similarly there are difficulties associated with simulations. The hybrid simulation method is used in most cases, which treats the electrons as a massless fluid and ions are particles. This means that the electron physics is not completely correct. The simulations are mostly done in 1-D, with some in 2-D and none in 3-D, so it is difficult to model 3-D effects accurately. Most simulations are for an ideal shock, but in reality the bow shock is curved with a foreshock that allows different parts to be in communication with each other. The simulations cover a small range of Mach number, but it is possible that behaviour may be different for stronger shocks.

Bibliography

[1] Anderson, K. A., Lin, R. P., Martel, F., Lin, C. S., Parks, G. K., Reme, H., (1979) Thin sheets of energetic electrons upstream from the Earth's bow shock. Geophys. Res. Lett. 6:401-404.

[2] Armstrong, T. P., Pesses, M. E., Decker, R.B., (1985) Shock drift acceleration. In: Tsututani, B.T., Stone, R.G. (Eds), Collisionless Shocks in the Heliosphere: Reviews of current research , Geophysics Monograph series, Vol 35. AGU, Washington, DC, pp. 271-285.

[3] Asbridge, J. R., Bame, S. J., Strong, I. B., (1968) Outward flow of protons from the Earth's bow shock. J. Geophys. Res. 73(12):5777.

[4] Bale, S. D., Burgess, D., Kellogg, P. J., Goetz, K., Monson, S. J., (1997) On the amplitude of intense Langmuir waves in the terrestrial electron foreshock. J. Geophys. Res. 102(11):11281-11286.

[5] Bame, S. J., Asbridge, J. R., Feldman, W. C., Gosling, J. T., Paschmann, G., Sckopke, N., (1980) Deceleration of the solar wind upstream from the Earth's bow shock and the origin of diffuse upstream ions. J. Geophys. Res. 85, 2981.

[6] Baumjohann, W., Treumann, R. A., (1996) Basic Space Plasma Physics.

[7] Blanco-Cano, X., Schwartz, S. J., (1995) AMPTE-UKS observations of low frequency waves in the ion foreshock. Adv. Space Res. 15, 97-101.

[8] Blanco-Cano, X., Omidi, N., Russell, C. T., (2006) Macrostructure of collisionless bow shocks: 2. ULF waves in the foreshock and magnetosheath. J. Geophys. Res (Space physics) 111, 10205.

[9] Burgess, D., (1989) Cyclic behaviour at quasi-parallel collisionless shocks. Geophys. Res. Lett. 16, 345-348.

[10] Burgess, D., Lucek, E.A., Scholer, M., Bale, S.D., Balikhin, M.A., Balogh, A., Horbury, T.S., Krasnoselskikh, V.V., Kucharek, H., Lembege, B., Mobius, E., Schwartz, S. J., Thomsen, M.F., Walker, S.N, (2005) Quasi parallel shock structure and processes, Space Science Reviews, 118, 205-222.

[11] Cairns, I. H., (1987a) A theory for the Langmuir waves in the electron foreshock. J. Geophys. Res. 92(11):2329-2342.

[12] Cairns, I. H., (1987b) The electron distribution function upstream from the Earth's bow shock. J. Geophys. Res. 92(11):2315-2327.

[13] $Cla\beta en$, H.T, Mann, G, (1998) Motion of ions reflected off quasi-parallel shock waves in the presence of large amplitude magnetic field fluctuations. Astron. Astrophys. 330, 381-388.

[14] Desai, M.I., Burgess, D., (2008) Particle acceleration at coronal mass ejection driven interplanetary shocks and the Earth's bow shock. J. Geophys. Res. 113, Article A00B06.

[15] Dubouloz, N., Scholer, M., (1993) On the origin of short large amplitude magnetic structures (SLAMS) upstream of quasi-parallel collisionless shocks. Geo-

phys Res. Lett. 20, 547-550.

[16] Dubouloz, N., Scholer, M., (1995) 2D hybrid simulations of short large amplitude magnetic structures (SLAMS) upstream of quasi-parallel collisionless shocks, Advanced Space Res. 15, 175-178.

[17] Eastwood, J. P., Balogh, A., Lucek, E. A., Mazelle, C., Dandouras, I., (2005) Quasi-monochromatic ULF foreshock waves as observed by four spacecraft Cluster mission: 1. Statistical properties. J. Geophys. Res. 110 A11219.

[18] Eastwood, J. P., Lucek, E. A., Mazelle, C., Meziane, K., Narita, Y., Pickett, J., Treumann, R. A., (2005) The foreshock. Space Sci. Rev. 118, 41-94.

[19] Fairfield, D. H., (1969) Bow shock associated waves observed in the far upstream interplanetary medium. J. Geophys. Res. 74, 3541.

[20] Filbert, P. C., Kellogg, P. J., (1979) Electrostatic noise at the plasma frequency beyond the Earth's bow shock. J. Geophys. Res. 84(13): 1369-1381.

[21] Fuselier, S.A., Thomsen, M.F., Gosling, J.T., Bame, S.J., Russell, C.T, (1986a) Gyrating and intermediate ion distributions upstream from the earth's bow shock, J. Geophys. Res. 91, 91.

[22] Fuselier, S. A., Thomsen, M.F., Gary, S.P., Bame, S.J., Russell, C.T., Parks, G.K, (1986b) The phase relation between gyrophase-bunched ions and MHD-like waves, Geophys. Research Lett. 13, 60.

[23] Fuselier, S.A.,Gosling, J. T., Thomsen, M.F., (1986c) The motion of ions specularly reflected off a quasi-parallel shock in the presence of large amplitude, monochromatic MHD waves, J. Geophys. Res. 91, 4163-4170.

[24] Fuselier, S.A., Lennartsson, O.W., Thomsen, M.F., Russell, C.T., (1990) Specularly reflected He2+ at high Mach number quasi-parallel shocks. J. Geophys. Res. 95, 4319-4325.

[25] Fuselier, S.A., Thomsen, M.F, (1992) He2+ in field-aligned beams: ISEE results. Geophys. Res. Lett. 19, 437-440.

[26] Fuselier, S. A., Thomsen, M. F., Ipavich, F. M., Schmidt, W. K. H., (1995) Suprathermal He2+ in the Earth's foreshock region. J. Geophys. Res. 100, 17107.

[27] Giacalone, J., Schwartz, S.J., Burgess, D., (1993) Observations of suprathermal ions in association with SLAMS, Geophys. Res. Lett. 20, 149-152.

[28] Gosling, J. T., Asbridge, J. R., Bame, S. J., Paschmann, G., Sckopke, N., (1978) Observations of two distinct populations of bow shock ions in the upstream solar wind. Geophys. Res. lett. 5, 957-960.

[29] Gosling, J. T., Thomsen, M. F., Bame, S.J., Feldman, W.C., Paschmann, G., Sckopke, N., (1982) Evidence for specularly reflected ions upstream from the quasi-parallel bow shock, Geophys. Res. Lett. 9, 1333-1336.

[30] Gosling, J. T., Thomsen, M. F., (1985) Specularly reflected ions, shock foot thickness and shock velocity determinations in space. J. Geophys. Res. 90, 9893.

[31] Gosling, J. T., Thomsen, M.F., Bame, S. J., Rissell, C.T (1989) In reflection and downstream thermalization at the quasi-parallel bow shock. J. Geophys. Res. 94, 10027-10037.

[32] Greenstadt, E. W., Green, I, M., Inouye, G.T ., Colburn, D.S., Binsack, J.H., Lyon, E.F., (1970a) Dual satellite observations of Earth's bow shock I: The thick pulsation shock. Cosmic Elect. 1, 160-177.

[33] Greenstadt, E. W., Green, I, M., Inouye, G.T ., Colburn, D.S., Binsack, J.H., Lyon, E.F., (1970b) Dual satellite observations of Earth's bow shock II: Field-aligned upstream waves. Cosmic Elect. 1, 279-296.

[34] Greenstadt, E. W., Green, I, M., Inouye, G.T ., Colburn, D.S., Binsack, J.H., Lyon, E.F., (1970c) Dual satellite observations of Earth's bow shock. III: Field determined shock structure. Cosmic Elect. 1, 316 327.

[35] Greenstadt, E. W., (1974) Preliminary investigation of interplanetary shock structure: Quasi-parallel shocks. Technical Report.

[36] Greenstadt, E. W., Russell, C. T., Formisano, V., Hedgecock, P.C., Scarf, F. L., Neugebauer, M., Holzer, R. E., (1977) Structure of the quasi-parallel, quasi-laminar bow shock. J. Geophys. Res. 82, 651 666.

[37] Gurgiolo, C., Parks, G. K., Mauk, B. H., (1983) Upstream gyrophase bunched ions: a mechanism for creation at the bow shock and the growth of velocity space structure through gyrophase mixing. J. Geophys. Res. 88, 9093.

[38] Hoppe. M.M., Russell, C.T., (1980) Whistler mode wave packets in the Earths foreshock region. Nature 287, 417-420.

[39] Hoppe. M. M., Russell, C. T., Frank, L. A., Eastman, T. E., Greenstadt, E. W., (1981) Upstream hydromagnetic waves and their association with backstreaming ion populations: ISEE 1 and 2 observations. J. Geophys. Res. 86, 4471.

[40] Hoppe. M.M., Russell, C.T., (1983) Plasma rest frame frequencies and polarisations of the low frequency upstream waves: ISEE 1 and 2 observations, J. Geophys. Res. 88, 2021-2028.

[41] Hoshino, M., Terasawa, T., (1985) Numerical study of the upstream wave exci-

tation mechanism 1. Nonlinear phase bunching of beam ions. J. Geophys. Res. 86, 4471.

[42] Ipavich, F. M., Gloecker, G., Hamilton, D. C., Kistler, L. M., Gosling, J. T., (1988) Protons and alpha particles in field aligned beams upstream of the bow shock. Geophys. Res. Lett. 15, 1153.

[43] Kaufmann, R. L., (1967) Shock observations with the Explorer 12 Magnetometer, J. Geophys. Res. 72, 2323-2342.

[44] Kuramitsu, Y., Hada, T., (2008) Nonadiabatic interaction between a charged particle and an MHD pulse, Nonlin. Processes Geophys., 15, 265-273.

[45] Laakso, H., Taylor, M., Escoubet, C. P., (2010) The Cluster Active Archive.

[46] Le, G., Russell, C. T., (1992a) A study of ULF wave foreshock morphology-I:ULF foreshock boundary. Planet. Space Science. 40, 1203-1213.

[47] Le, G., Russell, C. T., (1992b) A study of ULF wave foreshock morphology-II:spatial variation of ULF waves. Planet. Space Science. 40, 1215-1225.

[48] Lin, R. P., Meng, C. I., Anderson, K. A., (1974) 30- to 100-keV protons upstream from the earth's bow shock. J. geophys. Res. 79, 489.

[49] Lucek, E. A., Horbury, T., Balogh, A., Dandouras, I., Reme, H., (2004) Cluster observations of structures at quasi-parallel bow shocks, Ann. Geophys., 22, 2309-2313.

[50] Lucek, E. A., Horbury, T. S., Dandouras, I., Reme, H., (2008) Cluster observations of the Earths quasi-parallel bow shock, J. Geophys. Res. 113.

[51] Lyu, L.H, Kan, J. R., (1990) Ion leakage, ion reflection, ion heating and shock

front reformation in a simulated supercritical quasi parallel collisionless shock, Geophys. Res. Lett. 17, 1041-1044.

[52] Mann, G., Luhr, H., Baumjohann, W., (1994) Statistical analysis of short large amplitude magnetic field structures in the vicinity of the quasi-parallel bow shock. J. Geophys. Res. 99, 13,315 13, 323.

[53] Mann, G., Classen, H. T., (1995) Electron acceleration to high energies at quasi parallel shock waves in the solar corona., Astron. Astrophys., 304, 576.

[54] Ness, N. F., Scearce, C. S., Seek, J.B., (1964) Initial results of the IMP-1 magnetic field experiment, J. Geophys. Res. 69, 3531.

[55] Omidi, N., Winske, D., (1990) Steepening of kinetic magnetosonic waves into shocklets: simulations and consequences for planetary shocks and comets, J. Geophys. Res., 95, 2281.

[56] Omidi, N., Blanco-Cano, X., Russell, C. T., (2005) Macrostructure of collisionless bow shocks: 1. scale lengths. J. Geophys Res (Space physics) 110, 12212.

[57] Onsager, T. G ., Thomsen, M. F., Gosling, J.T., Bame, S.J., Russell, C.T., (1990) Survey of coherent ion reflection at the quasi-parallel bow shock. J. Geophys Res. 95, 2261-2271.

[58] Onsager, T. G., Winske, D., Thomsen, M. F., (1991a) Interaction of a finite length ion beam with a background plasma: reflected ions at the quasi-parallel bow shock, J. Geophys. Res. 96, 1775- 1788.

[59] Onsager, T. G., Winske, D., Thomsen, M. F., (1991b) Ion injection simulations of quasi-parallel shock reformation, J. Geophys. Res. 96, 21,183 - 21,194.

[60] Pantellini, F. G. E., Heron, A., Adam, J. C., Mangeney, A., (1992) The role of the whistler precursor during the cyclic reformation of a quasi parallel shock, J. Geophys. Res. 97, 1303.

[61] Paschmann, G., Sckopke, N., Bame, S. J., Asbridge, J. R., Gosling, J. T., Russell, C. T., Greenstadt, E. W., (1979) Association of low frequency waves with suprathermal ions in the upstream solar wind, Geophys. Res. Letters, 6:209-212.

[62] Paschmann, G., Sckopke, N., (1983) Ion reflection and heating at the earth's bow shock. In: Haerendel, G., Battrick, B. (Eds), Topics in Plasma-, Astro- and Space Physics. Max-Planck-Institut fur Physik und Astrophysik, Garching, Germany, pp.139.

[63] Reme, H. et al., (1997) The Cluster Ion Spectrometry (CIS) experiment, Space Science Reviews. 79, 303-350.

[64] Russell, C. T., Childers, D.D., Coleman Jr., P.J., (1971) OGE 5 observations of upstream waves in the interplanetary medium: discrete wave packets, J. Geophys. Res. 76, 845.

[65] Russell, C. T., Kivelson, M. G., (1995) Introduction to Space Physics.

[66] Scholer, M., Gloecker, G., Ipavich, F. M., Hovestadt, D., Klecker, B., (1979) Pitch angle distributions of energetic protons near the Earth's bow shock. Geophys. Res. Lett. 6, 707-710.

[67] Scholer, M., Terasawa. T., (1990) Ion reflection and dissipation at quasi-parallel collisionless shocks, Geophys. Res. Lett., 17, 119.

[68] Scholer, M., Burgess, D., (1992) The role of upstream waves in supercritical quasi parallel shock reformation, J. Geophys. Res. 97, 8319-8326.

[69] Scholer, M., (1993) Upstream waves, shocklets, short large amplitude magnetic structures and the cyclic behaviour or oblique quasi-parallel collisionless shocks, J. Geophys. Res. 98, 47-57.

[70] Scholer, M., Kucharek, H., Trattner, K. J., (1998) Injection and acceleration of energetic particles at collisionless shocks. Adv. Space Res. 21, 533-542.

[71] Scholer, M., Kucharek, H., Iku, S., (2003) Short large amplitude magnetic structures and whistler wave precursors in a full particle quasi-parallel shock simulation, J. Geophys Res. 108.

[72] Schwartz, S.J., Thomsen, M.F., Gosling, J.T., (1983) Ions upstream of the Earth's bow shock: a theoretical comparison of alternative source populations. J. Geophys. Res. 88, 2039.

[73] Schwartz, S.J., Burgess, D., (1984) On the theoretical/observational comparison of field- aligned ion beams in the Earths foreshock, J. Geophys. Res. 89, 2381.

[74] Schwartz, S.J., (1991) Magnetic field structures and related phenomena at quasi-parallel shocks, Advanced Space Res. 11, 231.

[75] Schwartz, S.J., Burgess, D., (1991) Quasi-parallel shocks: a patchwork of three-dimensional structures, Geophys. Res. Lett. 18, 373-376.

[76] Schwartz, S. J., Burgess, D., Wilkinson, W. P., Kessel, R. L., Dunlop, M., Luhr, H., (1992) Observations of short large amplitude magnetic structures at a quasi-parallel shock, J. Geophys. Res. 97, 4209-4227.

[77] Schwartz, S. J., Owen, C., Burgess, D., (last revision 2004) Astrophysical Plasmas on-line book.

[78] Sonnerup, B.U.O., (1969) Acceleration of particles reflected at a shock front. J. Geophys. Res. 74, 1301.

[79] Sugiyama, T., Fujimoto, M., (2001) Quick ion injection and acceleration at quasi parallel shocks, J. Geophys, Res. 106, 21657-21673.

[80] Thomsen, M.F, (1985) Upstream suprathermal ions In: Tsurutani, B.T., Stone, R.G. (Eds), Collisionless Shocks in the Heliosphere : Reviews of current research, geophys Monograph Series, Vol 35. AGU, Washington D.C, pp 243-270.

[81] Thomsen, M. F., Gosling, J.T., Bame, S.J., Russell, C.T., (1990) Magnetic pulsations at the quasi-parallel shock, J. Geophys. Res. 95, 957-966.

[82] Treumann, R. A. and Scholer, M., (2001) The magnetosphere as a plasma laboratory. In: The century of Space Science. Kluwer Academic, p.1495.

[83] Tsubouchi and Lembege, (2004) Full particle simulations of short large amplitude magnetic structures (SLAMS) in quasi parallel shocks, J. Geophys. Res. 109, A02114.

[84] Weisstein, E. W., Spherical Point Picking from MathWorld, a Wolfram web resource.

[85] Wilkinson, W. P., Schwartz, S. J., (1990) Parametric dependence of the density of specularly reflected ions at quasi-perpendicular collisionless shocks. Planet. Space Sci. 38, 419- 435.

[86] Wilkinson, W. P., Pardaens, A. K., Schwartz, S. J., Burgess, D., Luhr, H., Kessel, R. L., Dunlop, M., Farrugia, C. J., (1993) Nonthermal ions and associated magnetic field behaviour at quasi-parallel Earth's bow shock. J. Geophys. Res. 98, 3889-3905.

[87] Wilkinson, W. P, (2003) The Earth's quasi-parallel bow shock: Review of observations and perspectives for Cluster. Planetary and Space Science 51, 629-647.

[88] Winske, D., Omidi, N., Quest., K. B., Thomas, V. A., (1990) Re-forming supercritical quasi parallel shocks 2. Mechanism for wave generation and front reformation, J. Geophys, Res. 95, 18,821-18,832.

[89] Winske, D., Omidi, N., (1996) A non-specialist's guide to kinetic simulations of space plasmas. J. Geophys. Res. 101, 17,287-17,303.

[90] Winske, D., Yin, L., Omidi, N., Karimabadi, H., Quest, K., (2003) Hybrid simulation codes: past, present and future - a tutorial.